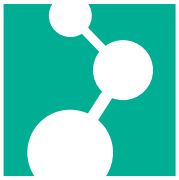

Application of a Hybrid Blocking Layer in Dye-Sensitized Solar Cells

Dissertation

zur Erlangung des Grades
„Doktor der Naturwissenschaften"
im Promotionsfach Chemie

am Fachbereich Chemie, Pharmazie und Geowissenschaften
der Johannes Gutenberg-Universität
in Mainz

Philipp Lellig
geboren in Trier
Mainz, Dezember 2011

Dissertation der Universität Mainz (D77)

Die vorliegende Arbeit wurde am Institut für Physikalische Chemie
der Johannes Gutenberg-Universität Mainz
und am Max-Planck-Institut für Polymerforschung in Mainz
in der Zeit von Dezember 2008 bis Dezember 2011 angefertigt.

"Quantum physics means anything can happen at any time for no reason."

Prof. Farnsworth

Abstract

In dye-sensitized solar cells a blocking layer between the transparent electrode and the mesoporous TiO_2 film is used to prevent short-circuits between the hole-conductor and the front electrode. The conventional approach is to use a compact layer of TiO_2 prepared by spin coating or spray pyrolysis. The thickness of the blocking layer is critical. On one hand, the layer has to be thick enough to cover the rough substrate completely. On the other hand, the serial resistance increases with increasing film thickness, because the layer acts as an ohmic resistance itself. In this thesis an amphiphilic diblock copolymer is used as a functional template to produce an alternative, hybrid blocking layer. The hybrid blocking layer is thinner than the conventional, compact TiO_2 film and thereby possesses a higher conductivity. Still, this type of blocking layer covers the rough electrode material completely and avoids current loss through charge recombination. The novel blocking layer is prepared using a tailored, amphiphilic block copolymer in combination with sol-gel chemistry. While the hydrophilic poly(ethylene oxide) part of the polymer coordinates a TiO_2 precursor to form a percolating network of titania particles, the hydrophobic poly(dimethylsiloxane) part turns into an insulating ceramic layer. With this technique, crack-free films with a thickness down to 24 nm are obtained. The presence of a conductive TiO_2 network for current flow, which is embedded in an insulating ceramic material, is validated by conductive scanning force microscopy. This is the first time that such a hybrid blocking layer is implemented in a solar cell. With this approach the efficiency could be increased up to 27 % compared to the conventional blocking layer. Thus, it is demonstrated that the hybrid blocking layer represents a competitive alternative to the classical approach.

Contents

1 Introduction **1**

2 Fundamentals **5**

2.1 Photovoltaics 5

2.1.1 Overview 5

2.1.2 Working Principle 8

2.1.3 Solar Cell Architecture 9

2.2 Blocking Layer in Solar Cells 10

2.3 Block Copolymers 14

2.4 Templating by Diblock Copolymers 17

2.5 ATRP 19

3 Methods **23**

3.1 NMR 23

3.2 GPC 23

3.3 SEM 24

3.4 TEM 25

3.5 SFM and Conductive SFM 25

3.6 XRR and XRD 27

3.7 SAXS and GISAXS 29

3.8 Characterization of Photovoltaics 30

4 Experimental **35**

4.1 Diblock Copolymer Synthesis 35

4.2 Blocking Layer Preparation 36

4.3 Solar Cell Assembly . . . 37
4.3.1 Liquid Electrolyte Based DSSCs . . . 37
4.3.2 Solid-State DSSCs . . . 38

5 Results and Discussion **39**
5.1 PEO-MA(PDMS) Block Copolymer . . . 39
5.1.1 Synthesis . . . 39
5.1.2 SAXS . . . 43
5.1.3 Scanning Force Microscopy . . . 45
5.2 The Conventional Blocking Layer . . . 46
5.2.1 Film Thickness . . . 46
5.2.2 Crystallinity . . . 47
5.2.3 Conductive SFM . . . 48
5.3 The Hybrid Blocking Layer . . . 50
5.4 Plasma Etching of the Hybrid BL . . . 52
5.4.1 Film Thickness . . . 53
5.4.2 Film Structure . . . 56
5.4.3 Crystallinity . . . 59
5.4.4 Conductive SFM . . . 61
5.4.5 Macroscopic Conductance . . . 63
5.4.6 Application in DSSCs . . . 65
5.5 Solvent Annealing of the Hybrid BL . . . 73
5.5.1 Film Thickness . . . 74
5.5.2 Film Structure . . . 76
5.5.3 Crystallinity . . . 78
5.5.4 Conductive SFM . . . 79
5.5.5 Macroscopic Conductance . . . 80
5.5.6 Application in DSSCs . . . 81

6 Summary and Outlook **87**

Bibliography **90**

1 Introduction

Today, energy generation is mainly based on fossil resources as well as on nuclear power. [1,2] Fossil resources are limited, and the burning of fossil fuels produces tons of carbon dioxide that promote the greenhouse effect and the climate change. Though the emission of nuclear power plants is lower, the generation of electricity comes along with the production and the problem of storing high-level radioactive waste. Furthermore, safety concerns arise through severe nuclear power plant accidents. [3] These issues demand for a transition to alternative, renewable, environmentally friendly, and safer sources of energy. These include wind power, solar energy, hydropower, bioenergy, and geothermal energy. [4–8] Solar energy stands out to be one of the best candidates to meet the increasing energy consumption. [9]
Photovoltaics convert sunlight directly into electricity. [10,11] The solar cell market is dominated by silicon based devices. [12] Organic and hybrid photovoltaics are low-cost alternatives to their expensive, inorganic counterparts. [13] Especially hybrid solar cells have gained increasing interest. Usually, hybrid solar cells consist of a mesoporous titanium dioxide film, which is sensitized by a dye, in combination with a liquid or solid-state hole-transport material. The so called *Grätzel cells* use a liquid electrolyte and excel by high power conversion efficiencies. [14] In their solid-state analogues, the electrolyte is replaced by a solid-state hole-transporting phase for everyday application. [15] However, the commercialization of these hybrid solar cells is hindered by their comparatively low power conversion efficiencies. To render these devices attractive for commercial application, each of the cell's components has to be optimized. Most effort is put in the optimization of the mesoporous TiO_2 film, the hole-transport material, as well as the sensitizer dye rather than on other layers of the solar cell. [16–18]

In hybrid solar cells a blocking layer between the hole-transport material and the front electrode is beneficial to improve the functionality of these devices and to obtain high power conversion efficiencies. [19–21] The blocking layer usually consists of a compact layer of titanium dioxide. This layer physically separates the transparent front electrode from the hole-conducting phase, thereby avoiding the recombination of charge carriers (Figure 1.1). As a result, the current output is increased signifi-

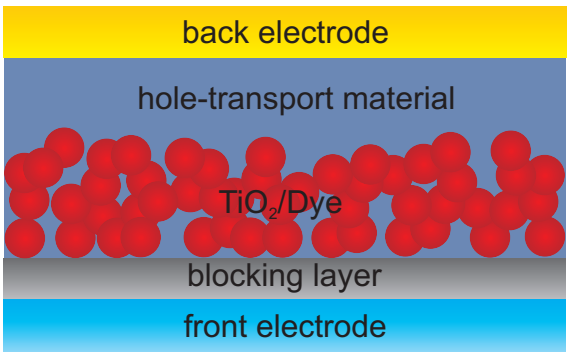

Figure 1.1: Structure of a hybrid solar cell with blocking layer.

cantly. However, this additional layer causes an increase in the serial resistance of the device and serves as a starting point for improvement.

A hybrid blocking layer that consists of a conducting TiO_2 network, which is embedded in a ceramic material, represents a competitive alternative to the classical, inorganic approach. For the preparation of the hybrid films an amphiphilic diblock copolymer is used to serve as templating agent in sol-gel chemistry. As these films can be prepared much thinner than the conventional blocking layer films, they should posses a higher conductivity accompanied by an increased efficiency in photovoltaics.

The aim of this thesis is to implement the novel, hybrid blocking layer in dye-sensitized solar cells as a replacement for the established, inorganic approach. At the same time, the correlation between the physical properties of the blocking layer and it's performance in solar cells is investigated. This is the first time that this type of blocking layer is incorporated in a solar cell device. Both, the conventional and the hybrid blocking layer, are characterized regarding their thickness, structure,

crystallinity/crystal structure, microscopic/macroscopic conductivity, and their application in solar cells. In doing so, the hybrid blocking layer is put into direct comparison to the conventional one under identical conditions.

2 Fundamentals

2.1 Photovoltaics

2.1.1 Overview

Commercially available photovoltaic devices are mainly based on inorganic materials especially on silicon. [22] Currently, power conversion efficiencies as high as ~ 25 % are reached with these silicon based devices. [23,24] Monocrystalline and polycrystalline silicon is the most widely used material for these solar cells. Using the polycrystalline semiconductor reduces the production costs but lowers the power conversion efficiency of the photovoltaic modules. Thin film technology is an alternative way to produce cheaper devices. In these types of solar cells thin films of amorphous silicon, cadmium telluride (CdTe), or copper indium gallium selenide (CIGS) are used. Thin film solar cells generally exhibit lower efficiencies than the thick, crystalline, silicon based devices but are more cost-effective. For example, using a solar cell based on amorphous silicon in a pocket calculator is sufficient as only little power is required. Organic and hybrid solar cells have gained increasing interest in science as well as in industry. [25,26] Though the efficiency and the stability of the inorganic devices are not reached, several advantages render these types of solar cells attractive for the large scale application. Instead of expensive inorganic materials, cheaper organic materials can be used in the production of these devices. These materials exhibit very high optical absorption coefficients and allow for the production of very thin devices. As most of the materials are processed from solution and at low temperatures, the devices can be fabricated using a convenient, inexpensive roll-to-roll printing technique. Therefore, the energetic payback time for these types of solar

cells is expected to be low. Organic devices are suited especially for applications where low weight or mechanical flexibility is of importance. By molecular engineering the properties of the organic molecules can be adjusted to optimize their application in photovoltaics.

Organic solar cells use conjugated, semiconducting polymers and small organic molecules. [27,28] In polymer-polymer (plastic) solar cells an electron-conducting and a hole-conducting polymer are blended in the photoactive layer. Among the organic solar cells high efficiencies are achieved by the combination of a hole-conducting polymer with a fullerene derivate. [29] 6,6-Phenyl-C_{61}-butyric acid methyl ester (PCBM) is a soluble derivative of the C_{60} buckminsterfullerene. This efficient electron acceptor type material is combined with a variety of different hole-conducting polymers. Good results are obtained in combination with poly(3-hexylthiophene) (P3HT). However, the use of fullerenes has some disadvantages, such as molecular diffusion at elevated temperatures. [30] Therefore, inorganic materials are used to replace the electron-conducting material.

In hybrid solar cells the acceptor-type material is replaced by inorganic semiconductors like TiO_2, CdS, CdSe, PbS, PbSe, ZnO, or SnO_2. [31–37] However, in most cases titanium dioxide is the choice of material. [38] Titanium dioxide is a cheap, non-toxic semiconductor that is used as a white pigment in wall paint, tooth paste, or sunscreen. Its most relevant modifications are anatase and rutile. Even though rutile is the most common form and exhibits better light-scattering properties, the anatase modification is preferred for the use in photovoltaic applications due to better dye absorption and faster electron transport. [39] For the application in solar cells a mesoporous anatase layer is used to increase the surface area and allow for efficient light harvesting. The inorganic material offers good electrical conductivity, processability, as well as physical and chemical stability. Poly(thiophene) and poly(phenylene vinylene) (PPV) based polymers exhibit good hole-conducting properties and are frequently used in combination with titanium dioxide. [40–44] This way, the unique properties of inorganic and organic materials are combined in these types of devices. In dye-sensitized solar cells (DSSCs) the inorganic layer is sensitized by a dye to increase the light absorption. Metal-free, organic dyes have been used, however,

the best results were obtained using amphiphilic, ruthenium based sensitizers. [45–50] The structure of the standard ruthenium dye cis-Bis(isothiocyanato)(2,2'-bipyridyl-4,4'-dicarboxylato)(4,4'-di-nonyl-2'-bipyridyl)ruthenium(II) (Z907) is shown in Figure 2.1. The carboxylate groups serve as anchors to bind to the TiO_2 surface. [51,52]

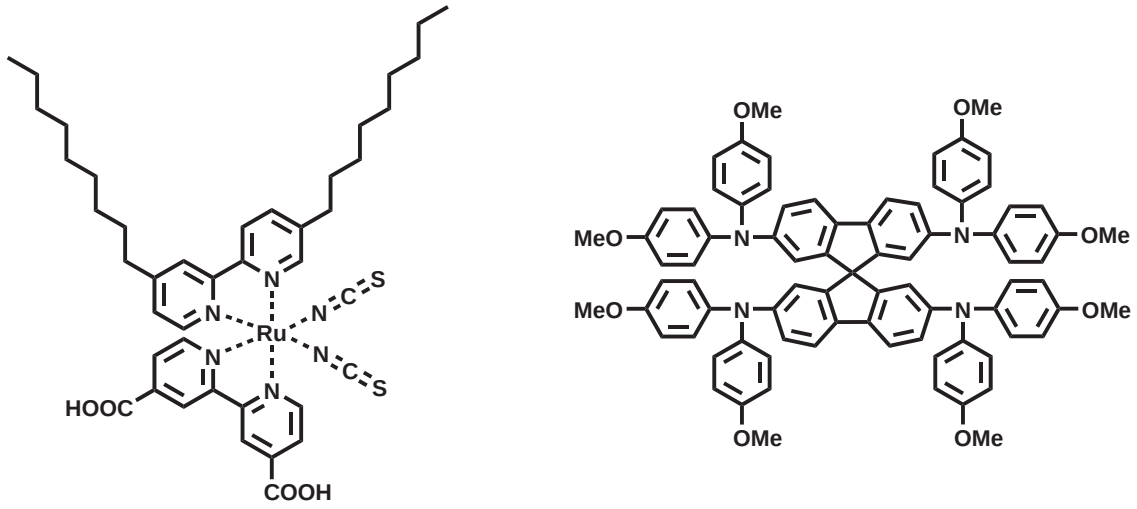

Figure 2.1: Sensitizer dye Z907 (left) and hole-conducting material spiro-OMeTAD (right).

In Grätzel cells a dye-sensitized TiO_2 film is used in combination with a liquid electrolyte containing a iodide/triiodide redox couple dissolved in an organic liquid. With this architecture efficiencies beyond 10 % have been reached. [53] Ionic liquids represent an alternative for the electrolyte to avoid evaporation and increase the lifetime of the devices. [54] However, considering the application in everyday life, one wants to avoid the use of liquids. To do so, the liquid electrolyte is replaced by solid-state hole-transport materials. [55,56] The widely used hole-transport material 2,2',7,7'-tetrakis-(N,N-p-dimethoxyphenylamine)-9,9'-spiro-bifluorene (spiro-OMeTAD) is shown in Figure 2.1. [57,58] The spiro-center avoids crystallization and improves the infiltration of the TiO_2 network as well as the contact between the titania and the hole-transport material. [59] For these types of hybrid solar cells efficiences up to 4 % are reported. [51]

2.1.2 Working Principle

Photovoltaics are based on and named after the photovoltaic effect. This effect describes the generation of a voltage along with an electrical current upon the absorption of light. The basic working principle of a solar cell, consisting of a donor and an acceptor type material sandwiched in between two electrodes of different workfunction, is depicted in Figure 2.2. In organic solar cells illumination takes

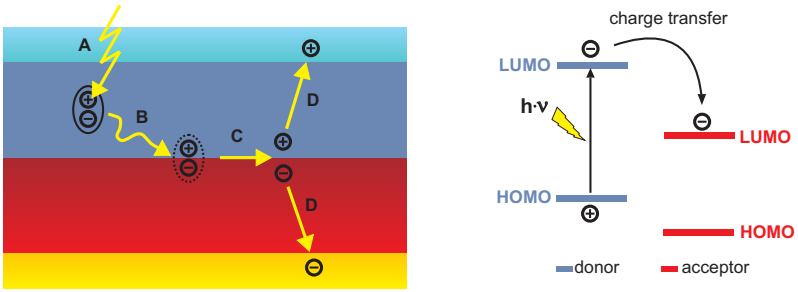

Figure 2.2: Working principle of a solar cell (left) with corresponding energy diagram (right).

place through a transparent electrode acting as a window material. Upon light absorption an electron in the donor type material is excited from the highest occupied molecular orbital (HOMO) to the lowest unoccupied molecular orbital (LUMO), leading to the creation of an exciton (Figure 2.2, A). An exciton is a neutral, excited state of a molecule, i.e. an electron-hole pair that is bound by electrostatic interaction. This is in contrast to inorganic devices where free electrons and holes are generated directly. The exciton can diffuse in a limited range of around 4-20 nm (Figure 2.2, B). [60,61] The diffusion length depends on the type of the organic material, e.g. P3HT exhibits an exciton diffusion length of 4 nm, whereas a value of 12 nm is reported for PPV. [62,63] Excitons may recombine by emitting a photon or decay nonradiatively by the generation of thermal energy. However, if the exciton reaches a donor/acceptor interface, the electron is injected into the LUMO of the acceptor (Figure 2.2, C). This way, holes and electrons are separated, and free charge carriers are generated. Thus, electrons and holes are transported separately through different materials. Driven by the internal electric field and due to the gradient in charge carrier concentration, electrons and holes are transported towards

the front and back electrode, respectively (Figure 2.2, D). After having reached the electrodes, the charge carriers can be extracted from an external consumer.

2.1.3 Solar Cell Architecture

In (inorganic-) organic solar cells the donor and acceptor type materials can be combined in different ways. [64–66] Examples of device architectures are shown in Figure 2.3. In bilayer heterojunction devices both materials are applied successively

Figure 2.3: Examples of device architectures: bilayer heterojunction (left), bulk heterojunction (middle), and ordered, bulk heterojunction (right).

on the substrate. This simple approach is advantageous in the sense that the charge carriers can travel independently towards the electrodes within separate materials and without the requirement of charge percolation pathways. Thus, the recombination of charge carriers after their generation is low. The drawback of this design is that only the excitons generated in the vicinity of the interface between donor and acceptor lead to charge carrier generation as a result of the limited exciton diffusion length. This turned out to be the main limitation of the photocurrent generation in these bilayer devices. This problem was overcome by the concept of bulk heterojunction devices.

The processing of the donor and acceptor type material often allows to already blend these materials in solution. For example, titanium dioxide can be synthesized *in situ* in a polymer solution to yield an inorganic network within an organic matrix. Vice versa, the synthesis of a polymer can be conducted within an inorganic framework. This way, an interpenetrating network of donor and acceptor is achieved. At the same time, the coating of the substrate with both materials is reduced to a single step. The bulk heterojunction design enlarges the surface of the donor/acceptor

junction compared to the bilayer architecture. Excitons are always generated in the vicinity of the heterojunction, and charge carriers are generated all over the active layer. This allows for thicker active layers. However, the morphology of the resulting blend is critical. The charge carriers can undergo recombination on their way towards the electrodes or may get trapped in imperfect percolation pathways.
The ordered, bulk heterojunction concept represents an ideal structure of the bulk heterojunction devices. These devices can be prepared, for example, by using the self assembly of polymers. Another technique is to synthesize inorganic, vertically aligned nanotubes that can be mixed or backfilled with an organic material. [67–70] This design offers the most direct pathway for the charge carriers to reach the electrodes without the occurrence of imperfect percolation pathways. The heterojunction surface and the charge generation is maximized, and at the same time the charge transport is optimized. However, the fabrication of these structures is challenging.

2.2 Blocking Layer in Solar Cells

Figure 2.4 shows a section of a titanium dioxide based DSSC without (A) and with (B) blocking layer. The charge separation of the exciton takes place at the pn-junction of the mesoporous titanium dioxide and the hole-transport layer. The rectifying, diode-like contact at this interface guarantees unidirectional charge carrier transport and is of utmost importance for the functionality of the solar cell. After the separation of the charge carriers, the electrons are transported towards the

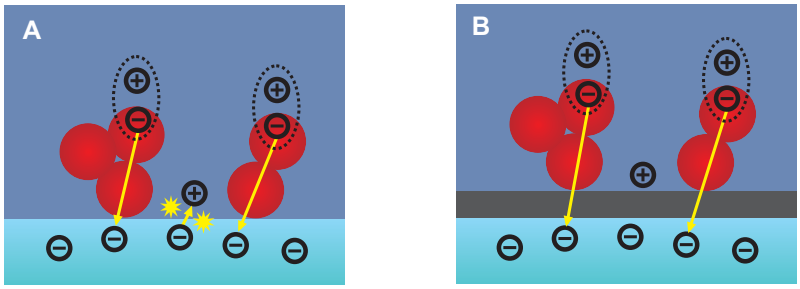

Figure 2.4: Section of a TiO_2 based solar cell without (A) and with blocking layer (B).

transparent conductive oxide (TCO) electrode driven by the internal electrical field. Due to the high porosity of the mesoporous titanium dioxide, the hole-conducting material is also in contact with the TCO electrode (Figure 2.4, A). Unfortunately, this allows recombination between the electrons gathered at the electrode and the holes in the hole-transporting material if an ohmic contact is formed. An ohmic contact is present, for example, when spiro-OMeTAD is used as a hole-conductor (see page 69, Figure 5.22). [71]

To overcome this problem a compact layer of titanium dioxide - the blocking layer - is used to avoid these short-circuits. [72–75] The purpose of the blocking layer (BL) is to physically separate the hole-transport material from the TCO electrode (Figure 2.4, B). The pn-junction between the hole-transport layer and the TiO_2 of the blocking layer blocks the electron migration towards the hole-conducting phase, and the charge recombination is avoided. As a consequence the photocurrent output is increased significantly. By the implementation of a blocking layer the efficiency of solid-state DSSCs could be increased by three to four orders of magnitude. [76] Moreover, it has been found that in some cases devices do not work at all in the absence of a blocking layer. [77] Additionally, the deposition of a thin titanium dioxide layer on top of the TCO material improves the mechanical adhesion of the mesoporous titania film. [78, 79]

Alternatives that use other materials than TiO_2 have been presented. [80–85] However, these alternatives involve complicated fabrication processes, thus, titania is still the most widely used material. For the preparation of blocking layer films two major techniques are established. [86, 87] Liquid coating techniques like spin or dip coating as well as chemical vapor deposition methods like spray pyrolysis are suited to produce compact TiO_2 films. Good results were obtained using the spray pyrolysis technique. However, the preparation by spin or dip coating of a sol-gel mixture containing a TiO_2 precursor is more convenient and produces films of the same functionality. [88, 89] This is why the solution-processed coating techniques are often favored.

Tin-doped indium oxide (ITO) or fluorine-doped tin oxide (FTO) coated glass is typically used as TCO material. [90, 91] Both materials exhibit high transparency as

well as a high conductivity. Several studies focus on the influence of the type of TCO material on the performance of DSSCs. [92,93] The results are ambiguous and it seems that the right choice of electrode material is dependent on the cell type and the cell design. However, ITO is known to lose its conductivity upon exposure to elevated temperatures. [94–96] Also, ITO glass is more expensive than FTO glass. For these reasons FTO coated glass substrates are often favored, and FTO was chosen to serve as TCO material in this thesis as well. A scanning force microscopy image of this FTO-coated glass is shown in Figure 2.5. The height scale of 227 nm and the

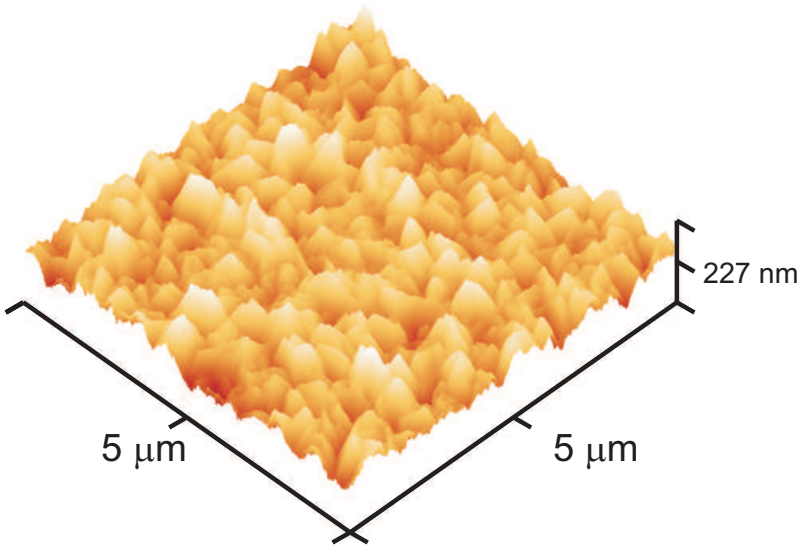

Figure 2.5: Scanning force microscopy image of FTO-coated glass.

root mean square (RMS) roughness of 41.7 nm make it clear that it is challenging to coat the FTO substrate by a thin, closed film. For an effective blocking layer it is particularly important to cover the rough TCO substrate completely by a closed film. The occurrence of cracks and holes in the film would result in charge recombination.

Usually, the blocking layer is prepared using an organic TiO_2 precursor. During the drying and sintering process the film contracts. If the titanium dioxide layer is too thin, cracks or holes form in the film. Cracking of inorganic materials upon drying, sintering as well as during cooling is a well-known problem in the production of thin films. [97–99] Thus, to obtain a closed film a certain minimum film thickness is re-

quired. However, the thickness of the blocking layer is a critical factor, because the serial resistance of the layer increases with increasing film thickness due to the formation of voids and impurities. A film that is too thick will hinder the current flow. In a detailed study by Peng et al. TiO_2 blocking layers of different thickness were used in solid-state DSSCs of identical structure. [76] This way, the device efficiencies could be correlated to the thickness of the blocking layer. The highest efficiency was obtained with a blocking layer thickness of 150 nm. Furthermore, an optimum range was determined to lie between 120 and 200 nm. Below a thickness of 120 nm the charge recombination was only partially suppressed, leading to a worsening of the performance of the solar cells. Thus, the inorganic blocking layer is restricted to a certain minimum thickness, which is associated with a certain serial resistance. An alternative, hybrid blocking layer developed recently in our group constitutes a promising replacement for the compact TiO_2 blocking layer. [100] Using a hybrid material instead of a pure inorganic film offers the possibility to reduce the thickness of the blocking layer without the formation of cracks or holes in a convenient way. These hybrid films contain a percolating TiO_2 network, which is templated by an amphiphilic copolymer. In the first place a triblock copolymer was used to template these hybrid films. In this work the preparation route has been enhanced by using a new kind of amphiphilic diblock copolymer. The use of a diblock instead of a triblock copolymer offers better control over the morphologies obtained in the hybrid layer that are designated by the phase diagrams.

The diblock copolymer contains a hydrophilic poly(ethylene oxide) (PEO) part and a hydrophobic poly(dimethylsiloxane) (PDMS) part. This templating agent is combined with a TiO_2 precursor in sol-gel chemistry. The function of the hydrophilic PEO part is to coordinate with the titania precursor to template the TiO_2 network. The PDMS part ceramizes during a calcination step and turns into an organic glass, i.e. a carbon-containing silicate glass (Si-O-C). [101] In the calcination process the polymer acts as a cross linking agent and avoids crack formation whereby films of reduced thickness can be prepared. Voids or cracks that may form during the sintering process are filled up by the polymer. Thus, the diblock copolymer not only acts as a templating agent like an ordinary surfactant but also carries a further functionality

to build the resulting hybrid material. It has been shown that the successive coating of titania particles with a layer of PDMS does not avoid the crack formation upon sintering. [102] The desired effect is only observed when the titania is templated by such a tailored, PDMS containing copolymer. This way, a conductive TiO_2 network with defined charge percolation pathways for current flow, which is embedded in an insulating ceramic material, is created. Since these novel blocking layers can be prepared much thinner than the conventional, compact TiO_2 films, they should posses a lower serial resistance and a higher conductivity. Still, this type of blocking layer covers the TCO substrate completely avoiding current loss through charge recombination. As a result, an improved current output and improved efficiency of solar cells is expected. This makes a hybrid composite an attractive material for the preparation of blocking layer films.

2.3 Block Copolymers

If more than one type of monomer is used in a polymerization, a copolymer is obtained. Multiple monomers can be used in a copolymerization, however, in most cases two types of monomers are used to build a diblock copolymer. The types of monomers and their composition allow to adjust the physical and chemical properties of the polymer. For example the implementation of poly(butadiene) into poly(styrene) leads to a poly(styrene) derivative that is more robust and less brittle than its homopolymer. Several types of binary copolymers are depicted in Figure 2.6. In linear copolymers the different types of polymerchains (blocks) can be connected alternating, statistically, periodically or as a gradient. Statistical and alternating di-

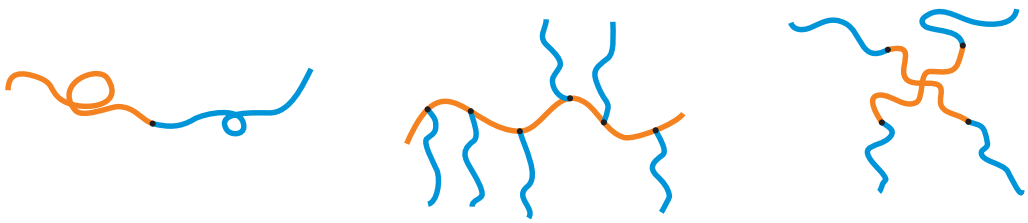

Figure 2.6: Linear (left), graft (middle), and star (right) block copolymers.

block copolymers are usually obtained by radical polymerization techniques. Linear block copolymers are synthesized by ionic polymerization techniques or controlled living radical polymerization. Graft copolymers are accessible by *grafting to* or *grafting from* polymerization. In these techniques the sidechains are added to an existing polymerchain that carries anchor groups (grafting to), or the sidechains are polymerized successively from functional groups within the backbone (grafting from). Star block copolymers are produced by employing multifunctional initiators or by using multifunctional coupling agents.

If two thermodynamically incompatible polymerchains are covalently bound in a block copolymer, they cannot separate macroscopically and tend to phase separate on the nanoscale instead. This self-assembly results in 3-dimensional, ordered structures without external direction. Several morphologies can be obtained depending on the relative block length (Figure 2.7). [103] For symmetric compositions a lammellar

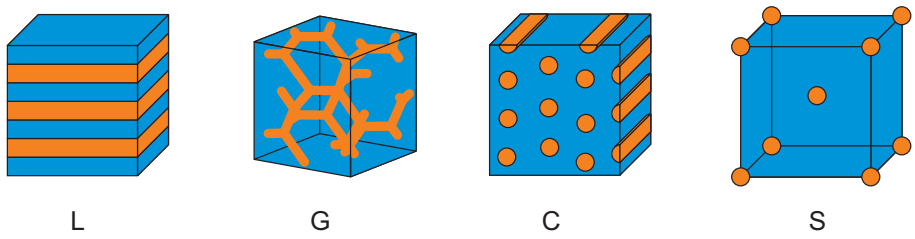

Figure 2.7: Morphologies of diblock copolymers: Lammellar (L), gyroid (G), hexagonal packed cylinder (C), and cubic packed spheres (S) (inverse phases are not shown).

phase is often found (Figure 2.7, L). Small variations in the symmetric composition lead to perforated lammellar morphologies or catenoid phases. A slight decrease of one block leads to the formation of the gyroid phase, and the minority component forms a percolating 3-dimensional network surrounded by the majority phase (Figure 2.7, G). If the asymmetry of the blocks is further increased, the smaller blocks arrange as cylinders in a hexagonal packed arrangement (Figure 2.7, C). Finally, at very dissimilar compositions, the formation of sphere-like domains of the small block, dispersed in a matrix of the larger block, is found (Figure 2.7, S). The inverse structures of the depicted morphologies are formed if the block length ratio is

changed the other way around.

Apart from the molecular weight ratio, there are further parameters that play an important role in the phase separation of diblock copolymers. The phase separation is governed by a balance between enthalpic and entropic factors. A thermodynamic description of the driving force for the microphase separation is given by the Flory-Huggins interaction parameter χ_{AB}: [104]

$$\chi_{AB} = \frac{z}{k_B T}\left(\epsilon_{AB} - \frac{1}{2}\left(\epsilon_{AA} + \epsilon_{BB}\right)\right) \tag{2.1}$$

In equation 2.1 z is the number of nearest neighbors per monomer, $k_B T$ is the thermal energy, and ϵ_{AB}, ϵ_{AA} as well as ϵ_{BB} are the interaction energies between the different types of monomer units, respectively. If there is a repulsive force between dissimilar polymer chains, ϵ_{AB} is positive, whereas a negative value indicates that both blocks are miscible. The Flory-Huggins interaction parameter determines the driving force for the phase separation. A negative value for χ_{AB} indicates a favorable interaction, and a positive value indicates an unfavorable interaction between species A and B. As the temperature stands in the denominator in this formula, the mixing is promoted at elevated temperatures. The Flory-Huggins interaction parameter, multiplied by the degree of polymerization N, represents the interaction per block. If $N\chi_{AB}$ is small, entropic factors dominate and mixing is favored. At high values of $N\chi_{AB}$ energetic effects dominate, leading to a demixing and a phase separation. At some point in between, an equilibrium state between enthalpic and energetic factors is found. This point is called the *order-disorder transition* (ODT). [105]

The interaction parameter can be used to predict whether a phase separation will occur or not. This allows to map a theoretical phase diagram for diblock copolymers (Figure 2.8). [106] The phase diagram maps the morphology in dependence of the interaction parameter $N\chi$ and the volume fraction f_A of one block with respect to the other. For symmetric diblock copolymers ($f_A = 0.5$) both blocks will mix, and no phase separation is observed if $N\chi_{AB} < 10.5$. If $N\chi_{AB} > 10.5$ diblock copolymers are expected to undergo phase separation, and a lamellar phase is predicted.

However, the morphology of thin copolymer films may differ from the structure

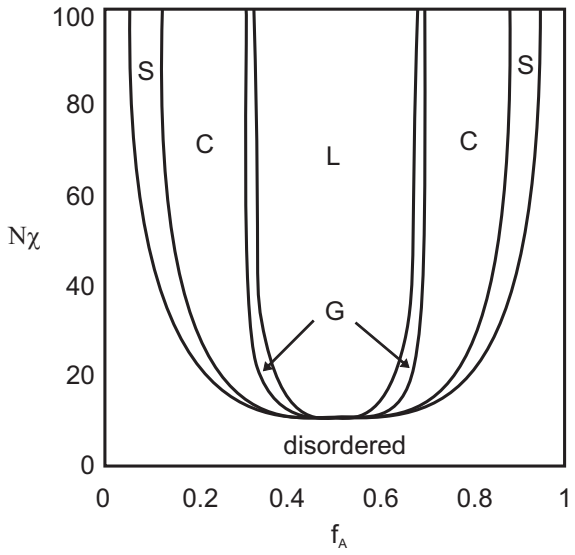

Figure 2.8: Theoretical phase diagram of a diblock copolymer (adapted [103]).

in bulk. [107,108] If a substrate is coated with a polymer film, the interaction of the substrate and the free surface with the polymer has to be taken into account, respectively. Especially in very thin films the surface/interfacial energetics play a major role. The substrate may exhibit a preferential attraction to one block of the polymer. This case leads to microdomains that are oriented parallel to the substrate. If the surface of the substrate is neutral, i.e. it allows the presence of both blocks, the domains can orient normal to the substrate surface. Therefore, the nanostructure of thin polymer films can be influenced by substrate surface modifications or by post treatments of the films, e.g. thermal or solvent vapor annealing.

2.4 Templating by Diblock Copolymers

The morphologies of copolymers that exhibit defined structures on the nanoscale offer the possibility to employ copolymers as templating agents for the production of organic, inorganic, and hybrid materials. [109–112] Through their self-assembly the periodic structures of polymers can be transferred to large area surfaces. The morphology of a copolymer can be adjusted according to its phase diagram, and the size of the resulting structures is determined by the molecular weight. This technique is used, for example, in diblock copolymer lithography. [113] When a diblock copolymer

is spin coated onto a substrate, an etching or irradiation process can be used to selectively remove one block. This way, the polymer can be used as a mask for further functionalization of a substrate, e.g. evaporation of metals to create an electrical circuit. Afterwards, organic residuals can be removed by a calcination step. Diblock copolymer lithography can create much smaller structures than photolithographic techniques or electron beam lithography in a very convenient way.

Furthermore, the structure directing function of copolymers can be combined with sol-gel chemistry to yield inorganic materials of defined shape and size. In sol-gel chemistry typically a metal alkoxide precursor is used to produce oxide type materials. [114,115] Through the hydrolysis of the precursor a colloidal dispersion of particles in a liquid (sol) is formed. The continuation of this process can lead to crosslinking and to the formation of a 3-dimensional inorganic network (gel).

When an amphiphilic copolymer is combined with sol-gel chemistry, the inorganic sol particles are templated by the hydrophilic block of the diblock copolymer. [116] For this purpose, PEO is often used as the hydrophilic block. After the selective removal of the polymer, the inorganic, templated structure remains. By this technique the morphology is not only determined by the properties of the diblock copolymer alone, and a variation of the sol-gel composition can lead to a variety of different structures. [117]

If transition metal oxide precursors are employed, the obtained materials are appealing for the application in photovoltaics. [118–123] Especially, the fact that the size of the block copolymer phase separation matches the size of the exciton diffusion length renders copolymer templated materials attractive for the application in solar cells. [124] Titanium dioxide is a widely used n-type semiconductor in solar cells, which can be prepared by sol-gel chemistry using titanium containing precursors. The structure of the TiO_2, playing a decisive role in the functionality of the devices, can be fine-tuned by the sol-gel process and the choice of templating polymer. Several studies report on the preparation of mesoporous titania films for the application in solar cells produced by the sol-gel technique. [125,126]

Often the polymer is combusted after having acted as templating agent. However, if the diblock copolymer carries a further functionality, this step is not applicable

and a hybrid material is created. For example, a tailored diblock copolymer was synthesized by linking the hole-conducting polymer poly(triphenylamine) covalently to a PEO block to template titanium dioxide. [127,128] This circumvents an additional filling step of the titanium dioxide structure with the hole-conductor afterwards.
Thus, tailored copolymers represent a class of templates superior to ordinary surfactants. In this thesis a tailored diblock copolymer is used as a functional template as well. The templating copolymer is synthesized by atom transfer radical polymerization (ATRP).

2.5 ATRP

Free radical polymerization is one of the most important polymerization techniques for the production of high molecular weight polymers. [129,130] A variety of different monomers is suited for this type of polymerization and copolymerization under convenient experimental conditions. The procedure requires the absence of oxygen but is tolerant to water and small impurities. Typically, the free radical polymerization is conducted in a temperature range between room temperature and 100 °C under ambient pressure. The polymerization can be carried out in bulk, in solution, or in aqueous media. In contrast to the step-growth polymerization, high molecular weight products are obtained already after short reaction times and at low conversions. As all kinds of alkenes functionalized with hydroxy-, amino- and acid-groups can be used, nearly 50 % of all commercial polymers are produced by the free radical polymerization. The most important examples for commercially synthesized polymers via radical polymerization are ethylene, styrene, vinyl chloride and (meth)acrylates.
However, the control over the molecular weight and the polydispersity of the products is difficult as a result of chain transfer and termination reactions between radicals. While the chain transfer reactions can be suppressed by the proper choice of reaction conditions, the diffusion driven termination of the free radicals, namely recombination and disproportionation, can hardly be avoided. To minimize the termination reactions and to obtain high molecular weights, the concentration of

radicals is minimized to some ppm. Still, the rate of initiation is much lower than the rate of propagation, thus, the number of growing chains is very small during the polymerization ($\sim$ 0.1 %). This leads to a broad distribution of the chain lengths, and the preparation of polymers with controlled architecture is not possible using the free radical polymerization.

Controlled living radical polymerization techniques allow for the synthesis of high molecular weight polymers of well defined architecture in the absence of chain transfer or termination reactions. These include the *reversible addition fragmentation chain transfer* (RAFT), the *nitroxide mediated polymerization* (NMP), and the *atom transfer radical polymerization* (ATRP). [131, 132] RAFT relies on a degenerative chain transfer process. Propagating polymerchains of different length are exchanged, leading to a narrow molecular weight distribution in the product. In NMP and ATRP a controlled radical polymerization is achieved by a dynamic equilibrium between an active and a dormant species.

The fundamental steps involved in ATRP are shown in Figure 2.9. The basic mech-

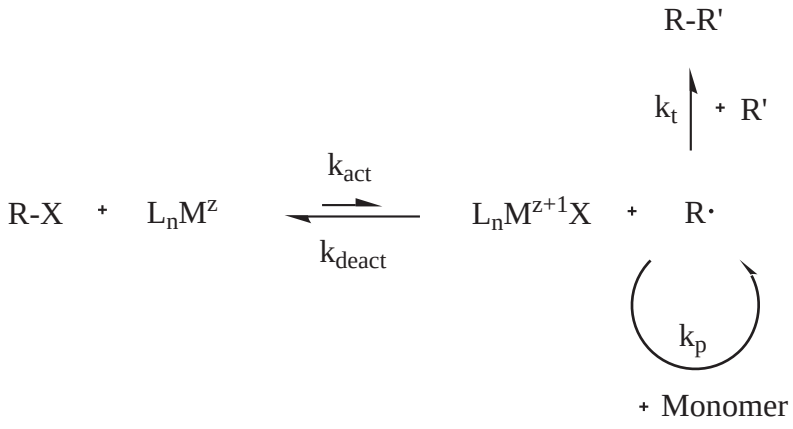

Figure 2.9: Mechanism of atom transfer radical polymerization.

anism of ATRP is the reversible, homolytic cleavage of an alkyl halide R-X by a transition metal complex L_nM^z. The transition metal is oxidized, and an alkyl radical is generated. Similar to the free radical polymerization, the generated radical can add monomer or undergo radical-radical termination. However, in ATRP the rate constant of deactivation k_{deact} is much higher than the rate constant of acti-

vation k_{act}, favoring the dormant species rather than the active radical. Thus, by trapping the radical in the dormant form, which cannot undergo recombination, the radical concentration is reduced. This way, the rate constant of termination k_t is significantly reduced compared to the rate constant of propagation k_p, and termination reactions are almost completely avoided. After a certain time in the dormant state, the polymer chain is reactivated and more monomer can be added. The active species reacts with only a few monomer units before it is converted back into the dormant form. Thus, each polymerchain is active for only a few milliseconds and stays in the dormant state for several seconds. Typically, in a polymerization this cycle is repeated ~ 1000 times, and a total lifetime of several hours is achieved. This way, the lifetime of a polymerchain is significantly increased compared to the free radical polymerization where a growing polymer chain adds monomer every ~ 1 ms and has a lifetime of only ~ 1 s. Additionally, in ATRP the initiation is much faster than in the free radical polymerization, and all chains are essentially initiated at the same time. Thus, all chains grow to the same length, and low polydispersities ($1.0 < M_W/M_N < 1.5$) are obtained in the product. The degree of polymerization X can be adjusted by the initial monomer to initiator ratio:

$$X = \frac{[M]_0}{[I]_0} \tag{2.2}$$

After the polymerization the chains remain active allowing their end-functionalization and the synthesis of copolymers by sequential monomer addition.

ATRP can be conducted in a wide temperature range from sub-zero to > 100 °C. The list of monomers suitable for ATRP includes styrenes, (meth)acrylates, (meth)-acrylamides, vinylpyridine, acrylonitrile, and others. Transition metals like Fe, Co, Ni are used to mediate the reaction. However, the best results are obtained with copper catalysts that allow to process various monomers in a number of different solvents. Polydentate, N-containing ligands like alkylamines and pyridines are used to mediate ATRP. [133,134] The ligands allow for the solubility of the copper complex in organic solvents and adjust the atom transfer equilibrium. Often the chemical structure of the initiator is similar to the one of the monomer.

3 Methods

3.1 NMR

Nuclear magnetic resonance (NMR) spectroscopy allows to investigate the chemical structure and configuration of macromolecules. [135] Only nuclei with an odd number of neutrons and/or protons are accessible to NMR spectroscopy (e.g. ^{1}H, ^{13}C). The technique is based on the Zeeman effect that describes the orientation of nuclei parallel or anti-parallel to an external magnetic field. The orientation of the nuclei can be switched by the absorption of electromagnetic radiation. This phenomenon happens at a specific resonance frequency that is dependent on the chemical environment of the nuclei. A frequency sweep yields distinct resonance frequency for each nucleus, and these frequencies can be transformed into a NMR spectrum. In a NMR spectrum the signals are given as the chemical shift relative to a reference compound (tetramethylsilane).

^{1}H-NMR Setup

Manufacturer:	Bruker
Device:	Avance DPX 250
Frequency:	250 MHz

3.2 GPC

Gel permeation chromatography (GPC) is an important method for the determination of the molecular weight and the molecular weight distribution of polymers. [136] Polymer molecules are separated based on their hydrodynamic radius. The polymer sample is dissolved in a suitable solvent and washed down a chromatography

column packed with a porous material. The molecules enter the pores driven by a concentration gradient. This way, the molecules are trapped for some time, and their retention time is increased. The smaller the molecules, the more pores they can enter, and the longer they are retained. Thus, molecules of different size are separated from each other, headed by the high molecular weight fraction. As GPC is a relative method, a calibration is required. For this purpose, monodisperse polymers are used. The best results are obtained if the polymer used for calibration has a similar structure to the one examined. The concentration of the polymer in the eluent is monitored by refractive index, ultra-violet or light-scattering detectors. With the help of the calibration curve, the number average, the weight average, as well as the polydispersity of the sample can be calculated.

GPC Setup

Columns:	3 Polymer standard service columns (SDV)
Pump:	Waters 515 HPLC Pump
Detector:	RI ERMA Inc. ERC 7512 ERC
Eluent:	THF - Flowrate 1 ml/min

3.3 SEM

In scanning electron microscopy (SEM), an electron beam is used to map the surface of a specimen. [137,138] An electron beam with an energy of some keV is emitted by a cathode (gun) and focused by condenser lenses. The beam is used to scan a rectangular area of the specimen line-by-line. The electrons interact with the atoms at or near the sample surface depending on the acceleration voltage. Back-scattered or secondary electrons are detected by specialized detectors. This signal is amplified and yields a magnified black and white image of the sample surface with resolutions in the nm range (and below). Different grey scale values in the SEM image arise from differences in the electron densities of the materials. Elements of higher atomic number appear brighter than those of lower atomic number.

SEM Setup

Manufacturer:	Zeiss
Device:	LEO 1530 Gemini
Acceleration voltage:	1-2 kV

3.4 TEM

The working principle of transmission electron microscopy (TEM) is similar to the one of light microscopy. [139] However, in this microscope electrons are used instead of visible light. Electrons are emitted from a cathode and accelerated towards the sample to transmit the very thin specimen. Instead of optical lenses (made of glass), electromagnetic lenses are used for this purpose. The electrons interact with the sample, and the transmitted electrons are detected by a CCD detector. As the resolution is correlated to the wavelength of the electromagnetic radiation, TEM offers much higher resolution than light microscopy, and small structures down to the atomic scale can be visualized. Furthermore, TEM allows to determine the elemental distribution within a sample with the help of electron spectroscopic imaging (ESI). [140]

TEM Setup

Manufacturer:	FEI
Device:	Tecnai F20
Acceleration voltage:	200 kV

3.5 SFM and Conductive SFM

Instead of using visible light or electromagnetic radiation, in scanning force microscopy (SFM) a sharp tip is used to probe a sample surface. [141] The tip, mounted to the end of a flexible cantilever, is used to scan the sample in a raster pattern. Depending on the operation mode, the tip is not, in intermittent or in permanent contact with the surface. While contact-mode SFM is suited for scanning hard surfaces, soft-matter like polymers is often investigated by the dynamic operation

modes. The topography of the sample as well as interactions between the tip and the sample surface lead to a bending of the cantilever. The deflection of a laser beam that is reflected from the top side of the cantilever is detected on a photodiode. This allows to map the surface properties of the sample providing atomic resolution. Besides the topography, SFM can yield further information such as mechanical, electrical, and magnetical material properties. If a voltage is applied between the tip and the sample, local electrical currents can be measured in conductive SFM (Figure 3.1). [142] In this case a conductive tip is used for the measurement, and a DC voltage

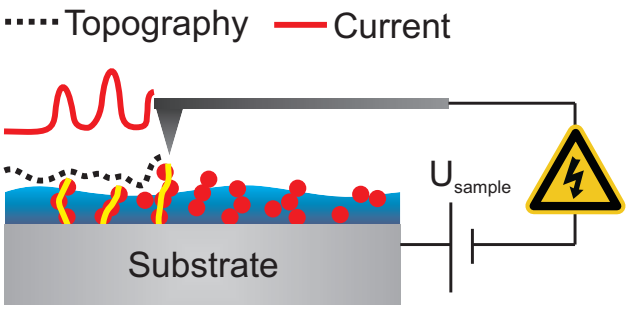

Figure 3.1: Principle of conductive scanning force microscopy.

is applied between the tip and the sample establishing an electrical circuit. For this purpose, a metal coated silicon cantilever is used to increase the conductivity. A mapping of the conductivity on the microscopic scale is obtained that can be directly related to the topography. Conductive scanning force microscopy is especially interesting for the investigation of composite materials.

SFM Setup

Manufacturer:	Veeco
Device:	Multimode
Cantilever (tapping mode):	OMCLAC 160 TS-W2 Silicon
Cantilever (cond. SFM):	CSC17 Ti/Pt

3.6 XRR and XRD

In X-ray reflectivity (XRR) a beam of X-rays is reflected from a thin film or multilayer systems to obtain information on the layer thickness, roughness, and density. [143,144] The sample is illuminated by a monochromatic X-ray beam with a wavelength λ in the order of 0.1 nm under variation of the incident angle α_i. If the incident angle is below the critical angle of the sample α_c, the beam is totally reflected (total external reflection). Above the critical angle the beam is partially reflected from the surface and partially transmitted through the material (Figure 3.2). The reflected beam is confined in a direction symmetric to the incident angle. The

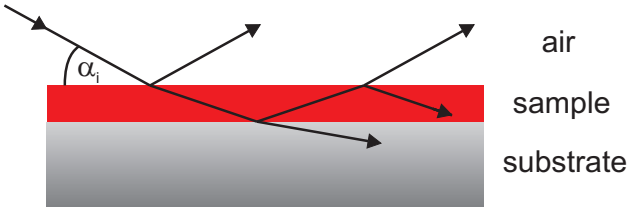

Figure 3.2: Beam path of X-rays at the air/sample/substrate interfaces.

transmitted beam is refracted at the air/sample interface, whereas the angle of refraction is determined by the refractive indices of these media. If the refracted beam hits the substrate or another layer of different refractive index, the beam is again reflected and transmitted. This leads to a path difference between the different propagating waves, which is dependent on the thickness of the sample. The interfering waves are detected at an angle equal to the incident angle. Constructive and destructive interference of the X-rays leads to oscillations (Kiessig fringes) in the observed intensity upon the variation of the incident angle. From this reflectivity curve, the film thickness, roughness, and density of the material can be derived. For this purpose, a theoretical reflectivity curve can be calculated and fitted to the experimental data. If such a fit was not feasible in this work, the film thickness was calculated using equation 3.1.

The calculated reflectivity profiles for a single layer and a multilayer system are shown in Figure 3.3. In the reflectivity curve of the single layer system an even dis-

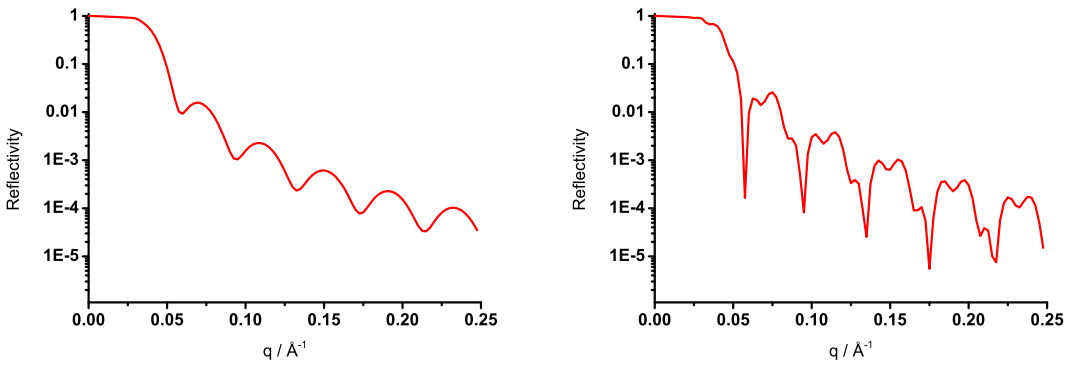

Figure 3.3: Simulated reflectivity curves for a single layer system (15 nm TiO_2 - left) and for a multilayer system (15 nm TiO_2/30 nm poly(styrene) - right).

tribution of Kiessig fringes can be found. The typical shape of a multilayer system shows a superposition of the signals of two separate layers. For thin layers the film thickness t can be obtained by the distance Δq between two neighboring minima:

$$t = \frac{2\pi}{\Delta q} \tag{3.1}$$

As the wavelength of X-ray radiation is similar to the lattice spacing d of crystalline materials, X-ray diffraction (XRD) can be used to determine crystal structures and crystallite sizes. [145] Upon variation of the incidence angle, constructive interference occurs if the conditions meet Bragg's law:

$$n\lambda = 2d\, sin\Theta \tag{3.2}$$

This way, a characteristic diffraction pattern is obtained. The investigated material can be identified by it's unique set of lattice spacings, and the crystallite size can be estimated by the peak size broadening. [146]

XRR/XRD Setup

Manufacturer:	Seifert
Device:	XTD 3003 TT
Wavelength:	$\lambda = 0.154$ nm
Data Evaluation Software:	Parratt32

3.7 SAXS and GISAXS

Small angle X-ray reflectivity (SAXS) is a non destructive method to gain information on the morphology of polymers in bulk. [147] The technique is applicable to crystalline as well as amorphous materials. The measurements are conducted in a transmission geometry. As most of the X-ray beam passes the sample without interaction, a beamstop is used to avoid damage of the detector. Electron density variations in the sample scatter the X-rays, and the scattered image is detected on a 2-dimensional detector. To simplify the evaluation of the data, a scattering profile is extracted from the 2-dimensional scattering image to gain structural information of the sample. Depending on the morphology of the polymer, a characteristic SAXS pattern is obtained.

Grazing incidence small angle X-ray scattering (GISAXS) is a useful tool to investigate buried or inner structures in thin films [148]. A grazing incident angle, depending on the system to be studied, is chosen for the measurement. To make surface sensitive measurements, an incident angle below the critical angle of the material can be used. Working above the critical angle ensures that the sample is fully penetrated by the beam. Often synchrotron radiation sources are used for these measurements. The advantages of synchrotron SAXS beamlines are the small beam divergence, the high brilliance, and a higher flux compared to conventional X-ray sources. A 2-dimensional detector records the scattered intensity. The direct and the reflected beam are blocked by beamstops to avoid saturation or damage of the detector. Out-of-plane cuts are extracted from the scattering images to gain information on lateral features of the sample. GISAXS yields an averaged, statistical view of an area that is much higher compared to the one covered by microscopy techniques. For example, at an incident angle of 0.7° and a beamsize of 17 x 32 μm, the footprint of the beam is 45000 μm^2.

SAXS Setup

Anode:	Rigaku Micromax 007
Wavelength:	$\lambda = 0.154$ nm
Detector:	Bruker HI-STAR (1024 x 1024)
Sample-detector distance:	1.8 m

GISAXS Setup

Beamline:	BW4, HASYLAB, DESY, Hamburg, Germany
Wavelength:	$\lambda = 0.138$ nm
Angle of incidence:	0.7°
Beamsize:	17 x 32 μm
Detector:	MarCCD165 (2048 x 2048)
Sample-detector distance:	2 m

3.8 Characterization of Photovoltaics

Solar cells are characterized by recording current-voltage curves (IV curves) under standardized illumination. For this purpose, a radiation intensity of 100 mW/cm^2 in combination with the AM 1.5 G (air mass 1.5 global) solar spectrum is used. The AM 1.5 G spectrum corresponds to the spectral distribution of the global solar irradiation at sea level after passing the atmosphere 1.5 times. These conditions are often referred to as *1 sun*. An efficient device delivers a high power output rather than a high current flow or a high voltage only. Thus, a voltage sweep is carried out, and the photocurrent generated by the cell is measured to gain information on the power output. The IV curve of the silicon solar cell that was used to calibrate the solar simulator is shown in Figure 3.4. The short-circuit current (I_{SC}) is defined as the current that is measured under short-circuit conditions, i.e. when the voltage equals zero. The I_{SC} yields information on how efficiently the photogenerated charges are generated. The open-circuit voltage (V_{OC}) is the voltage generated by the cell when no external load is present. The V_{OC} is related to the work function of the electrode materials. It yields information on how efficiently charges are separated.

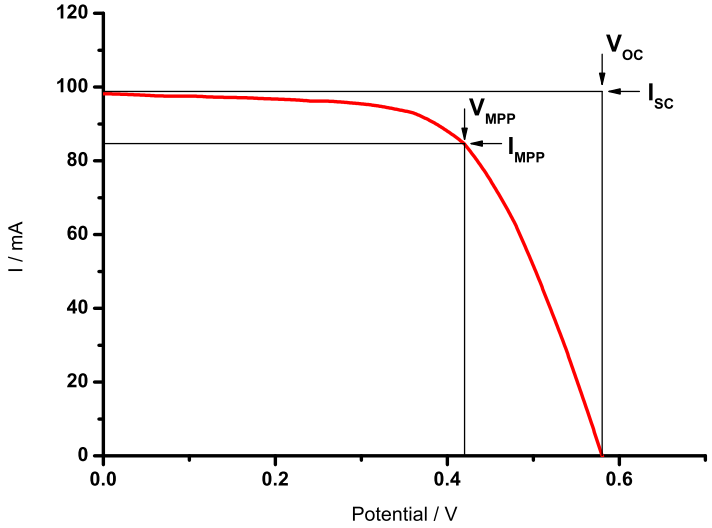

Figure 3.4: IV curve of the silicon solar cell used for calibration (cell area = 4 cm^2).

The fill factor (FF) is the ratio of the maximum power delivered by the solar cell and the product of the I_{SC} and the V_{OC}:

$$FF = \frac{I_{MPP} \cdot V_{MPP}}{I_{SC} \cdot V_{OC}} \tag{3.3}$$

The FF can be interpreted graphically as the ratio of the rectangular areas depicted in the IV curve. The main parameter characterizing a solar cell is the power conversion efficiency η, defined as the ratio of the electrical power output generated by the cell P_{OUT} and the incident radiation power P_{IN}:

$$\eta = \frac{P_{OUT}}{P_{IN}} = \frac{I_{SC} \cdot V_{OC} \cdot FF}{P_{IN}} \tag{3.4}$$

Thus, to optimize the efficiency of a solar cell, each of these parameters, the I_{SC}, the V_{OC}, and the FF have to be maximized.

The equivalent circuit for a real (non-ideal) solar cell is shown in Figure 3.5. The model consists of a current source and a diode describing the pn-junction in the device. The parallel shunt resistance (R_P) describes deviations from the perfect diodic behavior. The series resistance (R_S) represents the resistance occurring at the interfaces between the different layers of the solar cell. The influence of the variation

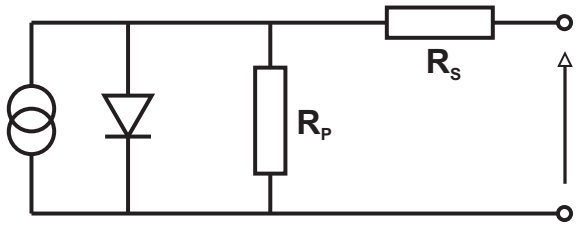

Figure 3.5: Equivalent circuit for a real solar cell (adapted) [22].

of R_P and R_S on the IV curve is visualized in Figure 3.6. A decrease in the parallel shunt resistance reduces the V_{OC} as well as the fill factor while the I_{SC} remains basically unaffected. On the other hand, an increased series resistance leads to a lower fill factor and a lower I_{SC} without affecting the V_{OC}. Ideally, the parallel shunt resistance should be as high as possible to allow charge transport in one direction only. At the same time, the series resistance should be as low as possible to avoid current loss. The values for the series resistance as well as for the parallel shunt resistance can be derived from the inverse slopes of the IV curves at the points of the V_{OC} and the I_{SC}, respectively. [149]

To simplify the comparison between different devices, the IV curves are normalized by the cell area, hence, current density-voltage curves (JV curves) are shown in the following work.

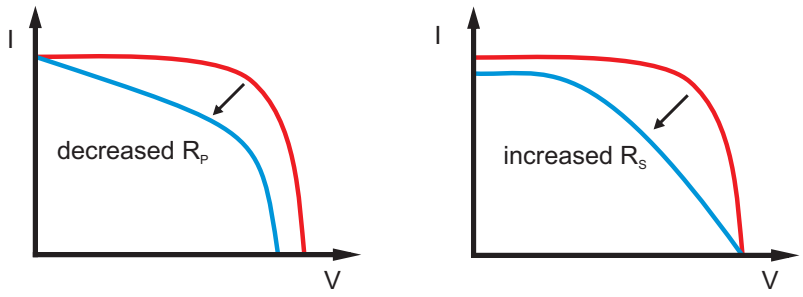

Figure 3.6: Influence of R_P (left) and R_S (right) on the shape of the IV curve.

Solar Simulator Setup

Lamp:	LOT-Oriel, Xenon short-arc lamp
Irradiance:	1 sun (100 mW/cm^2)
Spectrum:	AM 1.5 G
Temporal Stability:	1 %
Source measurement unit:	Keithley 2400 digital sourcemeter

4 Experimental

4.1 Diblock Copolymer Synthesis

The diblock copolymer poly(ethylene oxide)-block-poly(dimethylsiloxane)methylmethacrylate (PEO-MA(PDMS)) was synthesized by ATRP of functionalized PEO and poly(dimethylsiloxane)methylmethacrylate (MA(PDMS)) (ABCR Chemicals) as depicted in Figure 4.1. Anionic polymerization of ethylene oxide was initiated by potassium isopropoxide in tetrahydrofuran (THF) to yield living poly(ethylene oxide) (1). 2-bromo-2-methylpropionylbromide (distilled under vacuum before use) was added to the solution in the glovebox, and the reaction was stirred for 3 days at room temperature. The bromide salt was removed by centrifugation (4000 rpm, 10 min.) followed by decantation. The PEO macro starter (2) was precipitated two times in petrol ether. After drying over night at 40 °C in vacuum, a white powder was obtained.

For the polymerization of the diblock copolymer, the PEO macro starter (2 g) was dissolved in anisole (20 ml) and purged with argon for 15 minutes for degassing. CuBr (43.7 mg) and N, N, N', N', N"-pentamethyldiethylenetriamine (PMDETA, 63.6 μl) were added. For the first batch 2.49 ml and for the second batch 4.27 ml MA(PDMS) macro monomer were added under argon flow. The solution was frozen in liquid nitrogen and 3 freeze-pump-thaw cycles were applied to remove residual oxygen. The reaction was left for 10 days at 93 °C, then, the polymerization was stopped by exposure to air. The green solution was diluted with THF (20 ml), DOWEX ion exchanger was added, and it was stirred until the green color disappeared. The clear solution was filtrated by passing through an Al_2O_3 column, centrifuged (4000 rpm, 10 min.), and decanted. To remove residual educts, the

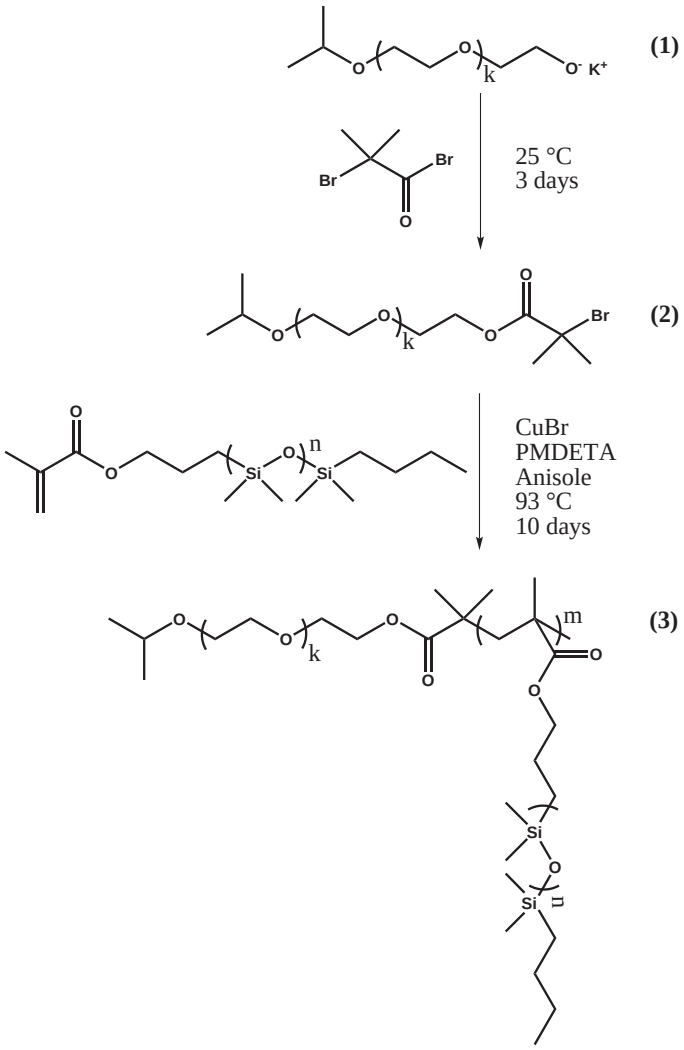

Figure 4.1: Atom transfer radical polymerization of PEO-MA(PDMS).

product was purified by ultrafiltration with THF (250 ml per cycle). For this purpose, a membrane (Millipore) with a nominal molecular weight limit of 10000 g/mol was used. After evaporation of the solvent, the diblock copolymer (3) was obtained as a colorless, viscous liquid. The yield was 1.820 g (41 %) for the first and 3.250 g (53 %) for the second batch.

4.2 Blocking Layer Preparation

For the preparation of the hybrid blocking layer the approach developed by Memesa et al. was followed. [100] However, the triblock copolymer was replaced by the newly

synthesized diblock copolymer. In detail, PEO-MA(PDMS) diblock copolymer (20 mg) was dissolved in THF (1500 mg) and isopropanol (500 mg). After adding titanium tetraisopropoxide (200 mg) (TTIP) and HCl (37 %, 20 mg), the solution was left to stir for 1 hour. Films were spin coated on silicon wafers and FTO substrates (2000 rpm, 2000 rpm/s, 30 s). For the plasma etching treatment, the substrates with the nanocomposite films were etched in an argon plasma at 20 mbar and 300 W for 10 minutes. For the vapor annealing treatment, the samples were stored in a desiccator containg a reservoir of THF for 90 minutes. The films were calcined in a nitrogen atmosphere at 450 °C for 2 hours with a heating rate of 6.25 °C/min starting from room temperature.
Following the method by Yu et al., the compact TiO_2 blocking layers were prepared by spin coating of an organic sol. [150]

4.3 Solar Cell Assembly

4.3.1 Liquid Electrolyte Based DSSCs

FTO substrates (AGC Fabritech, Japan, sheet resistance $< 12\ \Omega$/sq) were immersed in Alconox detergent solution and cleaned by ultrasonication for 15 minutes. The substrates were rinsed with distilled water and ethanol and dried in a flow of N_2. The blocking layers were spin coated as described in Section 4.2. After the application of the blocking layer, the substrates were put into an aqueous $TiCl_4$ solution (40 mM) and heated to 70 °C for 1 hour. The mesoporous TiO_2 layer was applied on top of the blocking layer by doctor blading a titania paste (Solaronix, Ti-Nanoxide T). The film thickness of the mesoporous titanium dioxide layer determined by profilometry was $\sim 3\ \mu$m. Immediately after the coating process, the films were put on a hot plate (70 °C) for 5 minutes. Subsequently, the films were sintered in air at 450 °C for 30 minutes. After cooling down to 80 °C, the samples were immersed into a 0.3 mM solution of the ruthenium dye Z907 (Dyesol) in a mixture of acetonitrile and t-butanol (v/v 1:1) for at least 12 hours. Residual dye solution was washed away by rinsing the substrates with dry acetonitrile. The films were dried in N_2

flow. The counter electrodes were prepared by sputtering a 30 nm thick platinum layer on clean FTO substrates. A 250 μm thick teflon ring served as spacer between the front and the back electrode. A I^-/I_3^- redox couple (0.03 M I_2, 0.3 M LiI, 0.5 M 4-tert-butylpyridine) in dry acetonitrile and an ionic liquid (Iolitec, Iolilyt SB-163) were used as electrolyte, respectively. The electrolyte solution was applied on the front electrode, which was fixed together with the back electrode using clamps.

4.3.2 Solid-State DSSCs

FTO substrates were patterned by etching away part of the conducting layer with zinc powder and HCl (18 %). Subsequently, the substrates were cleaned, and the blocking layer as well as the mesoporous titania layer were applied as described in Chapter 4.3.1. The titania paste (Dyesol, DSL-18NR-T) used for doctor blading was diluted with ethanol (1 g: 1.5 mL). The film thickness of the mesoporous TiO_2 layer determined by profilometry was $\sim$ 2 μm. The films were sintered for 30 minutes in air at a temperature ramped in 90 minutes to 500 °C. After cooling down, the samples were immersed in a 70 °C warm 30 mM solution of $TiCl_4$ in water for 70 minutes. Before another sintering step at 500 °C for 45 minutes, the samples were rinsed with water and dried with N_2. The following dye-uptake is described in Chapter 4.3.1. The hole-transport material used was spiro-OMeTAD (Merck, 14 vol% in chlorobenzene). Lithium-bis(trifluoromethylsulfonyl)imide (Li-TFSI) salt was pre-dissolved in acetonitrile (170 mg/ml) and added to the hole-transport solution. For every 73 mg of spiro-OMeTAD 7 μl of 4-tert-butylpyridine and 15 μl of Li-TFSI-solution was added. The hole-transport layer was applied by spin coating at 1500 rpm after letting it soak for 30 seconds. Silver/gold counter electrodes were deposited by evaporating 15 nm Ag/Au using a shadow mask.

5 Results and Discussion

5.1 PEO-MA(PDMS) Block Copolymer

The length scale of block copolymer phase separation is in the same order of magnitude as the exciton diffusion length. [124] This makes titanium dioxide films, templated by block copolymers, ideally suited for the preparation of materials designated for the application in photovoltaics. Typically, the mesoporous titania layer in DSSCs is prepared through the self assembly of block copolymers. In this thesis, the titanium dioxide within the blocking layer is templated. For the preparation of the hybrid blocking layer, an amphiphilic block copolymer, containing a hydrophilic PEO block and a hydrophobic PDMS block, is used.

5.1.1 Synthesis

Since anionic polymerization is a widely used technique for the synthesis of PEO as well as for PDMS, the first approach to link these polymers was by successive anionic polymerization. [151] An alcoholate of PEO was reacted with hexamethyltricyclosiloxane and, vice versa, an alcoholate of PDMS was reacted with PEO. In both cases only low molecular weight products were obtained. A successful route to link PEO and PDMS was achieved by using atom transfer radical polymerization, thus, the amphiphilic diblock copolymers used in this thesis have been synthesized by ATRP of PEO and MA(PDMS).

Termination of the living PEO with 2-bromo-2-methylpropionylbromide resulted in a PEO macro starter with a number average molecular weight of 7000 g/mol and a polydispersity of 1.16. The low polydispersity is a sign for a successful anionic polymerization. This macro starter was reacted with two different amounts

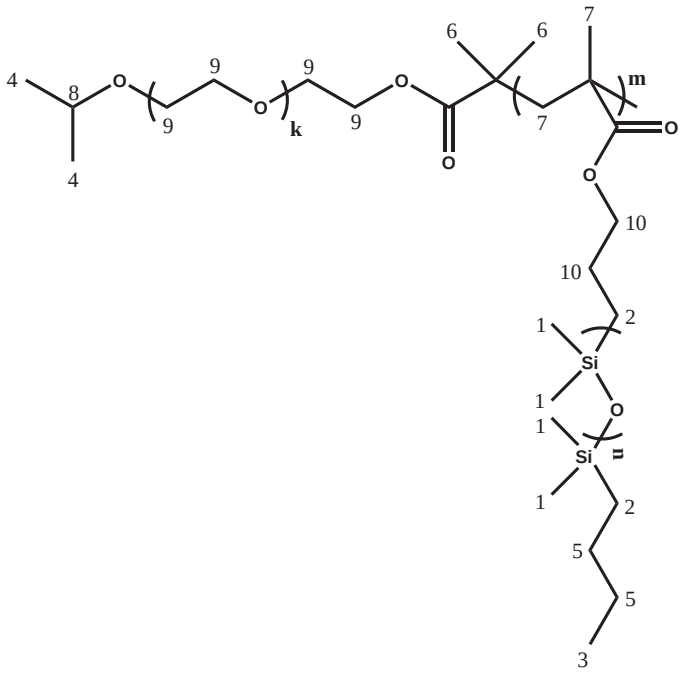

^{1}H-NMR (PEO-MA(PDMS), 250 MHz, $CDCl_3$, δ): 0.05 (PDMS backbone, **1**), 0.51 (m, 4 H, **2**), 0.86 (t, J = 1 Hz, 3 H, **3**), 1.14 (d, J = 5 Hz, 6 H, **4**), 1.29 (m, 4 H, **5**), 1.41 (s, 6 H, **6**), 1.90 (PMMA backbone, **7**), 3.34 (m, 1 H, **8**), 3.62 (PEO backbone, **9**), 3.88 (m, 4 H, **10**).

Figure 5.1: ^{1}H-NMR data of PEO-MA(PDMS).

of MA(PDMS) to yield two batches of the amphiphilic diblock copolymer. For the purpose of simplification, the first batch of PEO-MA(PDMS) will be referred to as *Polymer1*, and the second batch of PEO-MA(PDMS) will be referred to as *Polymer2*, hereafter. In Figure 5.2 and Figure 5.3 the GPC and ^{1}H-NMR spectra of Polymer1 and Polymer2 are shown, respectively. After successful polymerization, the products were purified by ultrafiltration to remove residual educts. This step was repeated as long as the vinyl peaks of the macro monomer at δ = 5.52 ppm (s, 1H) and δ = 6.08 ppm (s, 1H) disappeared in the ^{1}H-NMR spectra (Figure 5.1). The chromatograms show narrow and monomodal molecular weight distributions. The first batch yielded a diblock copolymer with a number-average molecular weight (M_N) of 19000 g/mol and a polydispersity (PDI) of 1.14. After the reaction of the second batch, the product was obtained with a number-average molecular weight of 14000 g/mol and a polydispersity of 1.46. The properties of both polymers are summarized in Table 5.1. ATRP is a controlled living radical polymerization. The

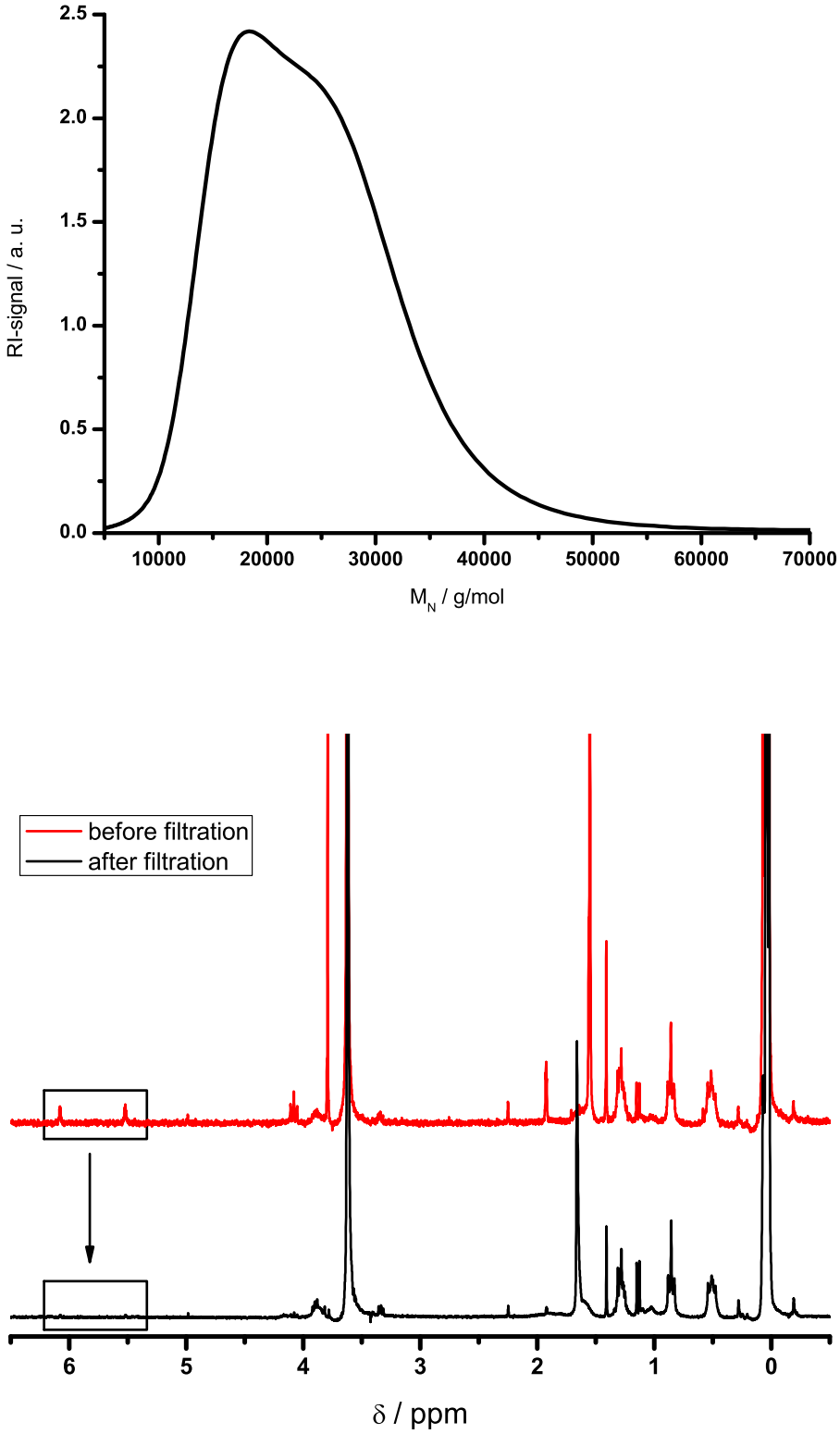

Figure 5.2: GPC (top) and ^{1}H-NMR (bottom) spectra of Polymer1.

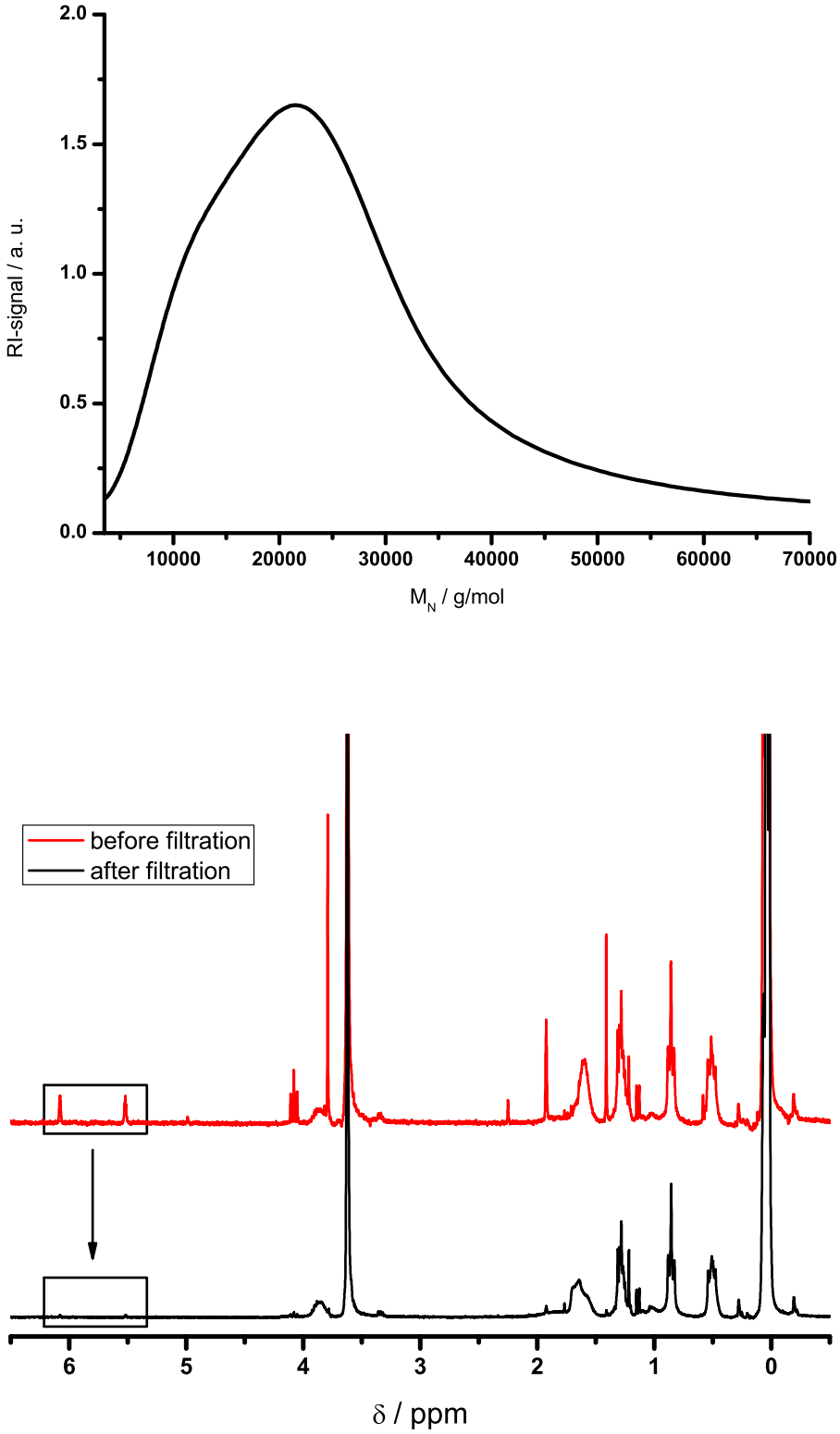

Figure 5.3: GPC (top) and ^{1}H-NMR (bottom) spectra of Polymer2.

Table 5.1: Properties of Polymer1 and Polymer2.

Label	M_N	PDI	M_N(PEO)	M_N(PDMS)	M_N(PEO)/M_N(PDMS)
Polymer1	19000 g/mol	1.14	7000 g/mol	12000 g/mol	1 : 1.7
Polymer2	14000 g/mol	1.46	7000 g/mol	7000 g/mol	1 : 1

chains grow simultaneously, and therefore the narrow molecular weight distribution from the PEO macro starter is preserved in the diblock copolymer. The block length ratio of the PEO block to the PDMS block is the most important factor influencing the phase separation morphology of the polymers. In the first batch the molecular weight ratio of PEO to PDMS was $\sim$ 1:2, and in the second batch the molecular weight ratio of PEO to PDMS was $\sim$ 1:1.

5.1.2 SAXS

Small angle X-ray scattering (SAXS) is a useful tool to determine the microdomain structure of soft matter. Due to the amphiphilic character of PEO-MA(PDMS), the diblock copolymer is expected to show strong phase separation. Both batches of PEO-MA(PDMS) were investigated by SAXS to gain structural information on the morphologies of the polymers in bulk. The SAXS curves with Gaussian fits for both batches of PEO-MA(PDMS) are shown in Figure 5.4. Both patterns show higher order reflections at integer multiples of the q-value of the first order peak. This spacing sequence is an indication for a lammellar ordering of the blocks. [152] The peaks are positioned at the same q-values for both batches. The main peaks are located at q = 0.59 nm^{-1} resulting in a d-spacing of 11 nm. This spacing corresponds to the distance between the lammelle. For Polymer2, a third, broad peak of low intensity can be found, additionally. This is a hint for the existence of a mixture of different (lamellar) phases.

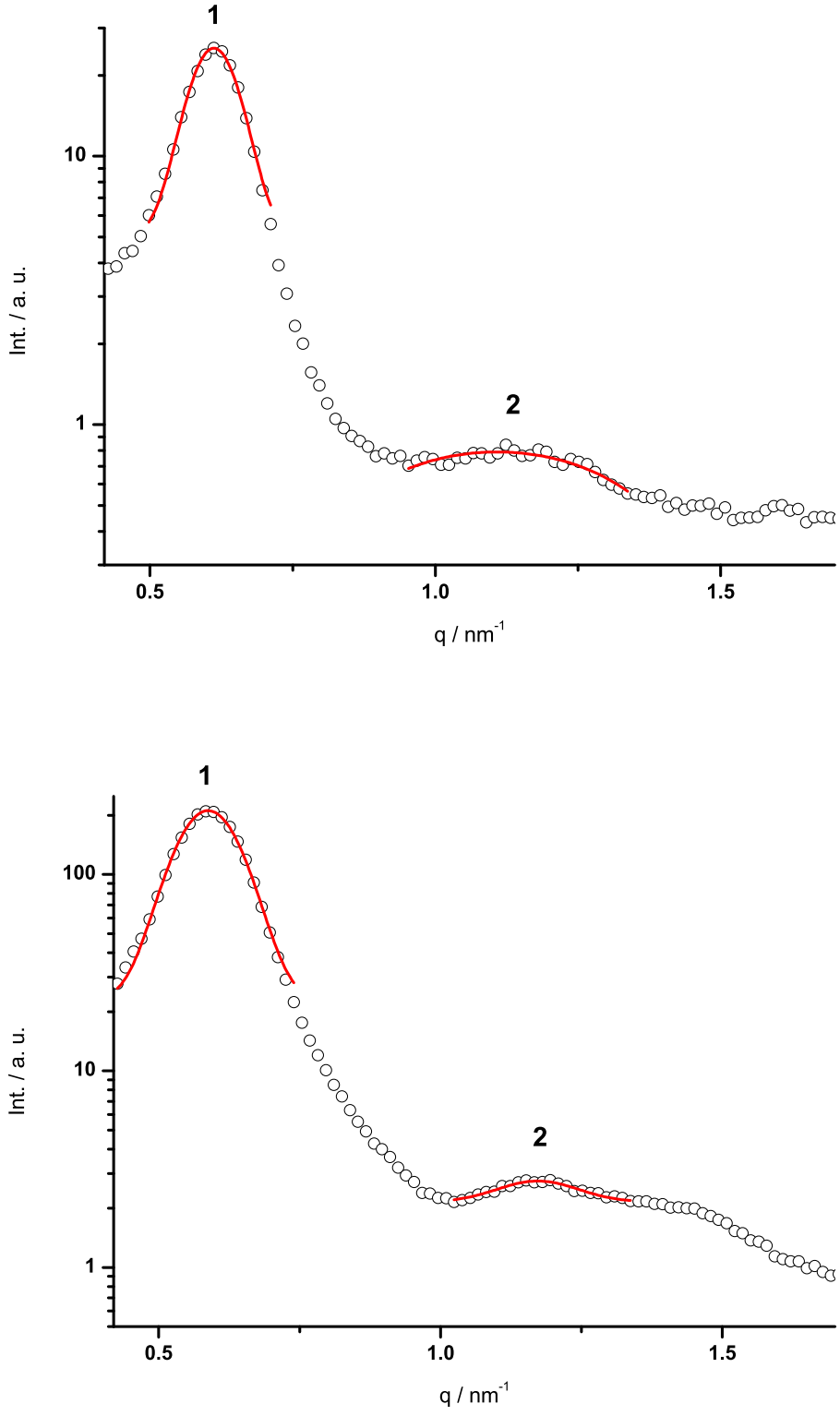

Figure 5.4: SAXS patterns with Gaussian fits of Polymer1 (top) and Polymer2 (bottom).

5.1.3 Scanning Force Microscopy

Scanning force microscopy was used to investigate the morphology of both polymers in thin films. The samples were prepared by dissolving the polymers in THF (20 mg Polymer/1500 mg THF) and spin coating the solution on silicon substrates. Figure 5.5 shows height and phase images of the two batches of PEO-MA(PDMS). In the height and phase image of Polymer1 (Figure 5.5, A and C) a wormlike struc-

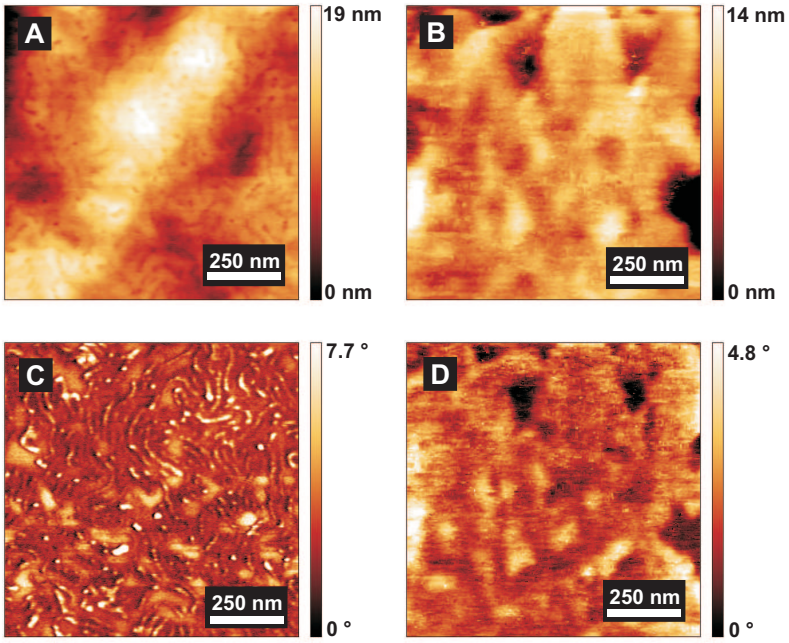

Figure 5.5: Height (top) and phase (bottom) SFM images of Polymer1 (left) and Polymer2 (right) spin coated on silicon substrates.

ture (RMS roughness = 3.3 nm) is visible. The strong contrast in the phase image indicates the existence of both blocks, i.e. the PEO block and the PDMS block of the amphiphilic polymer, at the surface of the film. The SAXS measurement of Polymer1 showed a lamellar structure in bulk, thus, the morphology of the spin coated film is different. In the height image of Polymer2 (Figure 5.5, B) no distinct microphase segregation can be found (RMS roughness = 2.3 nm). Also, the phase image (Figure 5.5, D) exhibits a low phase contrast. This might be due to the fact that only one block of the diblock copolymer is exposed at the surface of the film. This finding is consistent with the results obtained from the SAXS measurement

that indicated a lammellar ordering of the blocks. Thus, a bilayer structure, which is arranged parallel to the substrate surface, is found for Polymer2.
The morphologies of the diblock copolymers obtained by SAXS and SFM measurements are only a hint to the structure of the hybrid nanocomposite films. In addition to the block length ratio, in sol-gel chemistry the amount of acid, solvent, and the polymer-to-precursor ratio can strongly influence the morphology of the resulting films. This way, the morphology of the polymer in bulk does not limit the range of structures produced. Using sol-gel chemistry, a variety of morphologies is accessible with the same polymer.

5.2 The Conventional Blocking Layer

As mentioned in Chapter 2.2, two major methods are established in the preparation of the conventional blocking layer. Compact films of titanium dioxide can be produced by spin or dip coating from sol-gel mixtures or by spray pyrolysis of an aerosol containing a TiO_2 precursor. The drawback of the blocking layer prepared by spray pyrolysis is the requirement of a sophisticated setup. Furthermore, the reproducibility, the control over the film thickness, and the coating of large substrates is complicated. It has been found that both preparation methods yield blocking layers with essentially the same functionality. [89] For these reasons the *conventional* blocking layer is prepared by spin coating a sol-gel mixture in this work.

5.2.1 Film Thickness

A cross section SEM image and a XRR curve of the conventional blocking layer are shown in Figure 5.6. In the SEM image the boundaries of the compact TiO_2 film are marked by dotted lines to distinguish between the different layers. The titanium dioxide covers the rough FTO substrate completely. The layer is crack-free and exhibits no holes. Thus, the film successfully separates the FTO electrode from the hole-transport material in a solar cell device. On FTO, the film thickness varies locally due to the high roughness of the substrate, and this leads to peak-to-

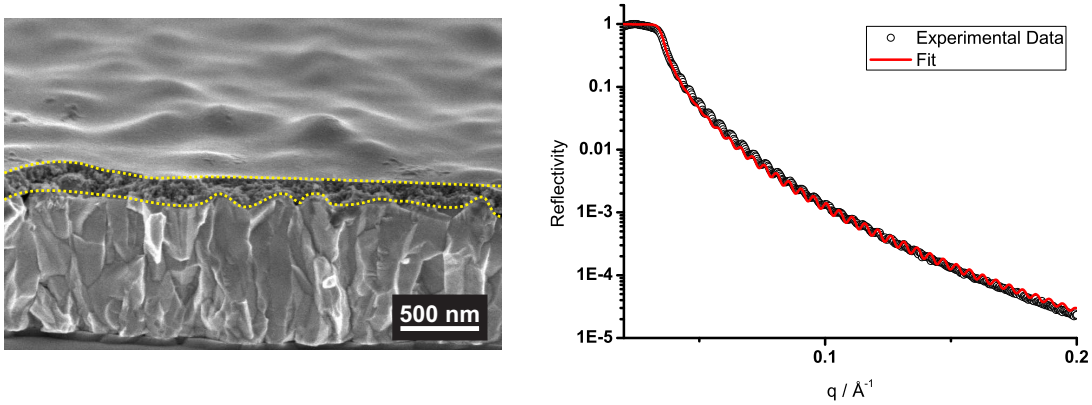

Figure 5.6: SEM cross section image (left) and XRR curve (right) of the conventional blocking layer. The SEM sample was prepared on FTO, the XRR curve was measured on a flat silicon wafer.

valley values between 100 and 200 nm. The X-ray reflectivity profile shows an even distribution of Kiessig fringes. This is an indication for a homogeneous, single layer system consisting of one material only. The nominal X-ray reflectivity measurements of the conventional blocking layer on flat silicon wafers resulted in a thickness of 121 nm. Hence, the thickness of the conventional blocking layer lies in the range between 120 and 200 nm designated by Peng et al. to yield the best performance in solar cell devices.

5.2.2 Crystallinity

For the electron transport, the crystallinity and the crystal structure of the titanium dioxide are important. The conventional blocking layer is prepared by spin coating of a sol-gel mixture containing the TiO_2 precursor titanium butoxide. The spin coated film is sintered at 450 °C for 2 hours allowing the yet amorphous titanium dioxide to crystallize in the anatase polymorph. Figure 5.7 shows the XRD pattern of a drop casted sample of the conventional blocking layer. The XRD profile shows a single, crystalline anatase phase. No rutile or brookit signals are visible in the XRD pattern, nor a broad halo that would indicate the presence of amorphous material. The size of the titania crystals can be estimated by the Scherrer equation for peak

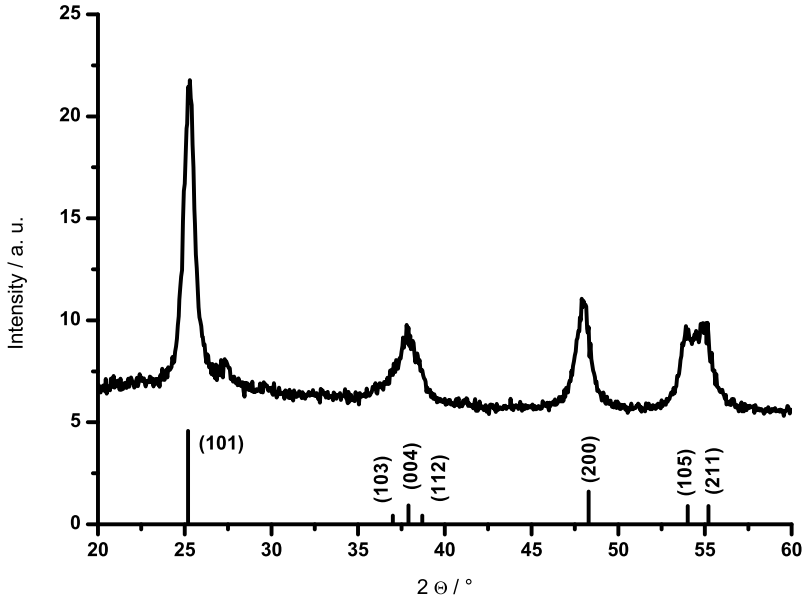

Figure 5.7: XRD pattern of the sol-gel mixture used for the conventional blocking layer with anatase reference peaks. [153]

size broadening. [146] Evaluating the most intense peak at $2\Theta = 25.25°$, with respect to the full width at half maximum of the primary beam, yields a crystallite size of 12 nm. This finding is consistent with results found by other groups where the crystal size was reported to lie in the range between 10 and 20 nm. [150] Thus, the applied thermal treatment is sufficient for the amorphous TiO_2 to crystallize completely in the anatase polymorph. This guarantees for optimal charge transport in photovoltaic applications.

5.2.3 Conductive SFM

The conventional blocking layer, prepared on platinum-coated silicon substrates, was characterized by conductive scanning force microscopy (Figure 5.8, A and B). The height map (Figure 5.8, A) of the compact TiO_2 film shows a smooth and granular structure (RMS roughness = 0.3 nm). The conductivity of the film (Figure 5.8, B) is not homogeneous across the surface. Small circular spots of high current flow show up, which are surrounded by areas of low current flow or insulation. This is

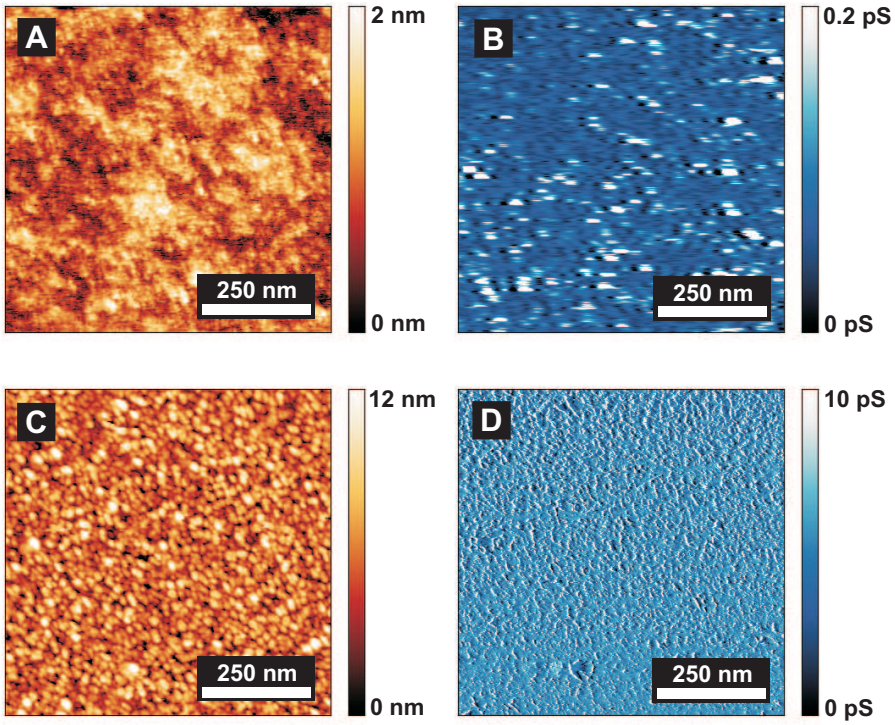

Figure 5.8: Height (left) and current (right) SFM images of the conventional blocking layer (top, applied voltage 3.1 V) and a Pt-coated silicon wafer (bottom, applied voltage 1.0 V).

surprising, because a crystalline, smooth, bulk titanium dioxide layer is expected to show a homogeneous conductivity even on the microscopic scale.

As a reference for a bulk conducting material, conductive scanning force microscopy images of a 30 nm thick platinum layer on a silicon substrate prepared by sputtering are shown as well. The height image (Figure 5.8, C) of the platinum layer shows a more coarse-grained structure with a higher roughness compared to the titanium dioxide film (RMS roughness = 2.0 nm). Furthermore, the current image (Figure 5.8, D) looks fairly different. The current image of the platinum film shows only slight variations in the current flow, and the layer exhibits a more homogeneous conductivity throughout the surface of the film.

This means that the titanium dioxide film, prepared by spin coating of the sol-gel mixture, does not result in a homogeneous conducting layer like bulk conducting materials do. Areas of low conductivity in the blocking layer may originate from residuals of the organic TiO_2 precursor used in the preparation of the film. These ar-

eas may be disadvantageous for the application in solar cell devices, because charge transport will take place in the areas of low resistance.

Here we define the *active area* to include all data points with a conductivity value above 50 % of the data scale. Thus calculated, the active area is 12 % for the compact titanium dioxide film and 61 % for the pure platinum layer. This shows a drawback of the conventional blocking layer, because only a fraction of the entire film surface will serve for charge transport, actually.

5.3 The Hybrid Blocking Layer

In contrast to pure inorganic blocking layers, the crack formation in thin films that occurs during the sintering process can be avoided by using a hybrid material (see Chapter 2.2). The hybrid blocking layer investigated in this thesis is prepared by spin coating a sol-gel mixture containing the amphiphilic diblock copolymer PEO-MA(PDMS) and the TiO_2 precursor TTIP as shown in Figure 5.9. Films were

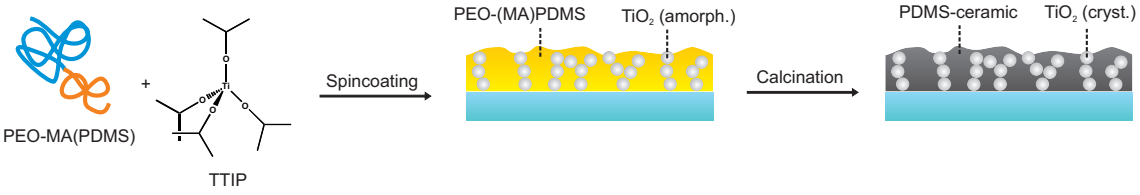

Figure 5.9: Schematic representation of the preparation of a hybrid film using sol-gel chemistry.

prepared on silicon wafers and FTO substrates. In this approach the hydrophilic PEO part of the polymer coordinates with the TiO_2 precursor to build up the inorganic TiO_2 network. The PDMS part ceramizes during a calcination step in inert atmosphere and turns into an organic glass, i.e. a carbon-containing silicate glass. [154] At the same time, the polymer acts as a cross linking agent and fills up voids in the film that may occur upon drying or sintering.

After the spin coating of the sol-gel mixture, the TiO_2 particles at the surface of the film may be (partially) covered by the polymer. During the calcination the polymer turns into an insulating ceramic material, and TiO_2 particles that were covered by

polymer are electrically insulated on the top of the blocking layer. For the application in solar cells it is particularly important that the conducting TiO_2 network is exposed at the surface of the film, so that electrons can be transported to the FTO electrode. Therefore, before the calcination of the film, one additional step is used to unveil the TiO_2 network, thereby improving the conductivity of the layer. A plasma etching treatment presented by Memesa et al. has established to expose the TiO_2 network to increase the conductivity of the hybrid films. [100] Another, novel approach introduced in this work is to use solvent vapor annealing to improve the structure of the hybrid blocking layer films before the calcination step. The preparation of the hybrid blocking layer including the plasma etching step is subject of Chapter 5.4. For this approach, Polymer1 with a molecular weight ratio of PEO to PDMS of 1:2 was used, exclusively. In Chapter 5.5, the preparation of the hybrid blocking layer using solvent vapor annealing is described. For this purpose, Polymer2 with a molecular weight ratio of PEO to PDMS of 1:1 was used, exclusively.
In addition to the block length ratio of the templating polymer, the structure of the hybrid blocking layer is affected by the composition of the sol-gel mixture. The ratio of polymer to TiO_2 precursor (TTIP) and the amount of acid (HCl) used in the sol-gel process is critical for the structure of the resulting film. Three major compositions of the sol-gel mixture have been investigated. For the purpose of simplification, the different compositions will hereafter be referred to as composition *A*, *B*, and *C* as depicted in Table 5.2. Compositions A and C containing 1 wt%

Table 5.2: Different compositions of the sol-gel mixture.

Abbreviation	Polymer	TTIP	HCl
A	1 %	1 %	1 %
B	1 %	10 %	1 %
C	1 %	1 %	10 %

Polymer and 1 wt% TTIP, with respect to the amount of solvent, resulted in films containing 40 wt% titanium dioxide and 60 wt% of the polymer derived ceramic. Composition B containing 1 wt% Polymer and 10 wt% TTIP yielded blocking layer films containing 80 wt% titanium dioxide and 20 wt% of the polymer derived ce-

ramic after the calcination step. However, considering that the density of titanium dioxide is approximately twice the density of the ceramic material, the amount of TiO_2 is accordingly lower with respect to the volume ratio of the hybrid films.

5.4 Plasma Etching of the Hybrid BL

Argon is an inert gas and won't react with organic nor inorganic compounds when used in plasma etching. Instead, an argon plasma will decompose a material and wear it off homogeneously. Thus, argon plasma can be used as a mechanical ablation method. During this process, soft matter like polymers is ablated more quickly than hard, inorganic materials like titanium dioxide. Hence, this technique is used to expose the TiO_2 particles at the surface of the blocking layer prior to the calcination step as shown in Figure 5.10. Titanium dioxide particles that may be covered by

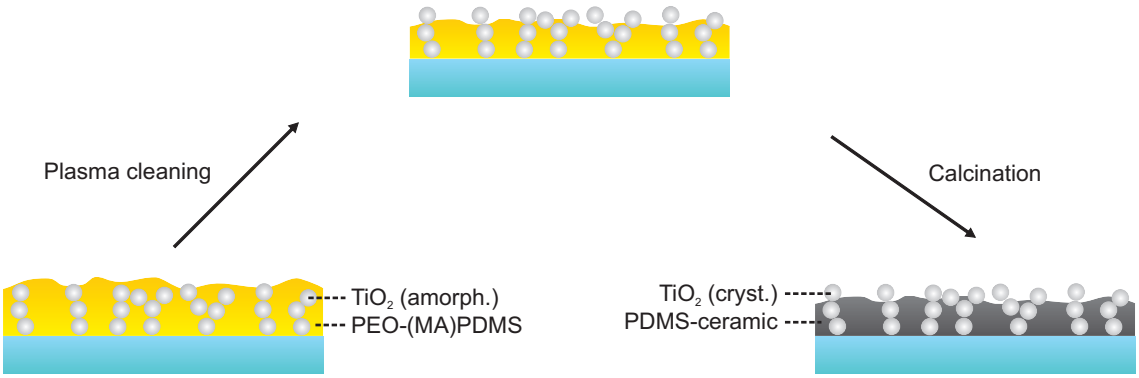

Figure 5.10: Schematic representation of the plasma etching step in the preparation of the hybrid blocking layer.

polymer after the spin coating of the sol-gel mixture are revealed by the plasma etching step, because the polymer is ablated more quickly by the argon plasma than the TiO_2. After the calcination step, the TiO_2 network turns crystalline and is exposed at the surface of the blocking layer. This way, the electron transport from the top of the blocking layer to the bottom FTO electrode is improved. [100]

5.4.1 Film Thickness

The X-ray reflectivity curves of the hybrid blocking layer of composition A after spin coating, after plasma etching, and after calcination are shown in Figure 5.11. The plasma treatment is used to remove a part of the organic layer in the hybrid

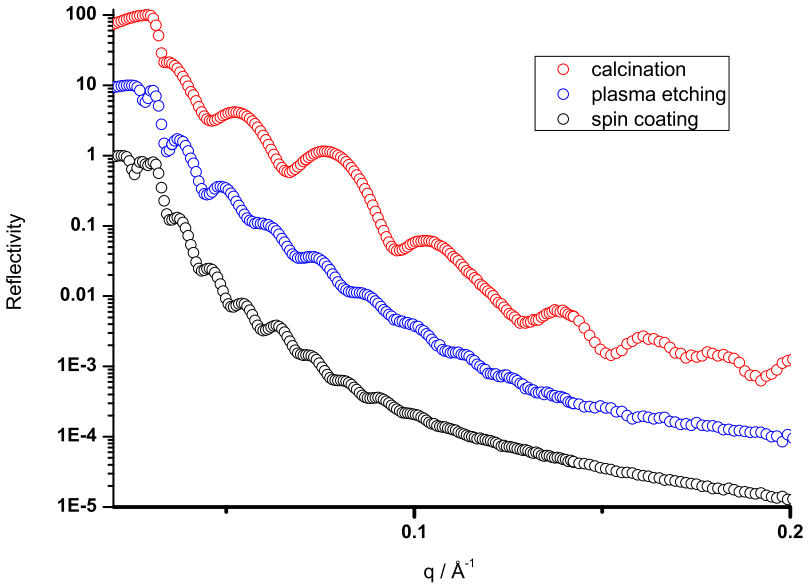

Figure 5.11: XRR curves of the hybrid blocking layer of composition A after spin coating, plasma etching, and calcination.

film. The XRR curves show that the film thickness is reduced from 72 nm after spin coating to 52 nm after the plasma etching step. The film thickness is again reduced in the calcination process. In this step, the polymer is pyrolyzed partially and turns into a glassy material. At the same time, the titanium dioxide sinters, turns crystalline, and a very thin film with a thickness of 24 nm is formed. In the X-ray reflectivity profile the amplitude and the distance of the Kiessig fringes is different. This suggests that the film consists of different, intermixed materials.
Figure 5.12 shows cross section SEM images and XRR curves of the finished blocking layer films of composition A, B, and C, respectively. The thickness for all three compositions of the hybrid films is significantly lower compared to the conventional blocking layer (see page 47, Figure 5.6). Still, all compositions of the hybrid blocking

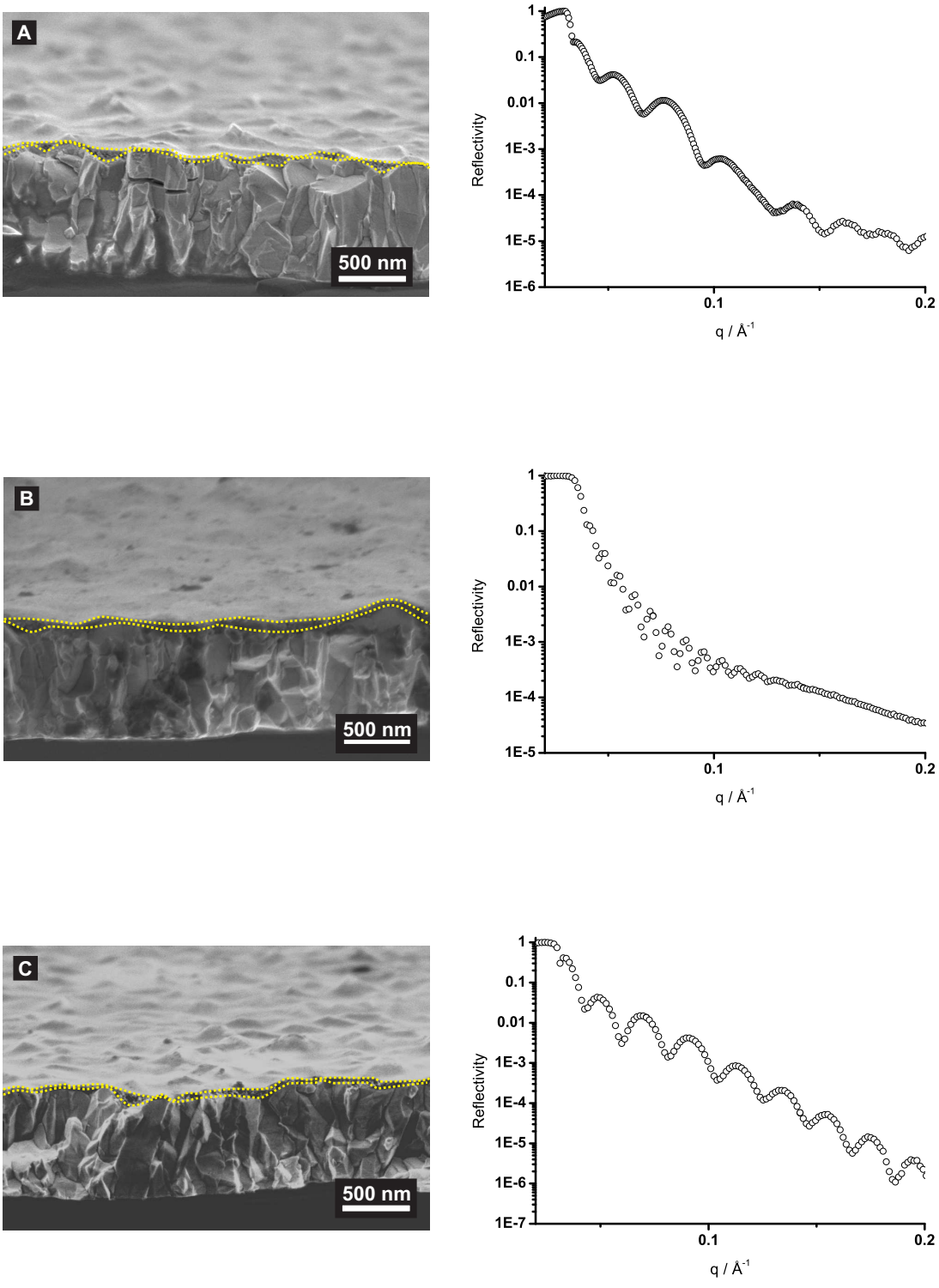

Figure 5.12: SEM cross section images (left) and XRR curves (right) of the hybrid blocking layer of composition A (top), B (middle), and C (bottom).

layer yield homogeneous, crack-free films without holes. This means that, despite being thinner than the conventional blocking layer, the hybrid films block recombination processes by separating the FTO electrode from the hole-transport material. Apart from the fact that the characteristic surface of the FTO is transferred to the hybrid layer, all films show very smooth surfaces. This is a result of the plasma etching process, which has a grinding effect on the film surface. The peak-to-valley values determined from the SEM images range from 10 to 90 nm for composition A, from 40 to 70 nm for composition B, and from 20 to 90 nm for composition C. Nominal thickness measurements on flat silicon wafers using X-ray reflectivity yield 24 nm, 68 nm and 29 nm, respectively. The film thickness for the blocking layer B is higher than for composition A and C. The preparation for all three layers is identical. However, in composition B the amount of TiO_2 precursor is the highest. The amount of precursor increases the viscosity of the sol-gel mixture. As a result of the spin coating process, these films are thicker than the other compositions. Nevertheless, approximately half the thickness of the conventional blocking layer is reached using this composition. Individual titanium dioxide particles in the hybrid material cannot be seen in the SEM images due to the low contrast between anatase and the ceramic material.

A thin lamella of the blocking layer of composition B with a thickness below 100 nm has been prepared using the focused ion beam (FIB). To increase the stability of the sample, a protective layer of platinum was deposited on top of the film. The lamella has been investigated by transmission electron microscopy (TEM), and electron spectroscopy imaging (ESI) was used to map the titanium (dioxide) amount throughout the lamella. The ESI/TEM images are shown in Figure 5.13. In the TEM image areas of high electron density, i.e. titanium dioxide, appear brighter than the organic material in the hybrid films. The titanium dioxide is not spread out homogeneously throughout the material. Most of it can be found at the bottom of the layer near the substrate. The titanium mapping by ESI suggests the same result. Only small amounts of titanium dioxide can be found in the upper part. That means only a small part of the conducting TiO_2 network is accessible at the surface of the film.

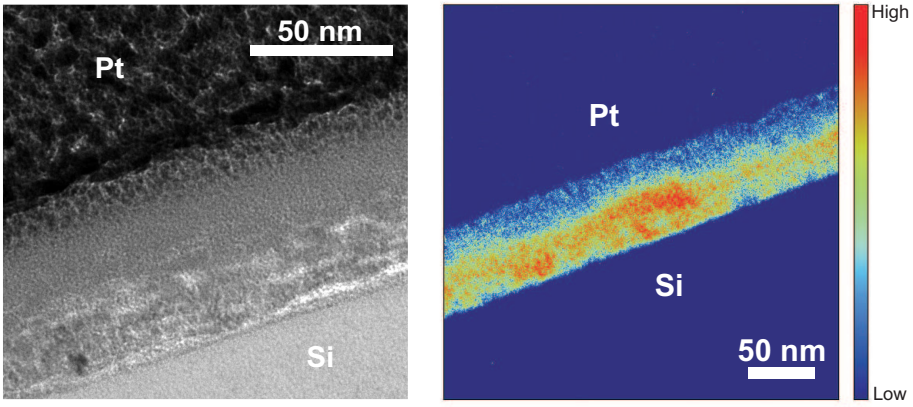

Figure 5.13: Focused ion beam prepared lamella of the hybrid blocking layer: TEM image (left) and titanium mapping by ESI (right).

In summary, a reduction of the film thickness down to 20 % of the conventional approach is possible using the hybrid material. Assuming similar conductivity for both materials, a significant increase of the conductance of the hybrid films compared to the pure TiO_2 film should be possible. A detailed characterization of the electrical properties of both blocking layers is subject of Chapter 5.4.4 and 5.4.5.

5.4.2 Film Structure

The investigation of the film structure by SFM and SEM techniques is restricted to the micrometer range and to the surface of the sample only. In contrast to these techniques, GISAXS offers the possibility to obtain information on the inner structure of the films over large areas. Working at a wavelength of $\lambda = 1.381\ \mathring{A}$, the incident angle of 0.7° used for the measurement is well above the critical angle of titanium dioxide ($\alpha_c = 0.25°$). Thereby, the whole sample is penetrated by the beam to reveal information on the inner structure of the material. The out-of-plane cuts of the GISAXS images yield information on the lateral structure of the hybrid films. Top-down view SEM images of the hybrid films are shown in Figure 5.14. For the SEM images flat silicon substrates were used, since on FTO substrates the characteristic structure of the FTO is transferred to the hybrid films making it difficult to recognize their fine structure. Figure 5.15 shows the GISAXS out-of-

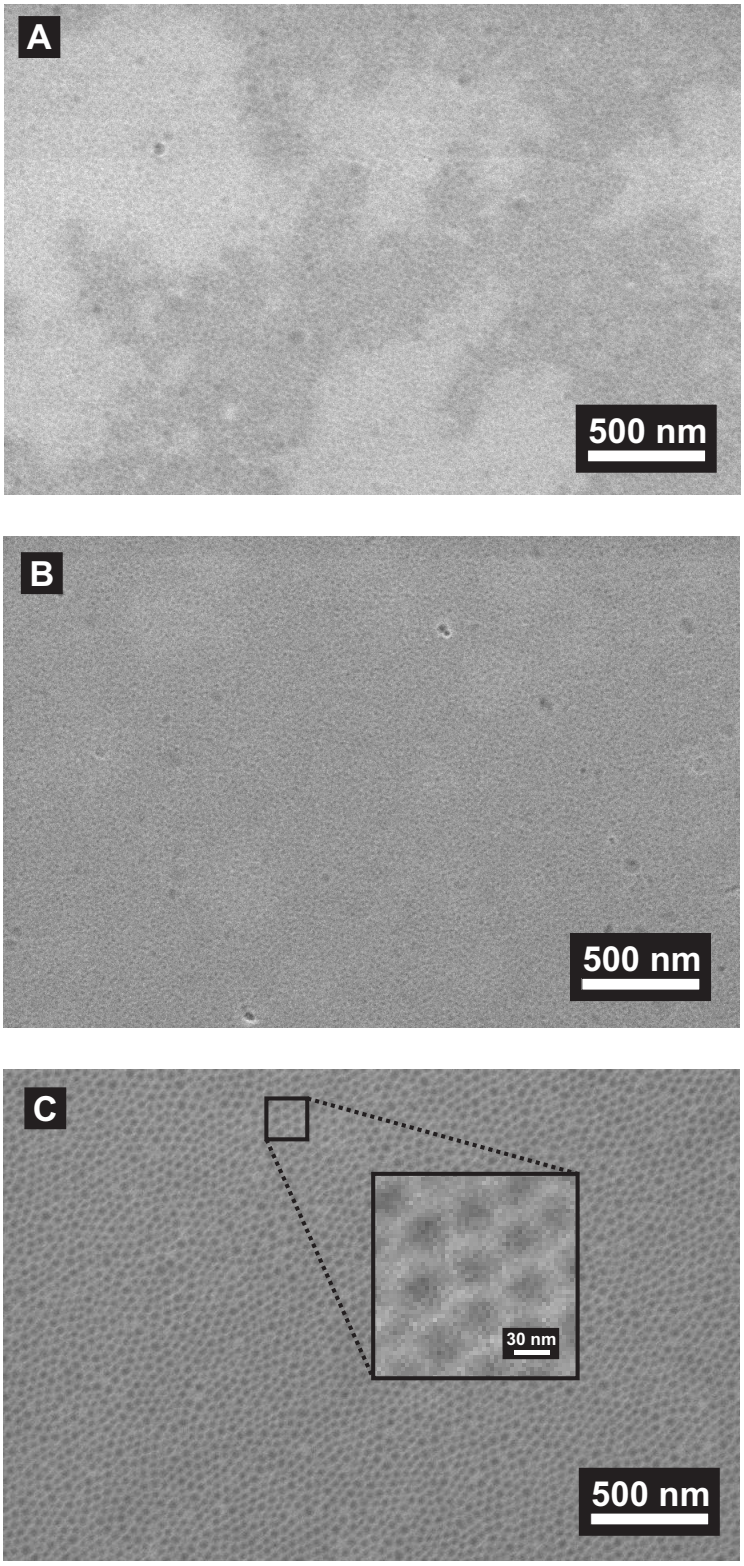

Figure 5.14: SEM top-down view images of the hybrid blocking layer of composition A (top), B (middle), and C (bottom).

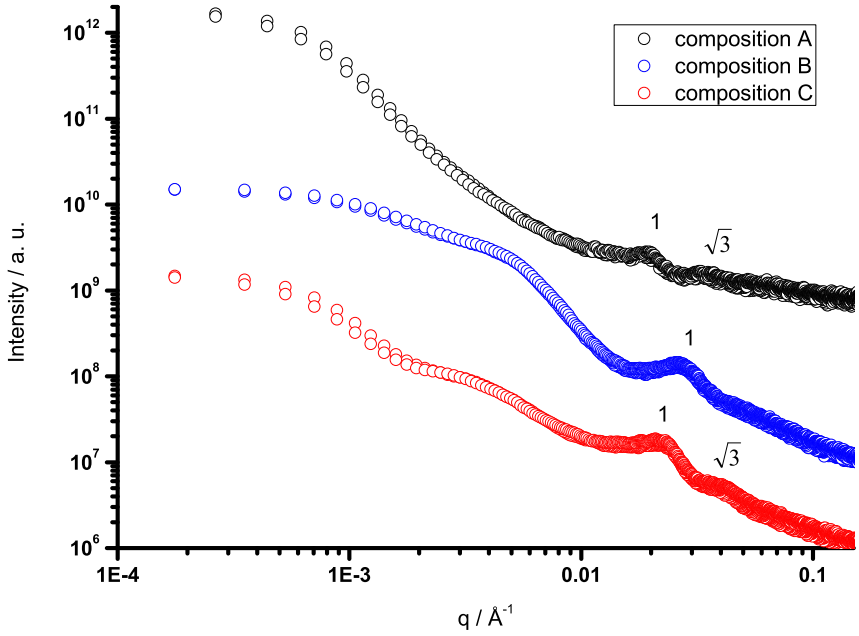

Figure 5.15: GISAXS out-of-plane cuts of the hybrid blocking layer with different compositions.

plane cuts of the blocking layers of composition A, B, and C. The broad peaks at low q-values in the GISAXS cuts arise from large domains that are also visible in the SEM images. Composition A and C show first and secondary order peaks with a ratio of 1:$\sqrt{3}$. This suggest a hexagonal ordering in these films. The primary peaks are positioned at q = 0.020 Å^{-1} for composition A and at q = 0.022 Å^{-1} for composition C, leading to a center-to-center distance of 31 and 29 nm, respectively. This length scale correlates to the distances found in the SEM images. As indicated by the intensity of the peaks, the ordering in film C is higher compared to film A. In the SEM image of the blocking layer of composition C a well-defined structure can be found as well. Thus, the increased amount of solvent improves the ordering in the films. However, the amount of acid does not influence the structure size. The primary peak of the blocking layer film B is shifted towards higher q-values compared to composition A and C. Higher q-values correspond to smaller, ordered structures. The position of the primary peak at q = 0.027 Å^{-1} leads to a center-to-center distance of 23 nm. Thus, by increasing the amount of TiO_2 precursor the

structure size in the film is reduced. This means, the variation of each component in the sol-gel mixture leads to a change in the structure of the hybrid films.

5.4.3 Crystallinity

For the preparation of the conventional blocking layer the sintering step is carried out at 450 °C for 2 hours in ambient atmosphere. This allows the amorphous titanium dioxide to completely crystallize in the anatase polymorph. Though the temperature and the calcination time are sufficient for TiO_2 to crystallize in a bulk material, the crystallization of TiO_2 within an organic matrix is not self-evident. Usually films of titanium dioxide, which are intended for the use in photovoltaics, are processed at 450-500 °C. Calcination at elevated temperatures may improve the crystallinity, on the other hand, the anatase phase may transform into the rutile phase in the temperature range of 600-700 °C. [155] For the application in solar cells the anatase form is the desirable material. [39] One reason is that the electron transport in rutile is slower compared to anatase. As a consequence, the same polymorph type is desired within the blocking layer. The effect of different calcination temperatures on the crystallinity and on the crystal structure of the hybrid nanocomposite is shown in Figure 5.16. The samples were prepared by drop casting the sol-gel mixture on a silicon wafer followed by a calcination step for 2 hours in nitrogen atmosphere. The reference sample without calcination shows a broad halo between 27° and 37° indicating amorphous material. The X-ray diffraction patterns for the samples calcined at 450 °C, 550 °C and 650 °C show the typical anatase peaks. Even at a temperature of 650 °C no rutile phase is formed. In contrast to the conventional blocking layer, a halo can still be found for these samples, which indicates a remaining fraction of amorphous titanium dioxide. In terms of crystal structure, no difference can be found within the temperature range between 450 °C and 650 °C. Thus, for the preparation of the blocking layer films a calcination temperature of 450 °C was chosen, because the conductivity of the TCO coating is reduced by exposure to elevated temperatures for long times. [78]

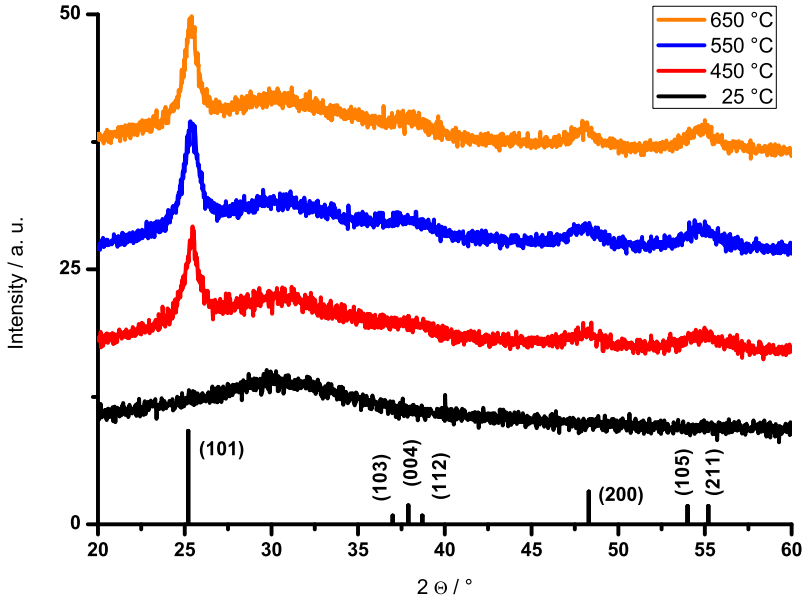

Figure 5.16: XRD patterns of the hybrid nanocomposite calcined at different temperatures with anatase reference peaks.

Areas of crystalline titanium dioxide can also be found in a TEM lamella of composition B that was calcined at 450 °C (Figure 5.17). The spacings in the FFT filtered image can be assigned to the (101) and (200) lattice planes of the anatase crystal structure. That means, even though the crystallization does not take place in a bulk material, in a hybrid composite a calcination temperature of 450 °C is sufficient for the amorphous titania to crystallize in the anatase polymorph. During the heating process the amorphous titania has turned crystalline, whereas the polymer ceramized around the anatase network. Based on the X-ray diffraction pattern for the sample calcined at 450 °C, the size of the titania crystals was estimated using the Scherrer equation. This way, a crystallite size of 37 nm is obtained. Thus, the crystallite size in the hybrid nanocomposite is larger compared to the bulk TiO_2 layer. This finding can be explained by the fact that the TiO_2 precursor used for the hybrid material is different to the one used for the compact TiO_2 film, and the titanium dioxide in the hybrid blocking layer is templated by a diblock copolymer.

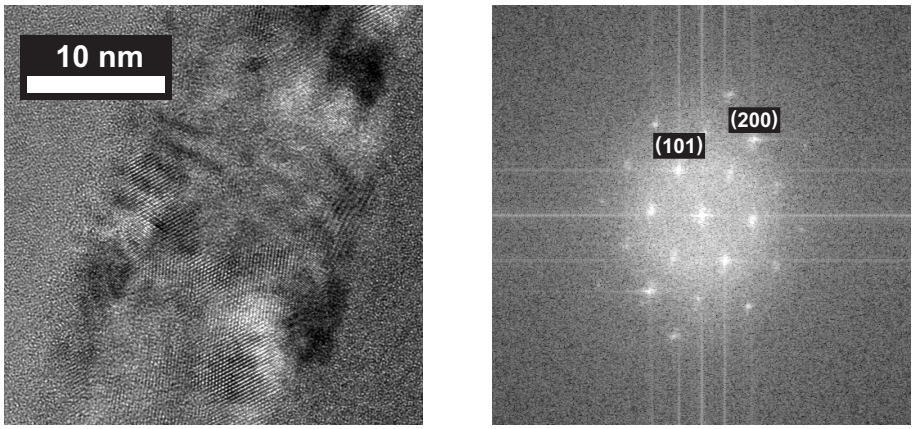

Figure 5.17: TEM image (left) and FFT-image (right) of a thin lamella of the hybrid blocking layer prepared with the focused ion beam.

5.4.4 Conductive SFM

The samples for conductive scanning force microscopy were measured on Pt-coated silicon substrates rather than on FTO glass in order to obtain samples with low roughness and homogeneous thickness. As the thickness of the blocking layers is different, one measures the conductance (I/U_{Sample}) and not the specific conductivity of the samples. Moreover, Berger et al. suggested that the locally measured current is not only determined by the resistance of the titania itself, but also by the contact resistance of the platinum/titania and the titania/tip interfaces. [156] However, as in these measurements the samples were prepared on identical substrates, the same type of tip was used, and in all cases TiO_2 is the conducting material, the results are reasonably comparable. In the current images the bright regions indicate areas of high current flow, whereas the dark regions designate areas of low current flow or insulation.

The conductive scanning force microscopy images of the hybrid blocking layers of composition A, B, and C are shown in Figure 5.18. The height images (Figure 5.18, A, C, and E) of the three blocking layer films show uniform and crack-free surfaces, respectively. The topography of the hybrid films of composition A and C exhibits a fine-grained structure, whereas the surface of the hybrid blocking layer B exhibits a more coarse-grained structure. The roughness of film B is higher (RMS roughness = 3 nm) compared to films A (RMS roughness = 0.6 nm) and C (RMS rough-

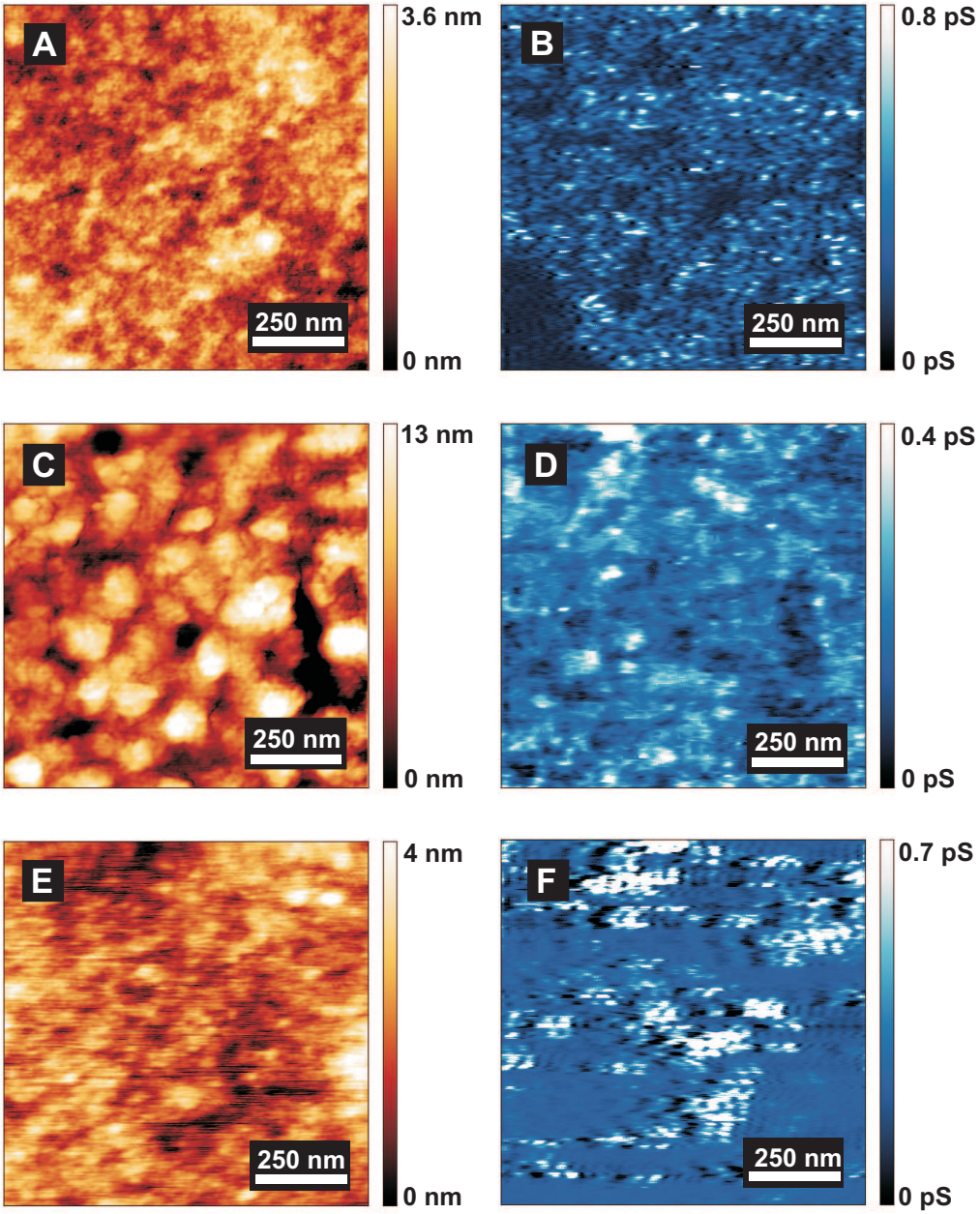

Figure 5.18: Height (left) and current (right) SFM images of the hybrid blocking layers of composition A (top), B (middle), and C (bottom) measured on a Pt-coated silicon wafer.

ness = 0.7 nm). The granular structures are attributed to agglomerates of TiO_2 particles. Since in composition B the amount of titanium dioxide is higher than in films A and C, the agglomerates are accordingly bigger.

In all cases, the current images (Figure 5.18, B, D, and F) of the hybrid blocking layers show a granular structure with circular spots of high current flow surrounded by insulating regions. Thus, the conductivity for all three samples is not homogeneous across the whole surface. Again, in the film of composition B the conducting spots are bigger compared to composition A and C owing to the higher amount of titanium dioxide. These measurements confirm the concept of a conducting TiO_2 network embedded in an insulating ceramic material. The current images of the hybrid films are similar to the one of the conventional blocking layer. However, in the case of the hybrid blocking layer, the areas of low current flow or insulation originate from the ceramic material that is incorporated into the film.

For composition B the average size of the small conducting spots is 30 nm. This size corresponds to the TiO_2 crystallite size obtained from line broadening in X-ray diffraction for the same composition. This correlation is an additional indication that the percolation pathways are actually provided by exposed particles of the crystalline TiO_2 network. Larger conductive areas in the current image are assigned to clusters of small crystallites.

The active area, as defined on page 50, is 9 % for composition A, 33 % for composition B, and 18 % for composition C of the hybrid blocking layer. As shown previously, the active area of the conventional blocking layer was 12 %. This means, although the nanocomposite consists to some extent of an insulating material, the active area of the hybrid film is higher.

5.4.5 Macroscopic Conductance

The macroscopic conductance of the conventional as well as of the hybrid blocking layers was investigated using samples of the structure FTO/blocking layer/Au. As all blocking layers showed to yield pinhole-free films, the current flow through the material can be measured by this sample architecture. The films were prepared on

FTO-coated glass, and a 100 nm layer of gold was deposited to serve as counter electrode. The current flow was measured in the range of -1 V to +1 V (Figure 5.19). The films have different thicknesses, and therefore the data shown in the diagram

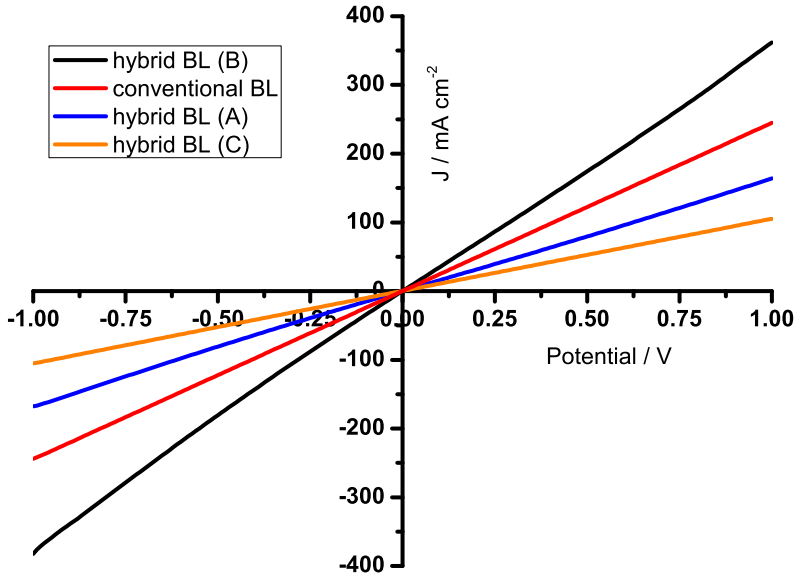

Figure 5.19: Current-voltage characteristics of the conventional and hybrid blocking layers of different compositions between two electrodes.

represent the conductance of the films rather than the material's specific conductivity. For all blocking layer materials a linear current density-voltage characteristic is observed. Thus, all types of layers show ohmic behavior. The difference in work function of FTO (ϕ = 4.3-4.4 eV) and titanium dioxide (ϕ = 4.2 eV) is very small, hence, no Schottky contact, which would result in a diode-like, rectifying current-voltage characteristic, is formed. [76, 157] The highest current flow is shown by the hybrid blocking layer of composition B followed by the classical blocking layer. The films of composition A and C both show a lower conductance than the conventional blocking layer. This finding correlates to the results of the conductive scanning force microscopy characterization. The highest active area was found for the hybrid film of composition B. For this composition the thickness of the film was reduced to $\sim$ 50 % of the conventional blocking layer. Thus, the improved conductance

of the hybrid blocking layer of composition B is attributed to the combination of lower film thickness and higher active area. Compared to the conventional blocking layer, the macroscpoic conductance is increased by 32 %. This higher macroscopic conductance should lead to a higher short-circuit current in a solar cell device.

5.4.6 Application in DSSCs

In order to compare the performance of the hybrid and the conventional blocking layer, dye-sensitized solar cells have been built. First, the application in liquid electrolyte based DSSCs is shown, followed by the implementation of the different blocking layers in solid-state DSSCs. The liquid electrolyte cells were built using a I^-/I_3^- redox couple in acetonitrile and in an ionic liquid, respectively. In the solid-state cells, the liquid electrolyte was replaced by the hole-conducting phase spiro-OMeTAD. Additionally to the solar cells employing the different types of blocking layers, reference samples without blocking layer have been assembled.

Dye-sensitized solar cells consist of several layers that are deposited onto the substrate one after another (see Chapter 4.3 for details). Each of these steps is critical for the performance of the final device. As a result, the efficiency of solar cells produced in different batches may vary. Therefore, the solar cells that are put in comparison in this thesis are prepared in one batch and under identical conditions to be reasonably comparable. Furthermore, the solid-state devices were measured at different positions (six electrodes, area = 0.140 cm^2), and the averaged values are shown here. The electrolyte based devices consisted of a single electrode with a typical area of $\sim$ 1.2 cm^2. Except for the blocking layer preparation, all samples have been treated exactly the same way in order to be comparable. This ensures that differences in the current-voltage characteristics can be exclusively related to the function of the blocking layer.

Application in Liquid Electrolyte Based DSSCs

In solid-state DSSCs the implementation of a blocking layer is well established. The role of a blocking layer for liquid electrolyte based solar cells is still under debate. [82,158] The energetics at the hole-conductor/TCO and the electrolyte/TCO interface are different in both types of cells. [78,159] However, several studies report that using a blocking layer in liquid electrolyte based devices is beneficial as well. [160–163]

In this chapter, the application of the hybrid and the conventional blocking layer in liquid electrolyte solar cells is investigated. JV curves of liquid electrolyte based solar cells with the different blocking layers and their characteristics are shown in Figure 5.20. Figure 5.21 shows the JV curves of ionic liquid based devices and their characteristic values. For a better overview, only the JV curves of the hybrid blocking layer with the composition that showed the highest efficiency are drawn. In the tables the devices are sorted descending from the highest efficiency. The Grätzel cells with the conventional and the hybrid blocking layers of composition B and C all exhibit a higher short-circuit current than the device without blocking layer. This is an indication for the reduced charge recombination owing to the function of the blocking layer. However, for these cells the open-circuit voltage and/or the fill factor is lower, respectively. From the slopes of the JV curves, the values for the series resistance R_S and the parallel shunt resistance R_P can be derived as described in Chapter 3.8. The parallel shunt resistance is similar for all devices. However, the series resistance for the device with the hybrid blocking layer of composition B is lower compared to the device with the conventional blocking layer. This lower series resistance is a result of the higher conductance of the hybrid film. With regard to the devices employing a hybrid blocking layer, the solar cell with the hybrid film of composition B, containing the highest amount of TiO_2, shows the highest efficiency. Nevertheless, the solar cell without blocking layer shows the highest efficiency among all devices.

The results for the ionic liquid type solar cells are similar. In some cases the characteristics of the devices employing a blocking layer are higher than the values of the

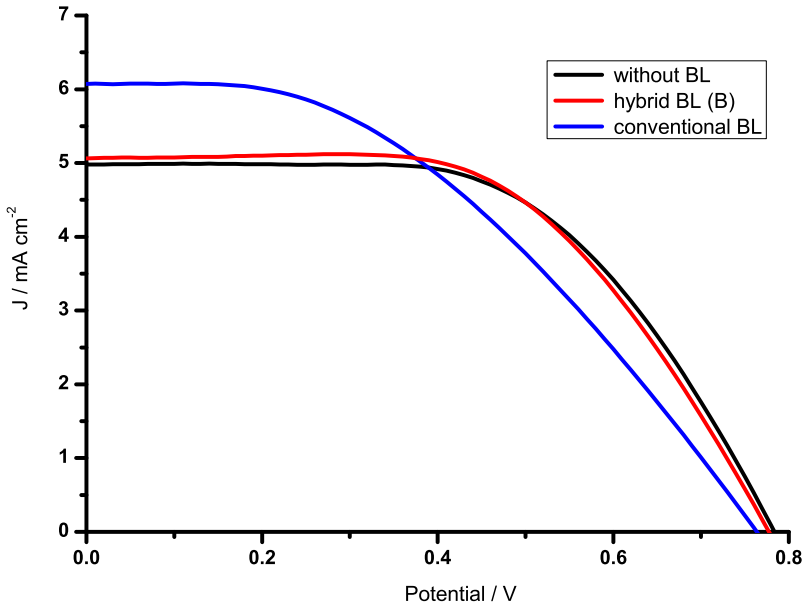

	η / %	J_{SC} / mA/cm^2	V_{OC} / V	FF / %
without BL	**2.24** ± 0.04	4.98 ± 0.02	0.78 ± 0.01	58 ± 1
hybrid BL (B)	**2.23** ± 0.04	5.06 ± 0.02	0.78 ± 0.01	57 ± 1
conventional BL	**1.96** ± 0.03	6.07 ± 0.03	0.76 ± 0.01	42 ± 1
hybrid BL (C)	**1.93** ± 0.03	5.13 ± 0.02	0.77 ± 0.01	49 ± 1
hybrid BL (A)	**1.40** ± 0.02	4.74 ± 0.02	0.77 ± 0.01	38 ± 1

Figure 5.20: JV curves and characteristics of Grätzel cells with the hybrid, the conventional, and without blocking layer.

device without blocking layer. In the end, the reference device without any blocking layer exhibits the highest overall efficiency. Again, composition B shows the highest efficiency among the devices with a hybrid blocking layer. In contrast to the Grätzel cells, this device does not exceed the efficiency of its counterpart employing the conventional blocking layer. Thus, the functionality of the blocking layer seems to be also dependent on the cell architecture, e.g. whether a liquid electrolyte or an ionic liquid is used.

The implementation of the different blocking layer in liquid electrolyte based solar cells leads to the assumption that the recombination of charge carriers is negligible for these types of devices. To investigate the extent of recombination at the elec-

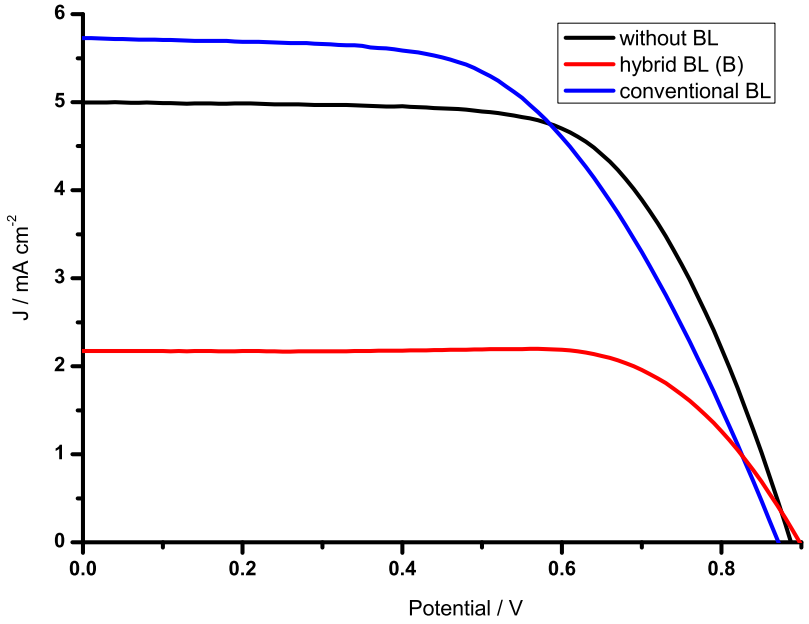

	η / %	J_{SC} / mA/cm^2	V_{OC} / V	FF / %
without BL	**2.85** ± 0.05	5.00 ± 0.02	0.89 ± 0.01	65 ± 1
conventional BL	**2.77** ± 0.05	5.73 ± 0.03	0.87 ± 0.01	56 ± 1
hybrid BL (B)	**1.38** ± 0.02	2.17 ± 0.01	0.90 ± 0.01	71 ± 1
hybrid BL (C)	**1.32** ± 0.02	4.05 ± 0.02	0.88 ± 0.01	37 ± 0
hybrid BL (A)	**0.89** ± 0.02	3.35 ± 0.02	0.89 ± 0.01	30 ± 0

Figure 5.21: JV curves and characteristics of ionic liquid based solar cells with the hybrid, the conventional, and without blocking layer.

trolyte/TCO interface compared to the solid-state hole-conductor/TCO interface, two representative devices have been assembled. A symmetrical device with the structure FTO/electrolyte/FTO and another device with the structure FTO/spiro-OMeTAD/Au represent the interfaces where the charge recombination takes place in Grätzel cells and in solid-state DSSCs, respectively. These devices are similar to solar cells omitting the dye-sensitized, active TiO_2 layer. As a result, the electrolyte and the hole-conducting material are in direct contact with the TCO front electrode. The JV curves of these devices are shown in Figure 5.22. The device with the liquid electrolyte shows a significantly lower current density throughout the measured potential range compared to the device with the solid hole-conducting

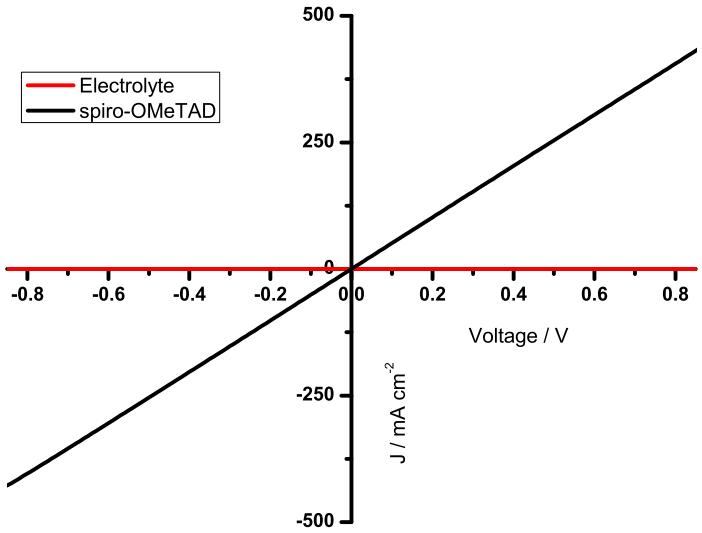

Figure 5.22: JV curves of representative samples with the structure FTO/electrolyte/FTO and FTO/spiro-OMeTAD/Au.

material. The difference in current density between both devices is 5 orders of magnitude. Similar results have been found by other groups using impedance spectroscopy measurements. [164] This demonstrates that the charge transport from the FTO electrode to the hole-conducting material is much higher than the charge transport from the FTO to the liquid electrolyte. As a consequence the prevention of charge recombination is of much higher importance in solid-state solar cells than in liquid electrolyte based devices. [165–167] This explains why the implementation of a blocking layer did not improve the efficiency in the liquid electrolyte based solar cells. The opposite effect is observed as the implementation of a blocking layer reduced the performance of the solar cells owing to the serial resistance of the layer. The reduced charge recombination in electrolyte based devices is caused by the charge transfer resistance and the associated overpotential between the liquid electrolyte and the solid electrode. [58] The charge transport resistance is the electrical resistance of charges between different phases. Ideally, an electron can pass a semiconductor/electrode interface without resistance like in a solid-state DSSC. At the liquid/electrode interface the conditions are different. In this case a barrier exists

for the solvated electron to migrate from the liquid phase to the solid phase. This causes an overpotential at the liquid/solid interface. The platinum-coating of the back electrode in electrolyte based DSSC serves as a catalyst and lowers this energy barrier. Still, this overpotential suppresses the recombination of charges at the electrolyte/electrode interface.

In summary, the implementation of a blocking layer in the liquid electrolyte based solar cells did not improve the efficiency. For this reason, in the following work solid-state dye-sensitized solar cells that employ spiro-OMeTAD as hole-conducting phase will be used to investigate the functionality of the hybrid blocking layer.

Application in Solid-State DSSCs

Solid-state hole-transporting materials are used as a replacement for liquid electrolytes to avoid evaporation and leakage. One of the most widely used hole-conducting materials for solid-state DSSCs is spiro-OMeTAD. Figure 5.23 shows a SEM cross section image and optical photograph of a solid-state DSSC employing spiro-OMeTAD. To avoid overlapping of the different layers after the fracture of the

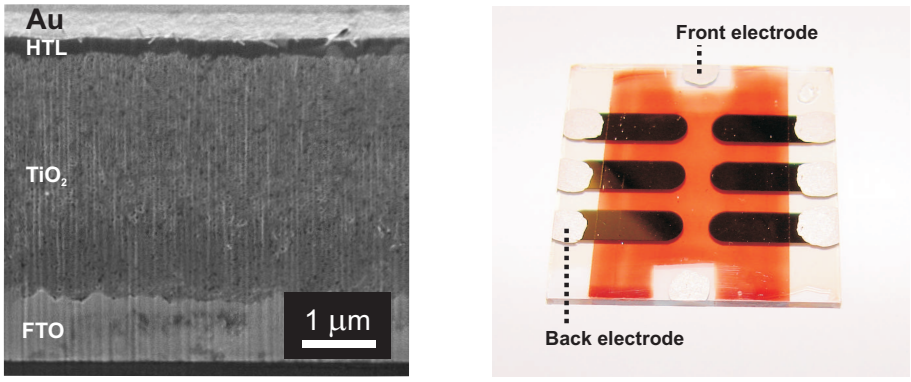

Figure 5.23: SEM image of a cross section (left) and optical photograph (right) of a solid-state dye-sensitized solar cell.

device, the surface of the SEM sample was polished using the focused ion beam. The vertical lines that loom in the cross cut originate from the preparation with the FIB. Doctor blading of the TiO_2 paste resulted in a transparent film with a thickness of ~ 3 μm as determined by profilometry. After the dye-uptake the titanium dioxide

films were colored reddish. Six silver/gold back electrodes are evaporated trough a shadow mask on top of the device. During the solar cell assembly two FTO-contacts were kept free to serve as front electrodes.

Solid-state DSSCs employing the hybrid and the conventional blocking layer as well as solar cells without blocking layer have been prepared. The JV curves of these devices and their characteristics are shown in Figure 5.24. For clarity, only the JV curve of the hybrid blocking layer which showed the highest efficiency is shown. In

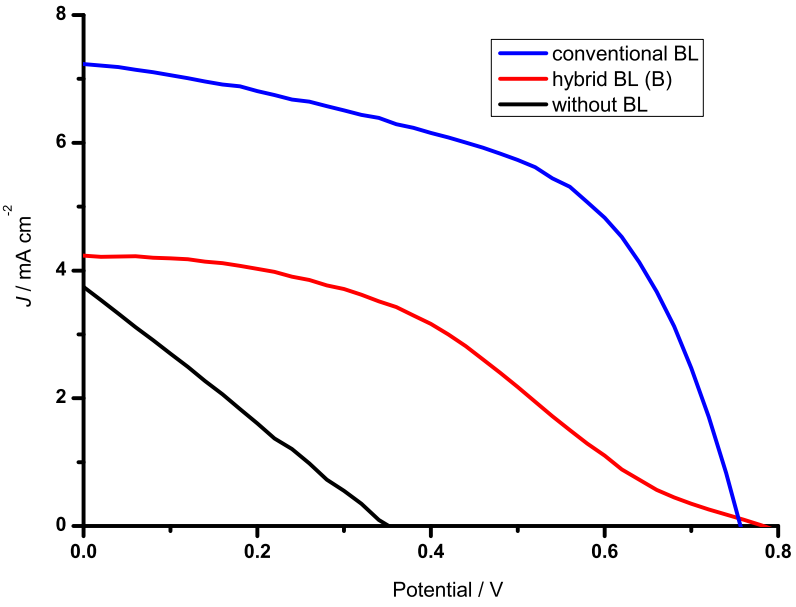

	η / %	J_{SC} / mA/cm^2	V_{OC} / V	FF / %
conventional BL	**2.98** ± 0.05	7.05 ± 0.03	0.76 ± 0.01	55 ± 1
hybrid BL (B)	**1.27** ± 0.02	4.23 ± 0.02	0.78 ± 0.01	38 ± 1
without BL	**0.35** ± 0.01	3.75 ± 0.02	0.35 ± 0.00	26 ± 0
hybrid BL (A)	**0.33** ± 0.01	1.61 ± 0.01	0.70 ± 0.01	29 ± 0
hybrid BL (C)	**0.08** ± 0.00	0.84 ± 0.00	0.39 ± 0.01	25 ± 0

Figure 5.24: JV curves and characteristics of solid-state solar cells with the hybrid, the conventional, and without blocking layer.

contrast to the electrolyte based devices, the solid-state solar cells employing the hybrid blocking layer B and the conventional blocking layer both exhibit a significant increased short-circuit current, open-circuit voltage, fill factor, and a higher

overall efficiency compared to the device without blocking layer. Again, this shows the benefits of the implementation of a blocking layer in solid-state DSSCs. The open-circuit voltage of both devices is similar to the difference in work function of FTO ($\phi = 4.3$ eV) and gold ($\phi = 5.1$ eV). The hybrid blocking layer of composition B shows the best functionality among the hybrid films. However, for this device an increased series resistance R_S is found. The JV curve is slightly S-shaped, which can be caused by interfacial effects such as charge trapping. [168] Nevertheless, for this solar cell all characteristic values are much higher compared to the cell without blocking layer. The thickness of the conventional blocking layer is in the order of $\sim$ 100 nm, and the thickness of the hybrid films is even lower. Thus, the titanium dioxide within the blocking layers does not contribute noticeably to the generation of charge carriers compared to the 3 μm thick active titania layer. Therefore, one can assume that in all cells the same amount of electrons and holes is generated under illumination. The increased short-circuit current in the cell employing the hybrid blocking layer is a direct hint that less charges recombine, and more charge carriers can be gathered at the electrodes. Thus, the implementation of the hybrid blocking layer effectively avoids the current loss at the FTO/hole-transport layer interface. This results in an overall efficiency of 1.27 %, which is a significant improvement compared to the cell without blocking layer. However, the device with the classical, compact TiO_2 layer exhibits a higher short circuit current of 7.05 mA/cm^2 and an overall efficiency of 2.98 %. The reference device without blocking layer shows a very poor performance with a short-circuit current of 3.75 mA/cm^2 and an overall efficiency of 0.35 %. Its linear current-voltage behavior results from the lack of a rectifying blocking layer, and this leads to low values in short-circuit current, open-circuit voltage, fill factor, and overall efficiency. The situation is similar for the devices employing the hybrid blocking layer of composition A and C.

In all examples presented, the hybrid blocking layer of composition B showed to yield the best results among the different compositions of the sol-gel mixture. The hybrid film of composition B contains the highest amount of titanium dioxide, exhibits the highest active area, the highest conductance, and the highest efficiency in solar cells. These properties are attributed to the increased amount of titanium

dioxide. By the increased amount of titanium dioxide the TiO_2 network is more dense, thereby improving the charge transport and the accessibility of the conducting network at the surface of the film. The hybrid blocking layer of composition B reaches approximately half the thickness of the conventional blocking layer. This leads to the improved electrical conductance compared to the conventional blocking layer. However, the efficiency of the solar cell using the conventional blocking layer was not reached. The S-shaped JV curve as well as the increased series resistance R_S of the device employing the hybrid blocking layer indicate that the charge transport at the interface between the hybrid film and the active titanium dioxide needs to be optimized.

In this chapter, an argon plasma was used to expose the TiO_2 network at the surface of the blocking layer. During the plasma treatment the surface may heat up due to friction forces. This could influence the surface properties and the charge transport at the boundary between the blocking layer and the mesoporous TiO_2 layer. For this reason, in the following chapter another approach is used for the preparation of the hybrid blocking layer films.

5.5 Solvent Annealing of the Hybrid BL

Solvent vapor annealing (VA) proved to be useful to enhance the morphology of solution-cast block copolymer films, and even change the orientation of the microdomains completely. [169–173] The hybrid films produced in this work are prepared by spin coating at high speed and high acceleration (speed = 2000 rpm, acceleration = 2000 rpm/s). That means, the morphology of the diblock copolymer and the embedded TiO_2 network is created under high stress, and the thermodynamic ideal structure may not be formed, but metastable structures may arise instead. This may be disadvantageous concerning the electrical conductivity of the films, as the electrical properties are dependent on the morphology. [128] Therefore, solvent vapor annealing is used to improve the structure of the hybrid blocking layer films as shown in Figure 5.25. Exposure of the spin coated films to a saturated solvent atmosphere swells the films and increases the mobility of the polymer chains. This

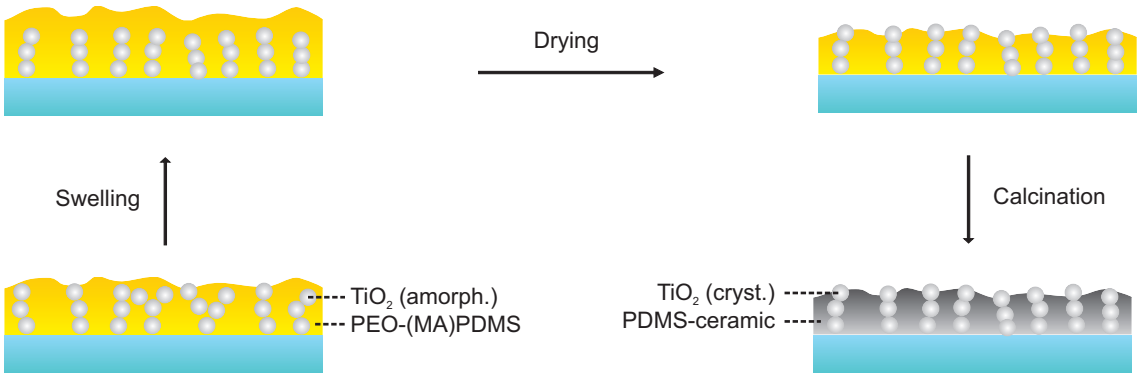

Figure 5.25: Schematic representation of the solvent annealing step in the preparation of the hybrid blocking layer.

allows the structure of the hybrid films to change. For this purpose, THF was used as a suitable solvent, since it is a good solvent for the PEO block as well as for the PDMS block. After the spin coating process, the films were exposed to a saturated THF atmosphere for 90 minutes. Owing to its high vapor pressure, the films can get completely soaked by the solvent in the given time. Subsequently, the films were dried in ambient atmosphere and calcined, whereas the titanium dioxide crystallizes and the polymer ceramizes.

The sol-gel-mixture of composition B yielded the best results among the hybrid films when plasma etching was used in the preparation of the blocking layer. The blocking layer prepared by solvent annealing showed the highest efficiencies in solar cells for the same composition (see page 82). Therefore, this chapter focuses on the sol-gel composition B containing 1 % diblock copolymer, 10 % TiO_2 precursor and 1 % HCl. Additionally, in this chapter Polymer2 with a PEO to PDMS ratio of $\sim$ 1:1 is used as templating agent, exclusively.

5.5.1 Film Thickness

A cross section SEM image and the X-ray reflectivity curve of the hybrid blocking layer of composition B after the solvent annealing treatment are shown in Figure 5.26. The film exhibits a more porous structure compared to the blocking layer films prepared with the plasma etching treatment, still it covers the surface of the FTO

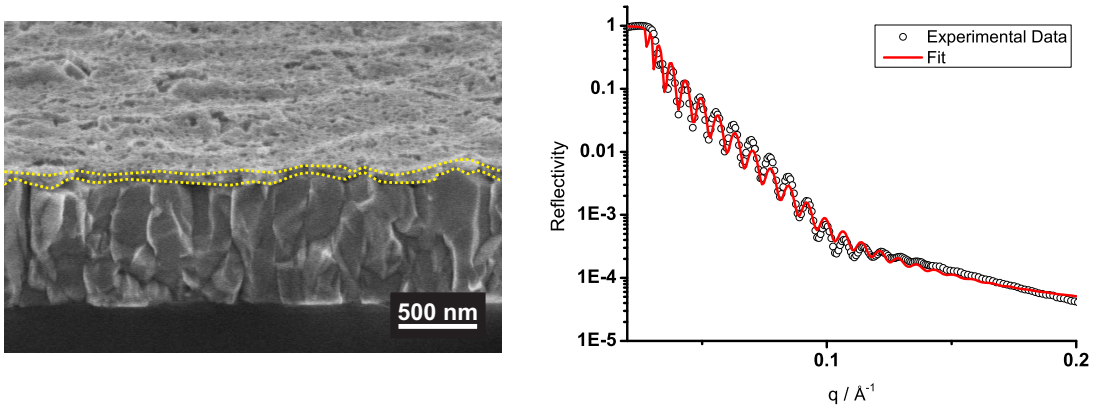

Figure 5.26: SEM cross section image (left) and XRR curve (right) of the hybrid blocking layer prepared by solvent annealing.

completely to serve as a barrier separating the hole-transport material from the FTO electrode. The application in solar cells in Chapter 5.5.6 confirms that the hybrid blocking layer is not penetrated by spiro-OMeTAD, as the charge recombination is reduced tremendously compared to the device omitting the blocking layer. The argon plasma has a grinding effect on the surface of the material, thus, these films are smoother compared to the blocking layer prepared by solvent vapor annealing. The peak-to-valley values determined from the SEM images range from 30 to 90 nm. Nominal X-ray reflectivity measurements resulted in a thickness of 78 nm. This value is slightly higher compared to the film of the same composition prepared with the plasma treatment. As shown in Chapter 5.4.1, the plasma removes the uppermost layer of the hybrid film. Still, compared to the conventional blocking layer, the thickness of the hybrid film prepared by vapor annealing is reduced by 36 %.

A thin lamella of the blocking layer was prepared using the focused ion beam. Electron spectroscopy imaging was used to map the titanium (dioxide) amount throughout the film. The ESI/TEM images are shown in Figure 5.27. The bright, sphere-like domains in the TEM image indicate areas of high electron density. These domains correspond to agglomerates of titanium dioxide. The domains are surrounded by ceramic material that exhibits a lower electron density as indicated by the dark

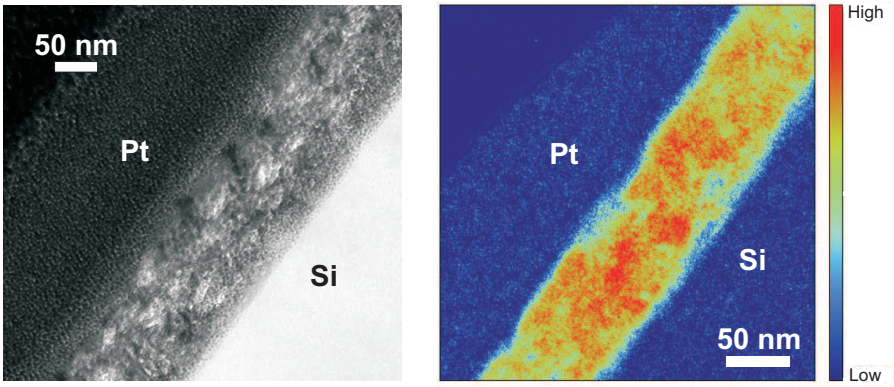

Figure 5.27: Focused ion beam prepared lamella of the hybrid blocking layer: TEM image (left) and titanium (dioxide) mapping by ESI (right).

regions. The titanium mapping by ESI confirms the homogeneous spreading of the titanium dioxide throughout the layer. The TiO_2 domains are not isolated from each other, and traces of titanium dioxide can be found throughout the film. In Chapter 5.4, Polymer1 with a PEO to PDMS ratio of 1:2 was used in the preparation of the hybrid films, and in these films most of the titanium dioxide was located at the bottom of the layer. Now Polymer2 with a PEO to PDMS ratio of 1:1 is used to template the hybrid films. Thus, the exchange of the templating polymer improves the intermixture of the titanium dioxide and the ceramic material in the films. This homogeneous distribution of the titanium dioxide from the top to the bottom of the layer is beneficial for the electron transport.

5.5.2 Film Structure

The morphology of the hybrid films becomes not clear by using microscopic techniques only. Thus, the hybrid blocking layer was investigated by GISAXS to get an insight to the morphology of the film, and to correlate the morphology to the surface structure found using microscopy techniques. Figure 5.28 shows the GISAXS out-of-plane cut and a top-down view SEM image of the hybrid blocking layer of composition B prepared by vapor annealing. The out-of-plane cut of the GISAXS measurement was fitted according to the Unified Fit Model. [174] This model divides

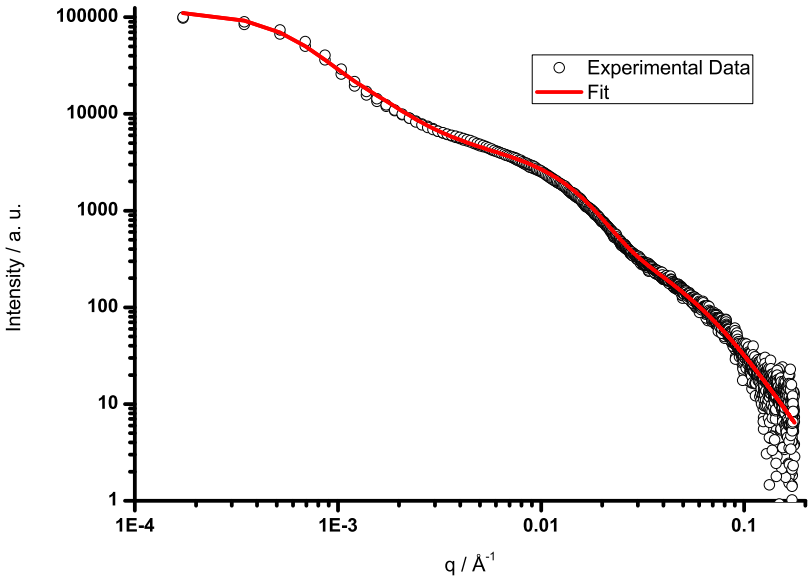

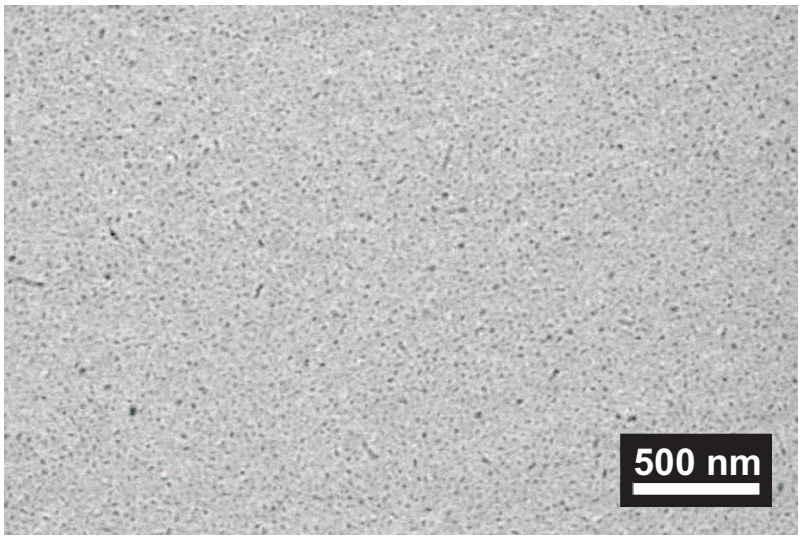

Figure 5.28: GISAXS out-of-plane cut and SEM top-down-view image of the hybrid blocking layer of composition B prepared by vapor annealing.

the GISAXS cut into linear Porod and shoulder-like Guinier regimes and describes the morphology of the material using several structural levels ranging from single particles to agglomerates. This way, values for the radius of gyration (R_g) and the fractal dimension (P) are obtained. The fractal dimension P gives information on the spacial arrangement of the scattering centers.

No distinct primary peak can be observed in the out-of-plane cut. Compared to the blocking layer films prepared with Polymer1, the data shows a low-order structure. Furthermore, the fit shows that small TiO_2 particles with a radius of gyration of $R_g = 13$ nm are dispersed in the hybrid material. Structures of similar size can also be found in the top-down view SEM image. The fractal dimension of P = 2.5 indicates a 3-dimensional arranged structure of particles and gives an additional hint to the presence of a percolating TiO_2 network within the blocking layer.

5.5.3 Crystallinity

The XRD pattern of a drop casted nanocomposite sample that was calcined for 2 hours at 450 °C is shown in Figure 5.29. In terms of crystallinity and crystal structure, the XRD pattern looks similar to the results obtained for the nanocomposite

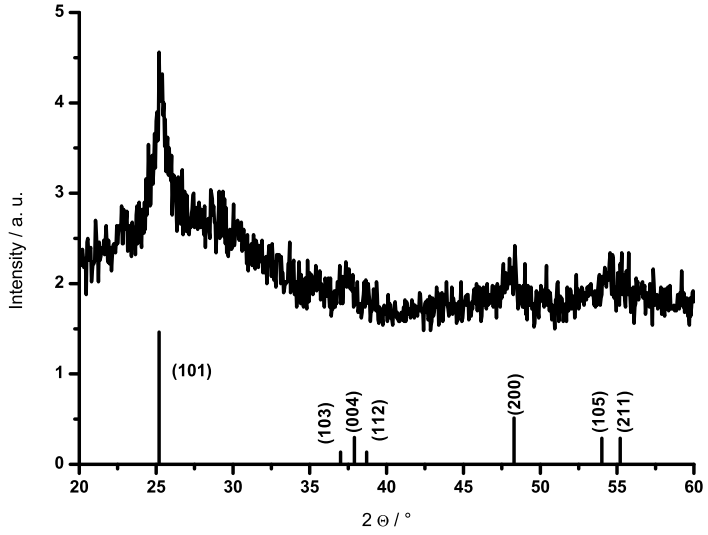

Figure 5.29: XRD pattern of the hybrid nanocomposite with anatase reference peaks.

using Polymer1 (see page 60). A single, crystalline phase in the anatase polymorph is visible. A halo that indicates a fraction of amorphous titania within the ceramic material is visible as well. The crystallite size estimated by line broadening is 10 nm. This result is in good agreement with the radius of gyration of R_g = 13 nm found in the GISAXS measurement. The value is lower compared to the hybrid blocking layer film prepared with Polymer1 (37 nm) and similar to the crystallite size found in the compact TiO_2 layer (12 nm). Thus, by employing Polymer2 as templating agent, the crystallinity and the crystal structure remains unaffected, but the size of the titania crystallites is reduced.

5.5.4 Conductive SFM

The conductive scanning force microscopy images of the untreated as well as of the annealed hybrid blocking layer are shown in Figure 5.30. Both height images show

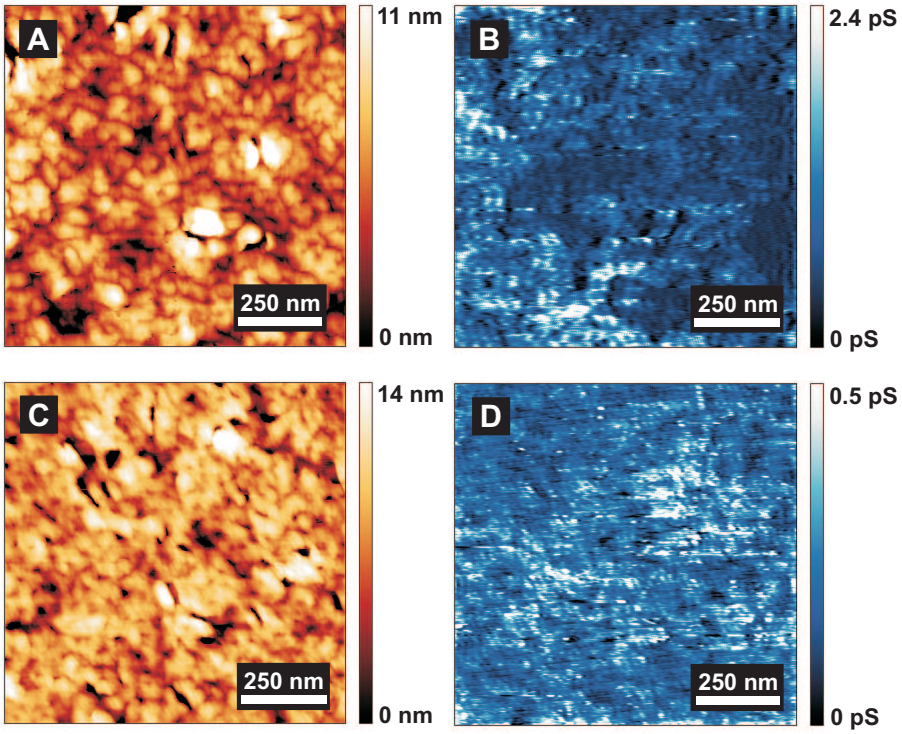

Figure 5.30: Height (left) and current (right) SFM images of the hybrid blocking layer without (top, applied voltage 4.5 V) and with (bottom, applied voltage 3.5 V) the vapor annealing treatment.

granular structures for the untreated (Figure 5.30, A) (RMS roughness = 2.4 nm) and for the annealed (Figure 5.30, C) (RMS roughness = 2.6 nm) film. Similar to the measurements in Chapter 5.4.4, the conductivity is not homogeneous across the sample surface. Both samples (Figure 5.30, B and D) show circular spots of high conductivity surrounded by insulating regions. However, compared to the equivalent hybrid film prepared by plasma etching, the size of the bright spots is smaller. A statistical analysis leads to an average size of 10 nm for the small conducting spots. As shown by the GISAXS and XRD measurements, the titania crystallites are of the same size. The active area is 14 % for the untreated and 27 % for the vapor annealed film. Thus, by the solvent vapor annealing the microscopic conductivity of the films is improved. Though the active area of the vapor annealed sample is lower compared to the blocking layer prepared by plasma treatment (33 %), it is still higher than the one of the conventional TiO_2 film (12 %).

5.5.5 Macroscopic Conductance

Samples of the structure FTO/blocking layer/Au were assembled to investigate the macroscopic conductance of the different materials. The current-voltage characteristics are shown in Figure 5.31. All samples show linear current-voltage characteristics, hence, an ohmic contact is formed. The conductance of the annealed blocking layer is slightly higher compared to the untreated sample. This finding is in agreement with the results from the conductive scanning force microscopy measurements, which showed that the active area is higher for the blocking layer with the vapor annealing treatment. Both hybrid films show a higher current flow than the compact TiO_2 layer. The conductance of the reference sample, i.e. the conventional blocking layer, is similar to the results on page 63.

The annealed, hybrid film exhibits about twice the conductance of the conventional blocking layer. The difference was 32 % when Polymer1 was used for the preparation of the hybrid blocking layer. This enhancement is attributed to the improved distribution of the titania particles within the ceramic matrix as shown by the investigation of the TEM lamella.

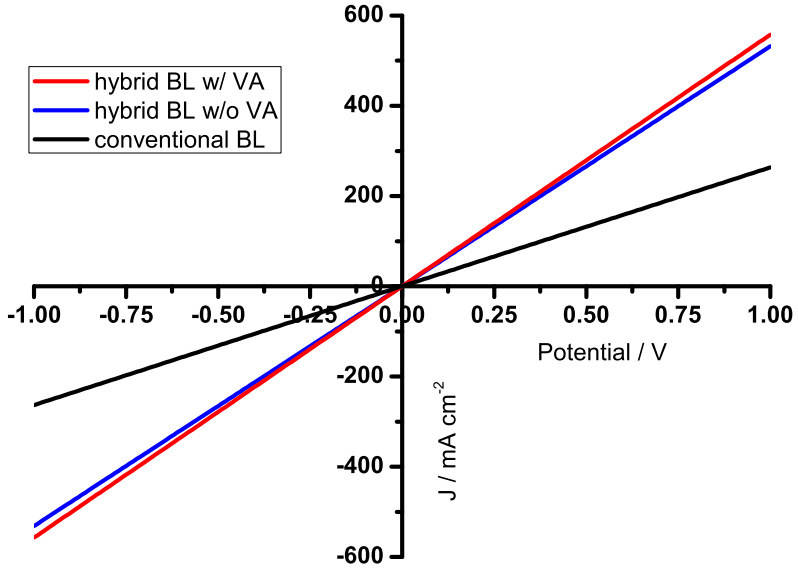

Figure 5.31: Current-voltage characteristics of the conventional and hybrid blocking layers (untreated and vapor annealed) between two electrodes.

5.5.6 Application in DSSCs

Comparison of Different Compositions

As a preliminary test, the three hybrid blocking layer films of composition A, B, and C were prepared with the vapor annealing treatment, and these films were implemented in solid-state DSSCs. The JV curves and the characteristics of these devices are shown in Figure 5.32. The solar cell with the hybrid blocking layer B exhibits a short-circuit current of 4.23 mA/cm^2, an open-circuit voltage of 0.69 V, and a fill factor of 35 %. These values lead to an overall efficiency of 1.07 %. The characteristic values for the hybrid films of composition A and C are significantly lower. The power conversion efficiencies for the devices employing the films A and C are 0.12 % and 0.03 %, respectively. Thus, the hybrid blocking layer of composition B performs best. The same result is found in Chapter 5.4, where the different compositions of the hybrid blocking layer prepared by plasma etching were characterized thoroughly.

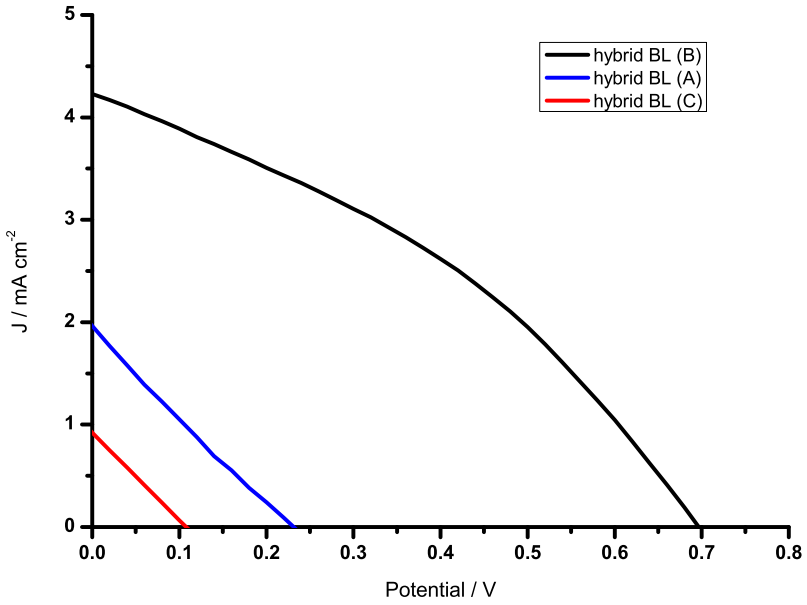

	η / %	J_{SC} / mA/cm^2	V_{OC} / V	FF / %
hybrid BL (B)	**1.07** ± 0.02	4.23 ± 0.02	0.69 ± 0.01	35 ± 0
hybrid BL (A)	**0.12** ± 0.00	1.97 ± 0.01	0.25 ± 0.00	23 ± 0
hybrid BL (C)	**0.03** ± 0.00	0.92 ± 0.00	0.11 ± 0.00	26 ± 0

Figure 5.32: JV curves and characteristics of solid-state DSSCs with hybrid blocking layers of different compositions

Effect of Vapor Annealing

To investigate the effect of the vapor annealing treatment on the hybrid blocking layer of composition B, two hybrid blocking layers of this composition were implemented in solar cells. One blocking layer was annealed for 90 minutes in a THF atmosphere, the other one was calcined right after the spin coating of the sol-gel mixture. Additionally, a device with the conventional, compact TiO_2 film and a solar cell without blocking layer served as a reference. The JV curves and their characteristics are shown in Figure 5.33. Both solar cells employing the hybrid films show a higher efficiency than the device with the conventional blocking layer and the device without blocking layer. The efficiencies are 2.71 % and 2.61 % for the device with and without vapor annealing treatment, respectively. For the sample

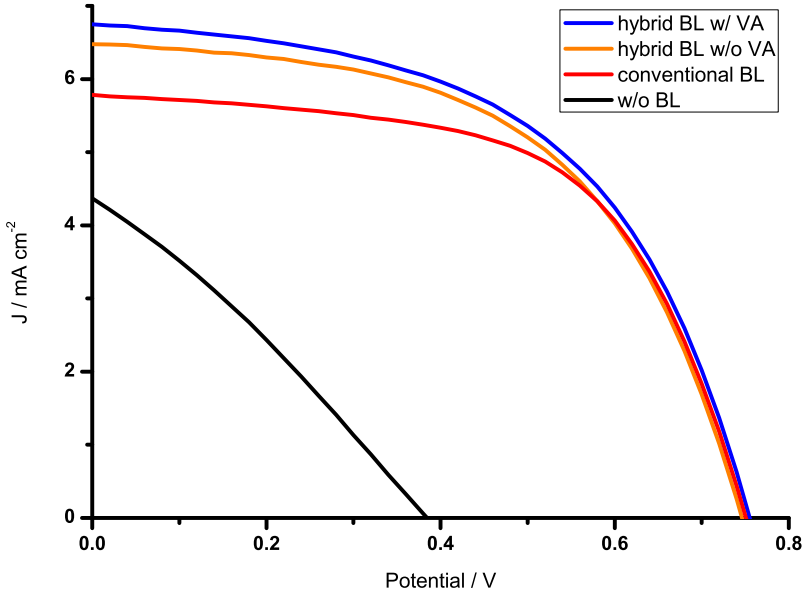

	η / %	J_{SC} / mA/cm^2	V_{OC} / V	FF / %
hybrid BL w/ VA	**2.71** ± 0.05	6.75 ± 0.03	0.76 ± 0.01	53 ± 1
hybrid BL w/o VA	**2.61** ± 0.05	6.47 ± 0.03	0.75 ± 0.01	54 ± 1
conventional BL	**2.56** ± 0.05	5.78 ± 0.03	0.75 ± 0.01	59 ± 1
w/o BL	**0.50** ± 0.01	4.37 ± 0.02	0.39 ± 0.01	29 ± 0

Figure 5.33: JV curves and characteristics of solid-state DSSCs with hybrid, the conventional, and without blocking layer.

with the conventional, compact TiO_2 film a power conversion efficieny of 2.56 % is found. Thus, an enhancement of 6 % between the annealed, hybrid film and the conventional blocking layer is achieved. The short-circuit currents for the devices with the vapor annealed, the untreated and the compact blocking layer are 6.75 mA/cm^2, 6.47 mA/cm^2, and 5.78 mA/cm^2, respectively. The open-circuit voltages and the fill factors for these devices are similar as well as the values for the parallel shunt resistance R_P and the series resistance R_S. Therefore, the difference in the efficiencies is essentially attributed to the difference in short-circuit current and directly related to the prevention of charge recombination. The reference device without a blocking layer shows very low characteristic values and is poorly functional. The absence of a rectifying blocking layer leads to the observed linear current-voltage characteristics.

In Chapter 5.4, the hybrid blocking layer, prepared by the plasma etching treatment, showed to prevent charge recombination. However, the efficiency of the device with the conventional blocking layer was not exceeded. At the same time, an increased series resistance R_S and a S-shaped JV curve was observed. These results indicated the presence of charge traps owing to interfacial effects, which may be caused by the plasma etching treatment. Now, a vapor annealing treatment is used in the preparation of the hybrid blocking layer. Solar cells with this type of hybrid films show a diode-like JV curve, and the efficiency of the device with the conventional blocking layer is exceeded. The improved efficiency is attributed to the replacement of the plasma etching step and to the exchange of the templating diblock copolymer. Additionally, the vapor annealing treatment shows a beneficial effect on the performance of the solar cells.

Long-Term Stability

Compared to inorganic photovoltaics the aging/stability of organic solar cells is a critical issue. [175,176] While silicon based solar cells proved to be stable in outdoor applications on a long-time scale, the organic devices show a faster degradation. Environmental parameters such as oxygen, water, and heat strongly influence the performance of organic devices. Often, a loss in performance is observed, which is caused by the degradation of the organic materials. Furthermore, the exposure to ambient atmosphere can also influence the electrode materials as well as the titanium dioxide.

The solar cells presented in this work so far have been characterized right after the cell assembly. To investigate the evolution of the cell characteristics and their long-term stability, solar cells with different blocking layers have been prepared. The devices were testet, stored in ambient atmosphere, and retested after several days. The evolution of the characteristic values of solar cells employing the vapor annealed, hybrid blocking layer and the compact TiO_2 blocking layer is shown in Figure 5.34. Each measurement is marked by a solid point and the dotted lines are a guide to the eye. Right after the cell assembly both devices show the highest

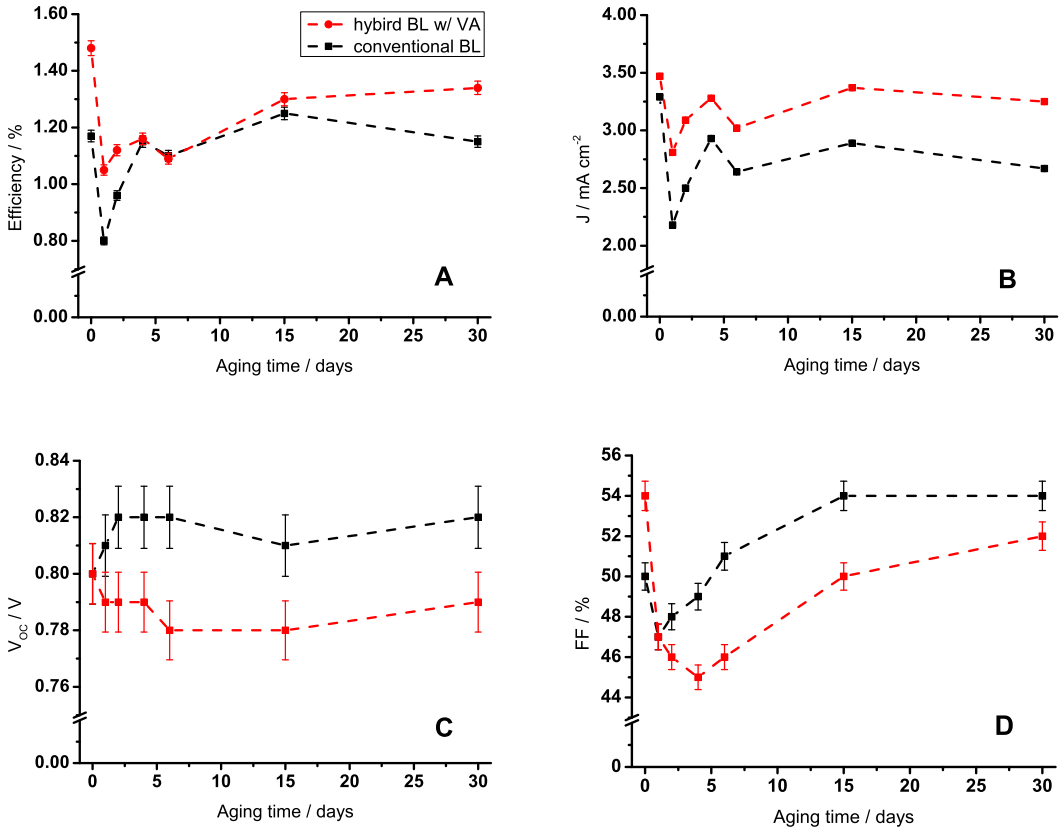

Figure 5.34: Evolution of the efficiency (A), the J_{SC} (B), the V_{OC}, and the fill factor (D) of DSSCs employing the hybrid and the classical blocking layer.

efficiency of the aging study (Figure 5.34, A). In the beginning, the efficiency of the solar cell with the hybrid and the conventional blocking layer is 1.48 % and 1.17 %, respectively. By replacing the compact TiO_2 film with the hybrid blocking layer, the efficiency is increased by 27 %, thus, even more than in the previous measurement (Figure 5.33). The efficiencies of both devices drop remarkably after the first day of storage, then slowly recover towards the last measurement after 30 days. However, the inital efficiency is not reached after that period of time. The increased efficiency of the solar cell employing the hybrid blocking layer over the device employing the conventional blocking layer is preserved within the 30 days.

A similar trend is observed for the short-circuit current (Figure 5.34, B). The short-circuit current drops after the first day and recovers towards the last measurement.

Unlike the efficiency and the short-circuit current, the open-circuit voltage and the fill factor (Figure 5.34, C and D) are higher for the device with the conventional blocking layer. However, the variation of the open-circuit voltage and the fill factor is negligible small. Thus, the increased efficiency of the solar cell with the hybrid blocking layer is mainly attributed to the increased short-circuit current as a result of suppressed charge recombination.

It is well-known that the efficiency of organic solar cells decreases upon exposure to ambient atmosphere. However, it is surprising that after the initial drop of the characteristic values after the first day of storage, the values recover for the subsequent measurements. To explain this finding, one has to take several effects into account.

Oxygen that is adsorbed on the surface of the titanium dioxide can scavenge electrons to generate O_2^-. These electron traps decrease the conductivity of the TiO_2 film, thereby reducing the short-circuit current as well as the overall efficiency. [177] On the contrary, it has been shown that water adsorbs dissociatively on the anatase surface, leading to an enhanced conductivity of the layer. Due to the high porosity of the titanium dioxide layer, these converse effects have a strong influence on the functionality of the device.

Right after the cell assembly the amount of oxygen and water in the devices is minimal. As the solar cell is not sealed, water and oxygen diffuse into the different materials in ambient atmosphere. This effect is the strongest after the first day of storage and explains the initial drop of the characteristics of the devices. Afterwards, the amount of oxygen and water in the device is in an equilibrium state with the ambient air. Additionally, the temperature has an influence on the functionality of the devices. The combination of several beneficial and detrimental effects then determines the performance of the photovoltaic devices.

To elucidate the evolution of the device performance in detail, further studies with encapsulated devices would be required. However, these measurements show that the hybrid blocking layer prepared by vapor annealing yields an increased efficiency that is preserved even on a long-time scale.

6 Summary and Outlook

It was shown that the implementation of a hybrid blocking layer in DSSCs is feasible and represents a promising alternative to the conventional, inorganic approach.
The investigation of the conventional blocking layer revealed that, even though the layer exhibits a high degree of crystallinity and is optimized in terms of thickness, only a part of the film serves for charge transport, actually. The area of low conductivity, originating from residuals of the organic TiO_2 precursor, represents a drawback of the classical blocking layer that is widely used in organic solar cells.
For the fabrication of the hybrid blocking layer, two batches of the novel diblock copolymer PEO-MA(PDMS) (labeled Polymer1 and Polymer2) were synthesized to serve as templating agents. Using sol-gel chemistry, homogeneous, crack-free layers of reduced thickness down to 24 nm were obtained.
At first, a plasma etching step was used in the preparation of the hybrid blocking layer to expose the TiO_2 network at the surface of the film and ensure high conductivity. The grinding effect of the plasma produced very smooth, closed films on rough FTO substrates, whereas their thickness showed to be dependent on the composition of the sol-gel mixture. Among three different investigated compositions, the film with the highest amount of TiO_2 precursor (10 %) yielded the best results. With 68 nm, the thickness of the hybrid blocking layer was reduced by half compared to the conventional one. In this approach Polymer1 was used in the preparation of the hybrid films, leading to an inhomogeneous distribution of the TiO_2 particles in the ceramic matrix. The applied thermal treatment was sufficient for the titanium dioxide to crystallize within the hybrid material, however, an amorphous fraction remained. The presence of a percolating TiO_2 network for current flow was shown by conductive scanning force microscopy. The area relevant for charge transport was

found to be higher for the hybrid blocking layer than for the conventional film, and the macroscopic conductance of the hybrid film was increased by 32 %. In the application in solid-state DSSCs, the hybrid as well as the conventional blocking layer both showed to effectively avoid charge recombination and enhance the efficiency compared to a reference device without blocking layer. The efficiency of the device employing the hybrid blocking layer (1.37 %) was increased significantly compared to the reference device without blocking layer (0.35 %). A remarkable increase in the short-circuit current indicated that the increased overall efficiency is a result of reduced charge recombination. The efficiency of the solar cell employing the conventional blocking layer was 2.98 % owing to a better electrical contact between active titania layer and conventional blocking layer as compared to the hybrid blocking layer.

A further preparation method for the hybrid blocking layer was presented in which the plasma etching step was replaced by a solvent vapor annealing treatment. In this approach, Polymer2 was used to template the hybrid films, leading to a homogeneous distribution of the TiO_2 particles within the ceramic matrix. The solvent vapor annealing treatment increased the conductivity of the hybrid films on the microscopic as well as on the macroscopic scale. These hybrid films showed about twice the conductance of the conventional blocking layer. The application in solid-state DSSCs confirmed the finding that the sol-gel mixture with 10 % TiO_2 precursor yields the best results. Films of this composition exhibited a thickness of 78 nm, thus, a reduction of 36 % compared to the conventional blocking layer was achieved. The efficiency of the solar cell employing the annealed, hybrid blocking layer (2.71 %) was significantly higher compared to the reference device without blocking layer (0.50 %), validating the functionality of the hybrid material. Moreover, the efficiency of the solar cell with the conventional blocking layer (2.65 %) was exceeded. The long-term stability of solar cells employing the different blocking layers during their exposure to ambient atmosphere was investigated. Though the efficiencies dropped due to aging effects initially, the higher efficiency of the device with the hybrid blocking layer over the device with the conventional one was preserved during the long-term study.

In conclusion, a convenient technique to produce organic-inorganic hybrid films is presented that is essentially equivalent to the preparation of classical blocking layer films. In contrast to pure inorganic blocking layer films, the hybrid material offers the possibility to produce very thin enclosed films on rough TCO substrates. These films exhibit a higher conductance compared to the conventional blocking layer, leading to an increased energy conversion efficiency in solid-state dye-sensitized solar cells.

Three important factors that influence the properties and the functionality of the hybrid films have been pointed out: The preparation method, the templating agent, and the composition of the sol-gel mixture strongly influence the properties of the resulting material. Thus, there are still open issues left in the optimization of the hybrid blocking layer. For example, the sol-gel composition with the highest amount of TiO_2 precursor (10 %) yielded the best results throughout this thesis. An increase of the amount of TiO_2 precursor to e.g. 15 % may further improve the properties of the hybrid film. It was shown that the increase of the TiO_2 precursor is accompanied by an increase of the film thickness. By adjusting the speed and the acceleration of the spin coating process, the thickness of the films could further be reduced, thereby increasing the conductivity and improving the functionality of the blocking layer. Further block length ratios of the templating agent may lead to cylindrical ordered titania structures, which would provide ideal pathways for charge percolation. Additionally, the use of an alternative TiO_2 precursor that does not require a thermal treatment (e.g. ethylene glycol modified titanate) could improve the degree of crystallinity and simplify the preparation method. This way, the hybrid blocking layer, having the potential for improvement, could render suitable for commercial applications.

Bibliography

[1] A. Evans, V. Strezov, T. J. Evans, *Renewable and Sustainable Energy Reviews* **13**, 1082 (2009).

[2] P. Würfel, *Physics of solar cells: from principles to new concepts* (Wiley-VCH, 2005).

[3] M. Bunn, O. Heinonen, *Science* **333**, 1580 (2011).

[4] Z. Chen, F. Blaabjerg, *Renewable and Sustainable Energy Reviews* **13**, 1288 (2009).

[5] K. H. Solangi, M. R. Islam, R. Saidur, N. A. Rahim, H. Fayaz, *Renewable and Sustainable Energy Reviews* **15**, 2149 (2011).

[6] R. Sternberg, *Renewable and Sustainable Energy Reviews* **14**, 713 (2009).

[7] J. S. Yuan, K. H. Tiller, H. Al-Ahmad, N. R. Stewart, C. N. Stewart Jr, *Trends in Plant Science* **13**, 421 (2008).

[8] D. R. Conn, *Library Journal* **136**, 102 (2011).

[9] R. Banos, *et al.*, *Renewable and Sustainable Energy Reviews* **15**, 1753 (2011).

[10] M. D. Archer, R. Hill, *Clean electricity from photovoltaics* (Imperial College Press, 2001).

[11] A. Goetzberger, V. U. Hoffmann, *Photovoltaic solar energy generation* (Springer, 2005).

[12] T. L. Benanti, D. Venkataraman, *Photosynthesis Research* **87**, 73 (2006).

[13] M. D. Archer, A. J. Nozik, *Nanostructured and photoelectrochemical systems for solar photon conversion* (Imperial College Press, 2008).

[14] B. Oregan, M. Grätzel, *Nature* **353**, 737 (1991).

[15] U. Bach, Solid-state dye-sensitized mesoporous TiO_2 solar cells, PhD Thesis (2000).

[16] J. H. Koh, J. K. Koh, J. A. Seo, J. S. Shin, J. H. Kim, *Nanotechnology* **22**, 7 (2011).

[17] I. Y. Song, S. H. Park, J. Lim, Y. S. Kwon, T. Park, *Chemical Communications* **47**, 10395 (2011).

[18] H. Tian, X. Yang, R. Chen, A. Hagfeldt, L. Sun, *Energy and Environmental Science* **2**, 674 (2009).

[19] H. J. Snaith, M. Grätzel, *Advanced Materials* **18**, 1910 (2006).

[20] Y. Tachibana, K. Umekita, Y. Otsuka, S. Kuwabata, *Journal of Physics D: Applied Physics* **41**, 5 (2008).

[21] J.-H. Yum, P. Chen, M. Grätzel, M. K. Nazeeruddin, *ChemSusChem* **1**, 699 (2008).

[22] J. C. Bernede, *Journal of the Chilean Chemical Society* **53**, 1549 (2008).

[23] M. A. Green, K. Emery, Y. Hishikawa, W. Warta, E. D. Dunlop, *Progress in Photovoltaics* **19**, 565 (2011).

[24] A. A. Rockett, *Current Opinion in Solid State and Materials Science* **14**, 117 (2010).

[25] S. S. Sun, N. S. Sariciftci, *Organic photovoltaics: mechanism, materials, and devices* (Taylor and Francis, 2005).

[26] C. J. Brabec, V. Dyakonov, U. Scherf, *Organic photovoltaics: materials, device physics, and manufacturing technologies* (Wiley-VCH, 2008).

[27] H. Hoppe, N. S. Sariciftci, *Polymer Solar Cells* (Springer, 2008).

[28] H. Spanggaard, F. C. Krebs, *Solar Energy Materials and Solar Cells* **83**, 125 (2004).

[29] C. Deibel, V. Dyakonov, *Reports on Progress in Physics* **73**, 39 (2010).

[30] X. N. Yang, J. K. J. van Duren, R. A. J. Janssen, M. A. J. Michels, J. Loos, *Macromolecules* **37**, 2151 (2004).

[31] C. Y. Kwong, A. B. Djurisic, P. C. Chui, K. W. Cheng, W. K. Chan, *Chemical Physics Letters* **384**, 372 (2004).

[32] L. Wonjoo, S. Seunghoon, H. Sung-Hwan, C. Byung Won, *Applied Physics Letters* **92**, 193307 (2008).

[33] I. Gur, N. A. Fromer, C.-P. Chen, A. G. Kanaras, A. P. Alivisatos, *Nano Letters* **7**, 409 (2006).

[34] A. R. W. Andrew, et al., *Journal of Physics D: Applied Physics* **38**, 2006 (2005).

[35] C. Dehu, *et al.*, *Applied Physics Letters* **88**, 183111 (2006).

[36] W. J. E. Beek, M. M. Wienk, R. A. J. Janssen, *Advanced Materials* **16**, 1009 (2004).

[37] N. Kudo, Y. Shimazaki, H. Ohkita, M. Ohoka, S. Ito, *Solar Energy Materials and Solar Cells* **91**, 1243 (2007).

[38] L. Yun-Yue, C. Tsung-Hung, C. Chun-Wei, S. Wei-Fang, *Applied Physics Letters* **92**, 053312 (2008).

[39] N. G. Park, J. van de Lagemaat, A. J. Frank, *Journal of Physical Chemistry B* **104**, 8989 (2000).

[40] A. J. Breeze, Z. Schlesinger, S. A. Carter, P. J. Brock, *Physical Review B* **64** (2001).

[41] Q. Fan, B. McQuillin, D. D. C. Bradley, S. Whitelegg, A. B. Seddon, *Chemical Physics Letters* **347**, 325 (2001).

[42] S.-S. Kim, J. Jo, C. Chun, J.-C. Hong, D.-Y. Kim, *Journal of Photochemistry and Photobiology A: Chemistry* **188**, 364 (2007).

[43] K. Naomi, *et al.*, *Applied Physics Letters* **90**, 183513 (2007).

[44] T.-W. Zeng, *et al.*, *Solar Energy Materials and Solar Cells* **93**, 952 (2009).

[45] S. Ferrere, A. Zaban, B. A. Gregg, *Journal of Physical Chemistry B* **101**, 4490 (1997).

[46] K. Hara, *et al.*, *Chemical Communications* **6**, 569 (2001).

[47] H. Tokuhisa, P. T. Hammond, *Advanced Functional Materials* **13**, 831 (2003).

[48] K. Sayama, *et al.*, *Solar Energy Materials and Solar Cells* **80**, 47 (2003).

[49] P. Wang, *et al.*, *Nature Materials* **2**, 402 (2003).

[50] H. J. Snaith, *et al.*, *Nano Letters* **7**, 3372 (2007).

[51] L. Schmidt-Mende, S. M. Zakeeruddin, M. Grätzel, *Applied Physics Letters* **86** (2005).

[52] M. K. Nazeeruddin, *et al.*, *Journal of the American Chemical Society* **115**, 6382 (1993).

[53] M. Grätzel, *Progress in Photovoltaics* **14**, 429 (2006).

[54] D. B. Kuang, *et al.*, *Small* **3**, 2094 (2007).

[55] H. J. Snaith, M. Grätzel, *Applied Physics Letters* **89**, 3 (2006).

[56] L. Schmidt-Mende, M. Grätzel, *Thin Solid Films* **500**, 296 (2006).

[57] H. J. Snaith, *et al.*, *Nanotechnology* **19**, 12 (2008).

[58] U. Würfel, Untersuchung zum Elektronentransport im nanoporösen TiO_2 von Farbstoffsolarzellen, PhD Thesis (2006).

[59] U. Bach, *et al.*, *Nature* **395**, 583 (1998).

[60] P. Peter, Y. Aharon, R. F. Stephen, *Journal of Applied Physics* **93**, 3693 (2003).

[61] L. Gang, V. Shrotriya, Y. Yan, H. Jinsong, Y. Yang, *Journal of Materials Chemistry* **17** (2007).

[62] L. Lüer, *et al.*, *Organic Electronics* **5**, 83 (2004).

[63] S. Thomas, B. Wolfgang, *Journal of Applied Physics* **90**, 3632 (2001).

[64] T. Xu, Q. Qiao, *Energy and Environmental Science* **4**, 2700 (2011).

[65] C. J. Brabec, N. S. Sariciftci, J. C. Hummelen, *Advanced Functional Materials* **11**, 15 (2001).

[66] M. Helgesen, R. Sondergaard, F. C. Krebs, *Journal of Materials Chemistry* **20**, 36 (2009).

[67] C. Y. Kuo, *Applied Physics Letters* **93**, 033307 (2008).

[68] Y.-Y. Lin, *et al.*, *Journal of the American Chemical Society* **131**, 3644 (2009).

[69] Z. Rui, *et al.*, *Applied Physics Letters* **93**, 013102 (2008).

[70] M.-C. Wu, *et al.*, *Journal of Materials Chemistry* **18**, 4097 (2008).

[71] T. B. Meyer, A. F. Meyer, D. Ginestoux, *Proceedings of the SPIE - The International Society for Optical Engineering* **4108**, 8 (2001).

[72] W. H. Howie, J. E. Harris, J. R. Jennings, L. M. Peter, *Solar Energy Materials and Solar Cells* **91**, 424 (2007).

[73] L. Kavan, M. Grätzel, *Electrochimica Acta* **40**, 643 (1995).

[74] S. S. Williams, *et al.*, *Chemistry of Materials* **20**, 5229 (2008).

[75] Y. Yoshida, *et al.*, *Solar Energy Materials and Solar Cells* **92**, 646 (2008).

[76] B. Peng, *et al.*, *Coordination Chemistry Reviews* **248**, 1479 (2004).

[77] M. C. Lechmann, Self assembled hybrid materials for solar cell application, PhD Thesis (2010).

[78] J. Krüger, Interface engineering in solid-state dye-sensitized solar cells, PhD Thesis (2003).

[79] Y. J. Kim, *et al.*, *Journal of Nanoscience and Nanotechnology* **10**, 340 (2010).

[80] B. A. Gregg, F. Pichot, S. Ferrere, C. L. Fields, *Journal of Physical Chemistry B* **105**, 1422 (2001).

[81] S. Lee, *et al.*, *Journal of Physical Chemistry C* **113**, 6878 (2009).

[82] A. O. T. Patrocinio, L. G. Paterno, N. Y. M. Iha, *Journal of Photochemistry and Photobiology A: Chemistry* **205**, 23 (2009).

[83] R. Betancur, M. Maymo, X. Elias, L. T. Vuong, J. Martorell, *Solar Energy Materials and Solar Cells* **95**, 735 (2011).

[84] J. Xia, N. Masaki, K. Jiang, S. Yanagida, *Chemical Communications* **2**, 138 (2007).

[85] Z. H. Feng, Y. B. Hou, D. S. Lei, *Renewable Energy* **35**, 1175 (2010).

[86] P. J. Cameron, L. M. Peter, *Journal of Physical Chemistry B* **107**, 14394 (2003).

[87] J. N. Hart, D. Menzies, Y. B. Cheng, G. P. Simon, L. Spiccia, *Journal of Sol-Gel Science and Technology* **40**, 45 (2006).

[88] M. Wu, *et al.*, *Journal of Solid State Electrochemistry* **14**, 857 (2010).

[89] C. D. Grant, *et al.*, *Synthetic Metals* **132**, 197 (2003).

[90] J. McLeskey, J. T., Q. Qiquan, J. Beck, R. Lumpkin, J. Pretko, *Solar Energy Materials and Solar Cells* **90** (2006).

[91] E. Fortunato, D. Ginley, H. Hosono, D. C. Paine, *MRS Bulletin* **32**, 242 (2007).

[92] L. Sangwook, *et al.*, *Journal of Physical Chemistry C* **113** (2009).

[93] H. Kim, G. P. Kushto, R. C. Y. Auyeung, A. Pique, *Applied Physics A: Materials Science and Processing* **93**, 521 (2008).

[94] C. Sima, C. Grigoriu, S. Antohe, *Thin Solid Films* **519**, 595 (2010).

[95] T. Kawashima, H. Matsui, N. Tanabe, *Thin Solid Films* **445**, 241 (2003).

[96] I. A. Ryzhikov, *et al.*, *Microelectronic Engineering* **69**, 270 (2003).

[97] T. Mizuno, H. Nagata, S. Manabe, *Journal of Non-Crystalline Solids* **100**, 236 (1988).

[98] A. Jagota, C. Y. Hui, *Mechanics of Materials* **11**, 221 (1991).

[99] M. Mah, J. M. Heintz, J. Rodel, P. Reynders, *Journal of the European Ceramic Society* **28**, 2003 (2008).

[100] M. Memesa, *et al.*, *Energy and Environmental Science* **2**, 783 (2009).

[101] R. J. P. Corriu, D. Leclercq, P. H. Mutin, A. Vioux, *Journal of Sol-Gel Science and Technology* **8**, 327 (1997).

[102] M. Memesa, Y. J. Cheng, J. Perlich, P. Müller-Buschbaum, J. S. Gutmann, *Synthesis and Reactivity in Inorganic, Metal-Organic and Nano-Metal Chemistry* **37**, 315 (2006).

[103] V. Abetz, *Block copolymers* (Springer, 2005). Bd. 1.

[104] F. S. Bates, G. H. Fredrickson, *Physics Today* **52**, 32 (1999).

[105] F. S. Bates, *Science* **251**, 898 (1991).

[106] M. W. Matsen, F. S. Bates, *Macromolecules* **29**, 1091 (1996).

[107] M. J. Fasolka, A. M. Mayes, *Annual Review of Materials Research* **31**, 323 (2001).

[108] R. A. Segalman, *Materials Science and Engineering R* **48**, 191 (2005).

[109] V. Abetz, *Block copolymers* (Springer, 2005). Bd. 2.

[110] Y. S. Jung, C. A. Ross, *Small* **5**, 1654 (2009).

[111] G. Rethore, A. Pandit, *Small* **6**, 488 (2010).

[112] E. J. W. Crossland, *et al.*, *Nano Letters* **9**, 2807 (2009).

[113] M. Park, C. Harrison, P. M. Chaikin, R. A. Register, D. H. Adamson, *Science* **276**, 1401 (1997).

[114] R. J. P. Corriu, D. Leclercq, *Angewandte Chemie - International Edition in English* **35**, 1420 (1996).

[115] J. Geserick, Synthese mesoskopisch organisierter Nanopartikel, PhD Thesis (2009).

[116] M. C. Orilall, U. Wiesner, *Chemical Society Reviews* **40**, 520 (2011).

[117] Y. J. Cheng, J. S. Gutmann, *Journal of the American Chemical Society* **128**, 4658 (2006).

[118] Y. J. Cheng, P. Müller-Buschbaum, J. S. Gutmann, *Small* **3**, 1379 (2007).

[119] F. Falaras, T. Stergiopoulos, D. S. Tsoukleris, *Small* **4**, 770 (2008).

[120] S. H. Kim, *et al.*, *Small* **4**, 2162 (2008).

[121] Z. C. Sun, *et al.*, *Chemphyschem* **7**, 370 (2006).

[122] P. D. Topham, A. J. Parnell, R. C. Hiorns, *Journal of Polymer Science Part B: Polymer Physics* **49**, 1131 (2011).

[123] R. Ulrich, A. Du Chesne, M. Templin, U. Wiesner, *Advanced Materials* **11**, 141 (1999).

[124] E. J. W. Crossland, *et al.*, *Nano Letters* **9**, 2813 (2009).

[125] P. Docampo, *et al.*, *Advanced Functional Materials* **20**, 1787 (2010).

[126] W. Zhang, *et al.*, *Small* **6**, 2176 (2010).

[127] M. C. Lechmann, D. Kessler, J. S. Gutmann, *Langmuir* **25**, 10202 (2009).

[128] M. C. Lechmann, *et al.*, *Journal of Materials Chemistry* **21**, 7765 (2011).

[129] K. Matyjaszewski, *Macromolecular Engineering* (Wiley-VCH, Weinheim, 2007).

[130] H. R. Kricheldorf, O. Nuyken, G. Swift, *Handbook of polymer synthesis* (Marcel Dekker, 2005).

[131] R. B. Grubbs, *Polymer Reviews* **51**, 104 (2011).

[132] K. Matyjaszewski, J. H. Xia, *Chemical Reviews* **101**, 2921 (2001).

[133] N. V. Tsarevsky, *et al.*, *Journal of Molecular Catalysis A: Chemical* **257**, 132 (2006).

[134] J. H. Xia, K. Matyjaszewski, *Macromolecules* **30**, 7697 (1997).

[135] H. W. Spiess, *Macromolecular Chemistry and Physics* **204**, 340 (2003).

[136] T. Williams, *Journal of Materials Science* **5**, 811 (1970).

[137] J. Cazaux, *Journal of Microscopy - Oxford* **217**, 16 (2005).

[138] G. H. Michler, *Electron Microscopy of Polymers* (Springer, 2008).

[139] D. A. Muller, *Nature Materials* **8**, 263 (2009).

[140] M. Czank, J. Mayer, U. Klein, *European Journal of Mineralogy* **9**, 1199 (1997).

[141] M. O. Gallyamov, *Macromolecular Rapid Communications* **32**, 1210 (2011).

[142] S. Weber, Electrical scanning probe microscopy on organic optoelectronic structures, PhD Thesis (2010).

[143] A. Gibaud, S. Hazra, *Current Science* **78**, 1467 (2000).

[144] M. Tolan, W. Press, *Zeitschrift Für Kristallographie* **213**, 319 (1998).

[145] C. Haydn, *Materials Chemistry and Physics* **43**, 116 (1996).

[146] P. Scherrer, *Nachr. Gött.* **2**, 96 (1918).

[147] B. Chu, B. S. Hsiao, *Chemical Reviews* **101**, 1727 (2001).

[148] www.gisaxs.de.

[149] A. Hayakawa, O. Yoshikawa, T. Fujieda, K. Uehara, S. Yoshikawa, *Applied Physics Letters* **90** (2007).

[150] H. Yu, S. Q. Zhang, H. J. Zhao, G. Will, P. R. Liu, *Electrochimica Acta* **54**, 1319 (2009).

[151] M. Memesa, An alternative blocking layer for titanium dioxide (TiO_2) solar cell applications, PhD Thesis (2008).

[152] P. F. W. Simon, R. Ulrich, H. W. Spiess, U. Wiesner, *Chemistry of Materials* **13**, 3464 (2001).

[153] P. D. Cozzoli, A. Kornowski, H. Weller, *Journal of the American Chemical Society* **125**, 14539 (2003).

[154] C. G. Pantano, A. K. Singh, H. X. Zhang, *Journal of Sol-Gel Science and Technology* **14**, 7 (1999).

[155] S. C. Padmanabhan, *et al.*, *Chemistry of Materials* **19**, 4474 (2007).

[156] R. Berger, H. J. Butt, M. B. Retschke, S. A. L. Weber, *Macromolecular Rapid Communications* **30**, 1167 (2009).

[157] Q. Q. Qiao, J. T. McLeskey, *Applied Physics Letters* **86**, 3 (2005).

[158] S. Ruhle, T. Dittrich, *Journal of Physical Chemistry B* **109**, 9522 (2005).

[159] G. Kron, T. Egerter, J. H. Werner, U. Rau, *Journal of Physical Chemistry B* **107**, 3556 (2003).

[160] J. N. Hart, D. Menzies, Y. B. Cheng, G. P. Simon, L. Spiccia, *C. R. Chimie* **9**, 622 (2006).

[161] S. Ito, *et al.*, *Chemical Communications* **34**, 4351 (2005).

[162] B. Yoo, *et al.*, *Journal of Electroanalytical Chemistry* **638**, 161 (2010).

[163] J. Xia, N. Masaki, K. Jiang, S. Yanagida, *Journal of Physical Chemistry B* **110**, 25222 (2006).

[164] F. Fabregat-Santiago, *et al.*, *Journal of the American Chemical Society* **131**, 558 (2009).

[165] C. S. Karthikeyan, M. Thelakkat, *Inorganica Chimica Acta* **361**, 635 (2008).

[166] H. J. Snaith, L. Schmidt-Mende, *Advanced Materials* **19**, 3187 (2007).

[167] J. B. Xia, N. Masaki, K. J. Jiang, Y. Wada, S. Yamagida, *Chemistry Letters* **35**, 252 (2006).

[168] A. Kumar, S. Sista, Y. Yang, *Journal of Applied Physics* **105**, 94512 (2009).

[169] S. H. Kim, M. J. Misner, T. Xu, M. Kimura, T. P. Russell, *Advanced Materials* **16**, 226 (2004).

[170] K. Fukunaga, H. Elbs, R. Magerle, G. Krausch, *Macromolecules* **33**, 947 (2000).

[171] K. Fukunaga, T. Hashimoto, H. Elbs, G. Krausch, *Macromolecules* **35**, 4406 (2002).

[172] J. N. L. Albert, T. H. Epps, *Materials Today* **13**, 24 (2010).

[173] Y. Xuan, *et al.*, *Macromolecules* **37**, 7301 (2004).

[174] S. Lenz, *et al.*, *European Physical Journal - Applied Physics* **51** (2010).

[175] M. Jorgensen, K. Norrman, F. C. Krebs, *Solar Energy Materials and Solar Cells* **92**, 686 (2008).

[176] C. S. Kim, S. S. Lee, E. D. Gomez, J. B. Kim, Y. L. Loo, *Applied Physics Letters* **94** (2009).

[177] N. Golego, S. A. Studenikin, M. Cocivera, *Physical Review B* **61**, 8262 (2000).

Abbreviations

AM 1.5 G	air mass 1.5 global
ATRP	atom transfer radical polymerization
BL	blocking layer
CIGS	copper indium gallium selenide
DSSC	dye-sensitized solar cell
η	power conversion efficiency
ESI	electron spectroscopy imaging
FF	fill factor
FIB	focused ion beam
FTO	fluorine-doped tin oxide
GISAXS	grazing incidence small angle X-ray scattering
GPC	gel permeation chromatography
HOMO	highest occupied molecular orbital
ITO	tin-doped indium oxide
I_{SC}	short-circuit current
IV curve	current-voltage curve
J_{SC}	short-circuit current density
JV curve	current density-voltage curve
Li-TFSI	Lithium-bis(trifluoromethylsulfonyl)imide
LUMO	lowest unoccupied molecular orbital
MA(PDMS)	poly(dimethylsiloxane)methylmethacrylate
NMP	nitroxide mediated polymerization
NMR	nuclear magnetic resonance
PCBM	6,6-phenyl-C_{61}-butyric acid methyl ester
PDMS	poly(dimethylsiloxane)
PEO	poly(ethylene oxide)
PEO-MA(PDMS)	poly(ethylene oxide)-block-poly(dimethylsiloxane)methylmethacrylate
PMDETA	N, N, N', N', N"-pentamethyldiethylenetriamine

PPV	poly(phenylene vinylene)
P3HT	poly(3-hexylthiophene)
RAFT	reversible addition fragmentation chain transfer
RMS	root mean square
R_P	parallel shunt resistance
R_S	series resistance
SAXS	small angle X-ray reflectivity
SEM	scanning electron microscopy
SFM	scanning force microscopy
spiro-OMeTAD	2,2',7,7'-tetrakis-(N,N-p-dimethoxyphenylamine)-9,9'-spiro-bifluorene
TCO	transparent conductive oxide
TEM	transmission electron microscopy
THF	tetrahydrofuran
TTIP	titanium tetraisopropoxide
V_{OC}	open-circuit voltage
XRD	X-ray diffraction
XRR	X-ray reflectivity
Z907	cis-Bis(isothiocyanato)(2,2'-bipyridyl-4,4'-dicarboxylato)(4,4'-di-nonyl-2'-bipyridyl)ruthenium(II)